LASER SURFACE TREATMENT OF AMORPHOUS METALS

Shravana K. Katakam, B.Tech

Dissertation Prepared for the Degree of

DOCTOR OF PHILOSOPHY

UNIVERSITY OF NORTH TEXAS

May 2014

APPROVED:

Narendra B. Dahotre, Major Professor
Rajarshi Banerjee, Co-Major Professor:
Sundeep Mukherjee, Co-Major Professor
Zhenhai Xia, Committee Member
Peter Collins, Committee Member
Nigel Shepherd, Chair of the Department of Materials Science and Engineering
Costas Tsatsoulis, Dean of the College of Engineering
Mark Wardell, Dean of the Toulouse Graduate School

Katakam, Shravana K. Laser Surface Treatment of Amorphous Metals. Doctor of Philosophy (Materials Science and Engineering), May 2014, 121 pp., 8 tables, 52 figures, references, 157 titles.

Amorphous materials are used as soft magnetic materials and also as surface coatings to improve the surface properties. Furthermore, the nanocrystalline materials derived from their amorphous precursors show superior soft magnetic properties than amorphous counter parts for transformer core applications. In the present work, laser based processing of amorphous materials will be presented.

Conventionally, the nanocrystalline materials are synthesized by furnace heat treatment of amorphous precursors. Fe-based amorphous/nanocrystalline materials due to their low cost and superior magnetic properties are the most widely used soft magnetic materials. However, achieving nanocrystalline microstructure in Fe-Si-B ternary system becomes very difficult owing its rapid growth rate at higher temperatures and sluggish diffusion at low temperature annealing. Hence, nanocrystallization in this system is achieved by using alloying additions (Cu and Nb) in the ternary Fe-Si-B system. Thus, increasing the cost and also resulting in reduction of saturation magnetization. laser processing technique is used to achieve extremely fine nanocrystalline microstructure in Fe-Si-B amorphous precursor. Microstructure-magnetic Property-laser processing co-relationship has been established for Fe-Si-B ternary system using analytical techniques. Laser processing improved the magnetic properties with significant increase in saturation magnetization and near zero coercivity values.

Amorphous materials exhibit excellent corrosion resistance by virtue of their atomic structure. Fe-based amorphous materials are economical and due to their ease of processing are of potential interest to synthesize as coatings materials for wear and corrosion resistance

applications. Fe-Cr-Mo-Y-C-B amorphous system was used to develop thick coatings on 4130 Steel substrate and the corrosion resistance of the amorphous coatings was improved. It is also shown that the mode of corrosion depends on the laser processing conditions. The microstructure evolution and the corrosion mechanisms operating are evaluated using post processing and post corrosion analysis.

ACKNOWLEDGEMENT

I would like to express my deep sense of gratitude to Dr.Narendra Dahotre without whom this work would not have been done. I am grateful to him for providing me with this wonderful opportunity to work under his guidance. He has been a great mentor not only in technical perspective but also for my overall personality development. I would also like to thank my co-advisor Dr.Rajarshi Banerjee with whom I had the closest interaction after my major advisor. He is an excellent teacher, in fact one of the best I have come across and great person to work.with
I would also thank Dr.Nigel Shepherd, Sundeep Mukherjee and Rick Reidy for their help and useful discussions in various topics which helped me a lot in clarifying many of my theoretical concepts. I also thank Dr.Pete Collins for his useful suggestions and discussions on microscopy and diffraction. I also would thank Dr.Zhenai Xia for serving in my committee. I would like to thank Dr.Juneyon Hwang, for his vital support during the initial stages of my doctoral study. I acknowledge Dr.Soumya nag and my friends Peyman, Iman, Dr.Arun devaraj and Casey smith for their help in learning microscopy techniques.

I would also like to acknowledge all the MTSE faculty and staff especially Wendy Agnes and Joan Jolly for being extremely helpful. I would like to thank my friends, Subhasis Meher, Shamiparna, Harpreet, Phalgun, Jitendra, Mageshwari, Sivanesh, Sameehan, Garima, Peeyush, Anchal, Ankit, Shivraj, Nikhil, Abhinay, Sanghita, Aniket, Medha, Nishita, Victor, Nilesh Kumar, Nilesh Denge, Bharat, Aditya, Thomas, Ravi, Hitesh, Dr.Sameer, Dr.Pandian, Dr.David dierks, Dr.David Garret, and other friends. I also thank previous teachers and also mentors Mr.Arvindha babu, Dr.dilshad Akhtar, Dr.Tapan Nath, Mr.Vinay Deshmukh and Prof.A.K.Jha.I am grateful to my family members for their support throughout my life without their support nothing would have been possible.

CONTENTS

LIST OF TABLES

LIST OF FIGURES

CHAPTER 1

INTRODUCTION

Amorphous materials are unique class of materials with only short range ordering compared to their crystalline counterparts with long range periodicity. There has been increased interest in amorphous materials over last few decades due to their interesting properties. Industrial use of these materials is limited owing to their inherent brittle nature. However, these materials find a huge potential when used in applications that require good surface properties. One of the most commercially appealing applications of these materials is to use them as soft magnetic materials and also as surface coatings to improve the surface properties. Furthermore, the nanocrystalline materials derived from their amorphous precursors show superior soft magnetic properties than amorphous and coarse grain crystalline counter parts for high frequency applications. In the current work, laser based processing of amorphous materials will be presented. The nanocrystalline microstructure and amorphous coatings both demand a very high quench rate in order to obtain the desired microstructure. The first part objective of the work deals with the laser based surface heat treatment to improve soft magnetic properties by controlled crystallization whereas second objective is focused on synthesis of amorphous coatings for corrosion resistance.

1.1 Laser Processing of Amorphous Materials

Laser processing is a localized process where a highly intense and coherent laser beam is irradiated onto the sample. The electrons are excited by increasing the vibrational energy by absorbing the energy from the electromagnetic wave Subsequently the electrons interact with the atoms in the lattice resulting in in generation of localized heat within the irradiated region. The material can be heated to different degree based on the power input and residence time, i.e

the amount of irradiation time by the laser beam, as a consequence, the material may suffer local rise in temperature, melting, or even evaporation. A part of the irradiated beam results in reflection, absorption and radiation. And the total energy of the beam is the sum of all the above mentioned phenomena described by the equation below.

$$E = rE + aE + t \text{----------Equation 1.1}$$

where r, a and t are coefficients of reflection, absorption and transmission. The heat input delivered to the material during laser processing is dictated by the absorptivity of the material that is typically 10-20% for metals due to their high reflectivity. Furthermore, the intensity of the laser beam decays exponentially as a function of time and depth described by the Beer-Lamberts law given by the equation:

$$I(Z,t)=I_0(t)(1-R-T)e^{-AZ} \text{----------Equation 1.2}$$

here A is absorptivity, I_0 is the intensity at the surface of the material, Z is the depth from surface and t is time. It can be inferred from the above equation that absorptivity plays a critical role in choosing the laser beam intensity and typically most of the metals are bad absorbers. The absorptivity can be increased by adopting different approaches that include improving the surface roughness, applying paint with high absorptivity, sand blasting etc. A suitable combination of laser power and residence time can be chosen to obtain a wide variety of microstructures due to different heating and cooling rates experienced during processing. A process map has been developed by Steen for proper combination of laser power and interaction time can be chosen depending on the requirement as shown in Figure 1.1. The present work deals with two aspects of laser processing, laser surface heat treatment to perform a controlled phase transformation on amorphous ribbons and laser surface melting to synthesize amorphous coatings. The laser processing conditions are optimized by choosing proper laser power input in

order to achieve proper thermal histories based on the intensity distribution of laser beam given by equation 1. The laser beam scan speed defines the degree of quenching experienced after laser irradiation. Hence by choosing proper laser power and scan speed, the thermodynamics and kinetics of phase transformation can be controlled to achieve desired microstructure.

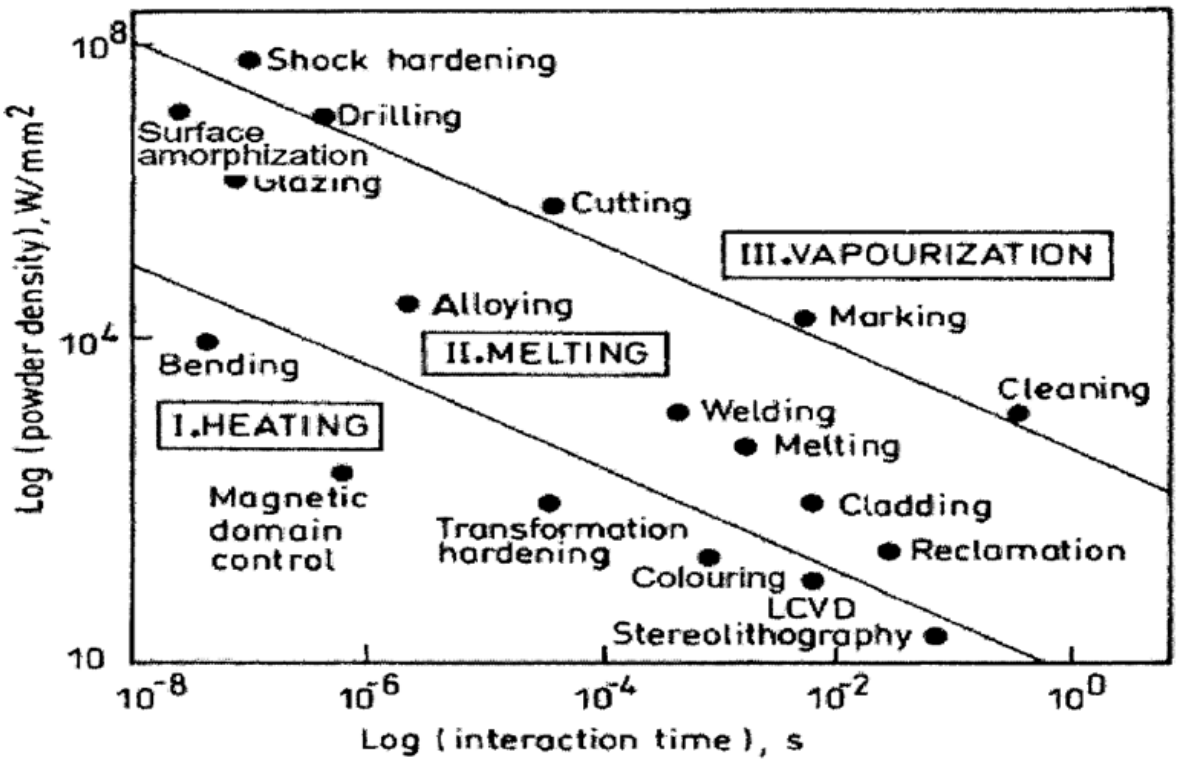

Figure 1.1 Process map as a function of residence time and energy density [1]

1.2 Thesis Outline

The present study of laser processing of amorphous materials is described in 5 chapters and a brief outline of each chapter is presented in this section.

Chapter 1 gives the basic introduction about laser material interaction then followed by the background and motivation for the present study.

Chapter 2 deals with description of the experimental methods adopted. It also includes the formulation of thermal model and also description of boundary conditions.

Chapter 3 describes the material response of Fe-Si-B amorphous ribbon to laser material interaction. The effects of laser energy density on structural relaxation and crystallization are discussed. Furthermore, the mechanisms operating for crystallization during laser processing are explained in the light of thermal stresses experienced across the laser track. The observed phenomena are extended to multipass laser processing. The effects of multi-pass laser processing on microstructure evolution on magnetic behavior. The magnetic properties were evaluated and compared with sample annealed using conventional furnace annealing. The variation in magnetic properties for the laser processed samples are explained extensive microstructural characterization The intrinsic magnetic property variation explained on the basis of compositional changes within the phases evaluated using atom probe tomography. The phase and microstructural evolution across the laser track were done using micro-XRD, transmission electron microscopy coupled with site specific compositional analysis using atom probe tomography to explain the complex crystallization phenomena. However, the multi-pass laser processed samples exhibited higher coercivity due to rapid grain growth ascribed to reheating effects. A magnetic field processing approach was adapted to reduce the observed increment in coercivity value. The synergistic effects of magnetic field coupled with thermal stresses experienced during laser processing were studied and the factors responsible for coercivity reduction are discussed. In summary, microstructure-magnetic property-laser processing relationship has been established for the Fe-Si-B ternary system using different analytical techniques and the laser processing has been optimized to achieve ultrafine grain microstructure with superior magnetic properties.

Chapter 4 deals with the synthesis of amorphous coatings for improved corrosion resistance. The microstructure evolution after laser cladding was evaluated using different

analytical tools and the mechanisms operating for the obtained microstructure are discussed. Furthermore, the corrosion response of the coatings samples is evaluated using post corrosion microscopy analysis. The corrosion mechanisms operating for the coatings are identified and correlated to the thermal histories experienced during laser processing. The thermal histories are evaluated by developing a COMSOL based heat transfer model.

Chapter 5 deals with the synthesis and microstructural evaluation of high entropy alloy coatings using laser processing. The microstructure and phase analysis was done using site specific transmission electron microscopy and the microstructural evolution is correlated to the laser processing conditions.

Chapter 6 concludes with the key outcomes of the present work based on the results and observations of the previous chapters.

Chapter 7 lists the future directions of the present work.

1.3 Background and Motivation

1.3.1 Surface Heat Treatment of Amorphous Materials

1.3.1.1 Motivation

According to the US department of energy report, most of the electricity consumed is generated by burning the fossil fuels (Figure 1.2a). This results in excessive emissions of pollutants affecting the environment. Furthermore, with the advancement of technology there is drastic annual increase in electricity consumption as shown in Figure 1.2b.

Additionally, there has been substantial electric losses incurred during generation, distribution and as well as transmission. In order to meet the ever increasing energy demand and also to minimize the emission of pollutants, there has been a great thrust in developing new energy generation techniques and also to develop infrastructure to minimize the energy losses

incurred during energy transmission and distribution. Soft magnetic materials play an important role in power generation and transmission. They are used in many components like inductors, choke coils and also as transformer core materials. Development of these materials will lead in efficient energy generation and transmission resulting in reduced losses.

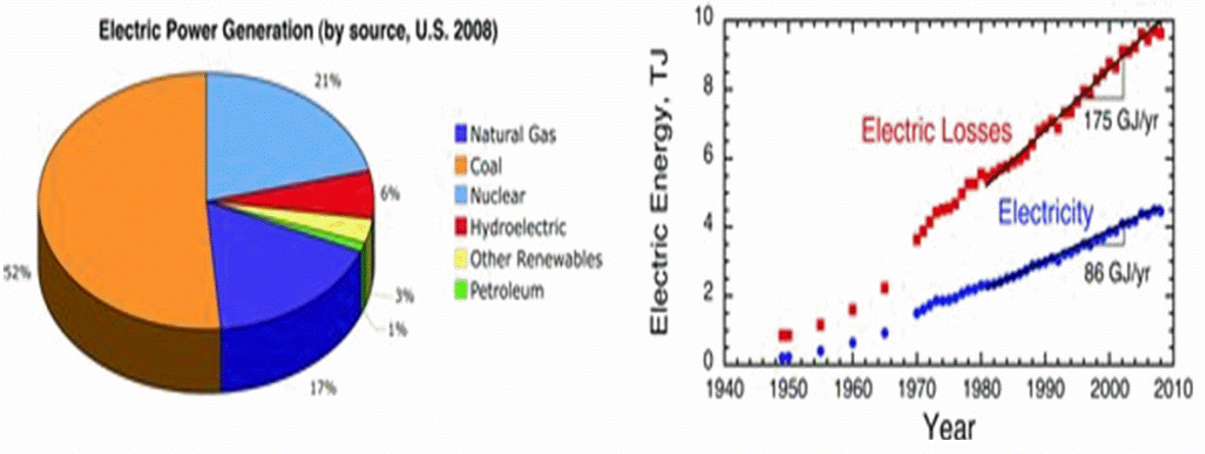

Figure 1.2 (a)Electric power generation by source; (b) residential electricity consumption and electric losses [2]

Transformers play a very vital role in energy transmission and distribution. A subtle increase in their efficiency will have a great economic and environmental impact. To this end, there has been increased interest in developing amorphous and nanocrystalline materials for soft magnetic applications. This is attributed to their superior soft magnetic properties compared to their conventional coarse grain crystalline counterparts. The schematics of B-H curves clearly show the contrast between the magnetic behaviour of crystalline vs amorphous/nanocrystalline materials (Figure 1.3). In order to exhibit superior soft magnetic properties, the material should exhibit a good combination of high saturation magnetization coupled with near zero coercivity values. It can be clearly seen from Figure 1.4 that amorphous and nanocrystalline materials have the superior soft magnetic properties compared to other material systems.

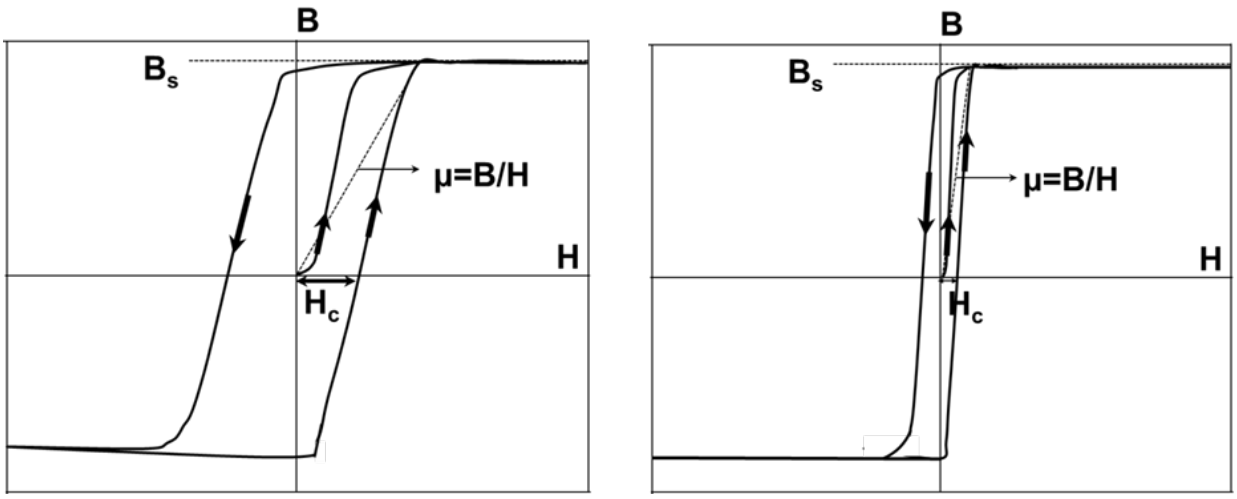

Figure 1.3 Magnetic hysteresis loop with coercivity (a) crystalline materials; (b) amorphous and nanocrystalline materials

However, the use of amorphous materials as transformer cores for high frequency applications has been limited due to their low curie temperature and low permeability at high frequencies. Nonetheless, nanocrystalline materials show superior soft magnetic properties at higher frequencies. The main advantage of nanocrystalline alloys is their high saturation induction of 1.2-1.3 Tesla and superior thermal stability compared to amorphous alloys. A good combination of high saturation magnetization, high permeability even at high frequency coupled with low losses of nanocrystalline materials allows a great reduction in volume and weight of the magnetic components.

Conventionally, the nanocrystalline materials are synthesized by furnace heat treatment of the amorphous precursors. Fe-based amorphous/nanocrystalline materials, due to their low cost and superior magnetic properties are the most widely used soft magnetic materials, Fe-Si-B ternary alloy is one of the widely used ferromagnetic amorphous material used in commercial

amorphous core transformers.

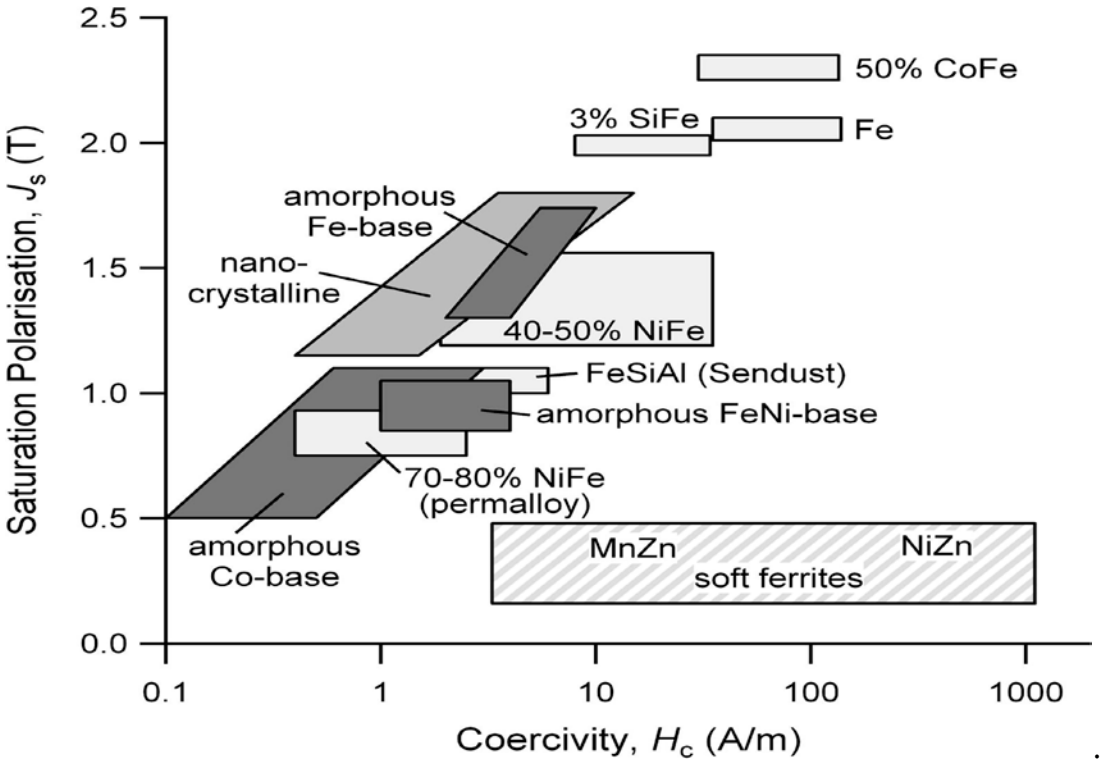

Figure 1.4 Comparison of soft magnetic properties of different materials [2]

However, nanocrystallization resulted in deterioration of soft magnetic properties due to the difficulty in achieving a nanocrystalline microstructure from this ternary system. Obtaining a desired nanocrystalline microstructure is difficult due to sluggish diffusion at low temperature annealing and rapid growth of crystals at higher temperatures. However, nanocrystalline microstructure in this system was achieved by Yoshizawa [3] using alloying additions (Cu and Nb) and the alloy is termed as FINEMET. This alloy system has the best combination of soft magnetic properties even today.

1.3.1.2 Evolution of Soft Magnetic Materials

The soft magnetic materials used for energy transmission in transformer cores were typically Fe-Si steels. The advancement of the soft magnetic field has seen a tremendous change over the years. Ideally, a softmagnetic material should exhibit lower coercivity values along with

higher saturation magnetization. There is an inverse relationship of coercivity (H_c α 1/D) with respect to grain size (D) and low coercivity values are usually achieved by increasing the grain size and avoiding the secondary precipitates which act as domain wall pinning centres. The next advancement is the use of grain oriented silicon steels where the grains are aligned in the direction parallel to the magnetic easy axis to reduce the magneto crystalline anisotropy. Based on the above arguments it can be inferred that superior soft magnetic properties can be achieved by increasing the grain size and also by reducing the magneto crystalline anisotropy. However, a substantial amount of decrease in coercivity is observed with superior soft magnetic properties for amorphous materials. This resulted in flurry of many amorphous systems including Fe-based, Co-based, Fe-Co, Fe-Ni, and Fe-Zr. The crystallization of these amorphous systems resulted in deterioration of soft magnetic properties due to rapid grain growth and also due to precipitation of secondary hard phases. Nonetheless, yoshizawa [3] proved that for very fine grain sizes, the soft magnetic properties are similar to amorphous materials. This was possible by addition of Cu and Nb as alloying additions to Fe-Si-B ternary system. Cu helps to increase the nucleation rate by segregating out from the amorphous matrix due to its immiscibility in Fe and Nb restricts the diffusion of elements. This results in very fine nanocrystalline grain size about 10nm leading to near zero coercivity value. The reduction in coercivity value for nanocrystalline materials has been extensively studied by Herzer and explained based on the random anisotropy model. The theoretical basis of the reduction in coercivity for nanocrystalline materials is further discussed in the following section.

1.3.1.3 Fe-Based Nanocrystalline System

Although there has been substantial research in the past few decades in improving the soft magnetic materials through alloy development, Finemet alloy system is by far the most

widely used soft magnetic material in the nanocrystalline form. This is attributed to their excellent soft magnetic properties at high frequencies and elevated temperatures.

Most of the alloys investigated are Fe-rich alloys which are derivatives of either the Finemet (Fe-Si-Nb-B-Cu) composition or Nanoperm (Fe-Zr-B) composition because of their high saturation inductions. The illustration in Figure 1.5 gives a comparison of magnetic properties of different alloys [4] It is clearly evident that the Fe-based nano-composites have a good combination of very high permeability and saturation magnetization compared to rest of the alloys. Additionally, the Fe-based alloys are made of low cost elements like Fe and Si which makes them even more attractive in economical perspective. One of the most important attractive aspect of the Fe-based nanocrystalline composite materials is their substantially low or near zero magnetostriction that make these materials attractive over stress relieved amorphous alloys. Due to the above mentioned reasons there has been a constant increase in implementing these materials in magnetic cores for ground fault interrupters, common mode chokes and high frequency transformers.

A nanocrystalline microstructure will possess good soft magnetic properties if the amorphous state is crystallized by the primary crystallization route precipitating out bcc Fe without any intermetallic phases. This ideally requires extrememly high nucleation rate coupled with slow growth rate leading to high volume fraction of nanocrystalline phase. Such crystallization has only been obtained by proper alloy design This can be achieved by relatively short annealing times of only 5–10 min and hence very high heating rates of 200–400 K/ min are needed to reach the annealing temperature [5].

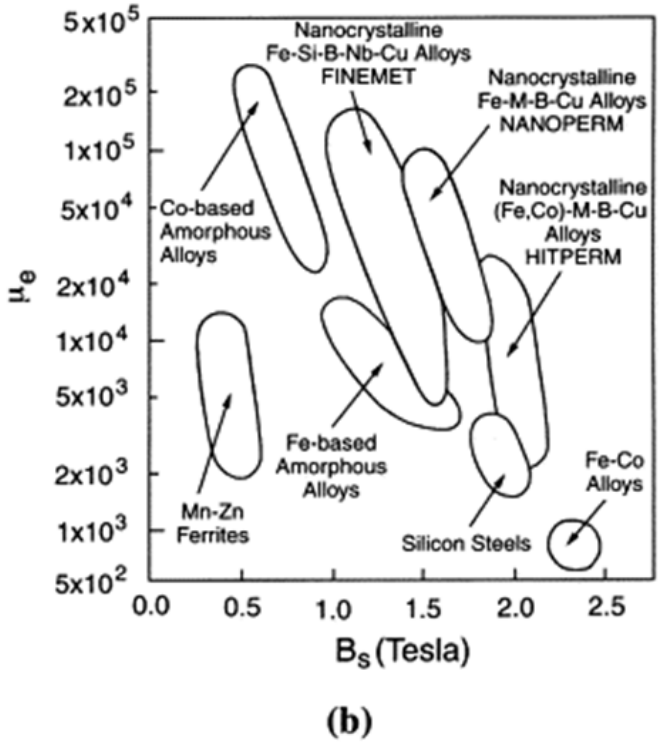

Figure 1.5 Comparison of magnetic properties for several alloys[4]

1.3.1.4 Theoretical Background for Superior Soft Magnetic Properties of Nanocrystalline Materials

The coercivity reduction is dictated by the magnetocrystalline anisotropy constant K which is the index defining the energy density required to rotate the magnetization vector against the preferred easy magnetic axis. Magnetocrystalline anisotropy is caused due to the coupling of spin and orbital motion of electrons and between orbital motion of electron and its lattice. Thus, the magnetic moment tends to align in specific directions within the lattice known as easy magnetization axis. The microstructure consists of distribution of several easy magnetic axis orientations within a structural unit (grain). Thus for large grain material, the magnetization follows the easy magnetization vector of the structural unit and the magnetization is defined by the local magneticrystaline anisotropy of structural element.

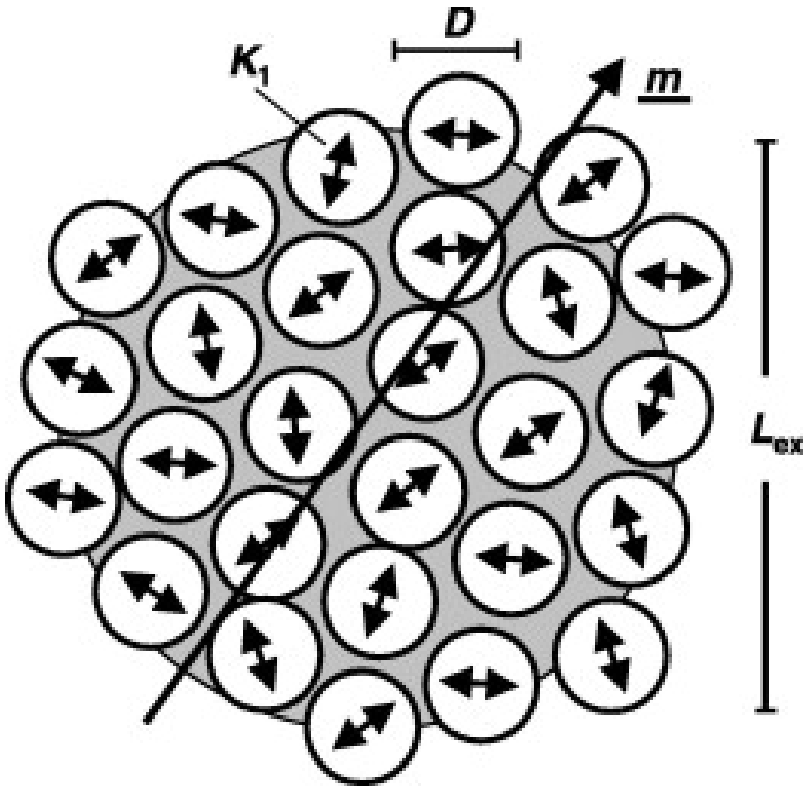

Figure 1.6 Schematic representation of random anisotropy model [6]

However, when the structural unit size falls within the regime of ferromagnetic exchange length, the ferromagnetic exchange forces start to dominate leading to restriction of magnetization along the easy magnetic axis of the structural unit. Thus, the magnetic anisotropy is averaged out over several structural units resulting in very low values as shown schematically in the Figure 1.6. The grey portion represents the ferromagnetic exchange volume defined by the exchange length over which the orientation m is constant. The double headed arrows represent the local magneto crystalline anisotropy of each structural unit. Amorphous and nanocrystalline materials both fall in this regime where the structural correlation lengths are in atomic scale for amorphous materials and within 10-20 nm in case of nanocrystalline materials. As a result, the average magneto crystalline anisotropy drastically reduces given by the equation below and a full theoretical treatment can be found elsewhere [6].

$$<K_1>=K_1(D/L_0)^6$$

The most significant outcome of the random anisotropy model is the variation of K_1 as a function of sixth power of grain size. Furthermore, the effect of grain size on coercivity is found to vary as D^6 where D is the grain size shown by herzer (Figure 1.7) The physical significance of this phenomena can be realized by the following example, when the typical grain size of Fe based nanocrystalline materials is about 10-15nm, the K_1 value shows a substantial decrease from 10^5 J/m^{-3} to few Joules per meter cube indicating a superior soft magnetic behaviour. Thus, the magnitude of change in magnetocrystalline anisotropy is considerably higher making these materials potential candidate for soft magnetic applications. Furthermore, the suppression of magnetocrystalline anisotropy is maintained even at higher temperatures. This is of particular importance for high frequency applications where the temperatures may get elevated due to high eddy currents. The permeability also shows an increment for both amorphous and nanocrystalline materials with increase in temperature. Thus nanocrystalline and amorphous materials exhibit superior soft magnetic properties. The next section describes processes by which nanocrystalline microstructure can be achieved.

1.3.1.5 Synthesis Routes of Nanocrystalline Materials from Amorphous Pre-Cursors

As mentioned earlier, the amorphous materials are heat treated to obtain a composite microstructure of nanocrystalline and amorphous phase. The material should be subjected to proper temperature range and aging time to obtain the desired microstructure. Additionally the heating rates and cooling rates also determine the thermodynamic factors during crystallization. Hence the non-equillibrium processing techniques definitely result in a different microstructure compared to furnace annealing.

1.3.1.6 Conventional Furnace Annealing:

Conventionally a nanocrystalline microstructure is obtained by furnace annealing the amorphous precursor ribbon above its primary crystallization temperature. It is very essential to choose proper annealing temperature and also time to obtain good soft magnetic properties. As explained previously it is essential to obtain extremely fine nanocrystalline microstructure (typically 20-30nm) in order to minimize the coercivity due to exchange forces.

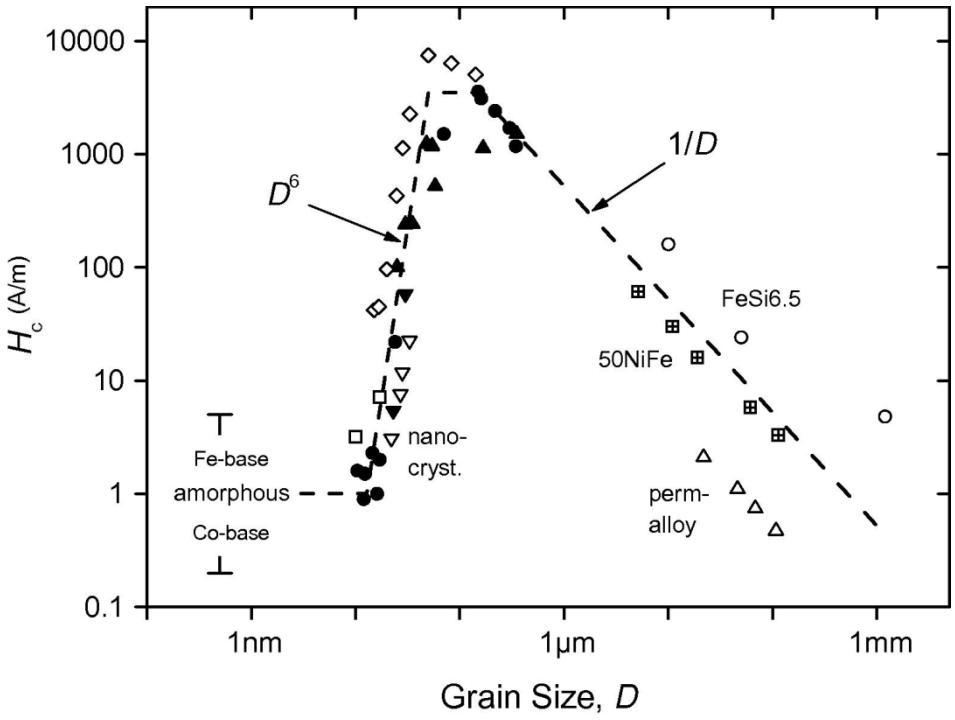

Figure 1.7 Coercivity (Hc) vs. grain size D for various soft magnetic alloys [6]

The initial phase formed typically is BCC α-Fe(Si). The nano crystalline microstructure develops within a very short time (10-15min) and does not alter appreciably on long term annealing. However, annealing at higher temperatures beyond second crystallization temperature (>600C) results in precipitation of iron borides. These borides deteriorate the soft magnetic properties due to their high anisotropies. In addition to conventional annealing, there have been efforts in achieving nanocrystalline microstructure by non-equillibrium techniques discussed as follows:

1.3.1.7 Flash Annealing or Joule Heating

Flash or current annealing has been investigated by many researchers to obtain a fine nanocrystalline microstructure. [7][8,9,10]. Flash annealing involves, heating by means of electric current. In this process, high heating and cooling rates can be achieved leading to nano crystalline microstructure from amorphous precursors. It was also reported that high temperature flash annealing improved the ductility of the crystallized ribbons due to entrapment of Boron in the BCC Fe phase indicating extremely high quench rates during the crystallization process [10]. It was also reported that the permeability also increased by 50% along with reduced brittleness compared to furnace annealing owing to finer grain sizes obtained during flash annealing[8] .The amount of boride phases was also reduced during flash annealing resulting in superior soft magnetic properties. A better mechanical response of the ribbons was also claimed.[7].

1.3.1.8 Laser Surface Treatment of Amorphous Materials

Lasers have been used in wide variety of applications including cutting, surgery, machining and also surface modification by surface heat treatment. Laser surface treatments have been used to improve the mechanical properties [11,12,13,14,15], corrosion properties [16] and also magnetic properties [17,18] by surface treatments. Chen et al [13] showed that plasticity of metallic glasses can be improved by generating residual stresses on the surface. A Zr-based metallic glass rod with composition $Zr_{55}Cu_{30}Al_{10}Ni_5$ was laser treated using a Nd-YAG laser and a significant increase in plastic strain (5.3%) was observed compared to as cast sample (0.3%).Synchrotron radiation and DSC analysis both indicated that crystallization did not take place. However, multiplication of shear bands were observed for laser processed samples and the generation of residual stresses are attributed to induce plasticity.

A similar study was done by Wu et al [19] by irradiating a laser beam onto a $Cu_{46.5}Zr_{47.5}Al_5Co_1$ amorphous rod. It was observed that the top surface retained an amorphous phase where as a graded microstructure with nano and microcrystalline precipitation occurred beneath the melted region. The stress-strain curves reveal a remarkable improvement in plasticity (5.7%) for laser treated sample compared to as the sample in as cast state (1.1%). The improvement in plasticity is attributed to the multiplication of shear bands observed for the laser treated sample. The shear bands are hindered by the precipitates generated at the HAZ and are transformed to a martensitic phase. Thus generation of precipitates in controlled manner hindering the shear bands is speculated to be the important cause for improvement in plasticity. In addition to improving the mechanical properties by surface treatment, lasers are also used to improve the magnetic properties. It has been reported the laser scribing results in significant decrease in core losses for silicon steels used for transformer core applications [20, 21, 22, 23, 24]. It is believed that the laser scribing induces residual stresses that further refine the domain sizes leading to significant decrease in core loss. A similar phenomena is also reported in case of laser irradiation of ferromagnetic amorphous ribbons.[25, 26, 27, 28] It was shown that significant reduction in core losses are observed by laser scribing of amorphous ribbons. This is attributed to refinement of domain structure after laser irradiation.

1.3.2 Surface Modification Using Laser Processed Amorphous Coatings

1.3.2.1 Corrosion Resistance of Amorphous Alloys

The functionality of every industrial component depends on its surface properties. Corrosion is one of the important surface phenomena that occur in almost every component, and proper measures should be taken to mitigate corrosion and improve the longevity of the components. One of the methods to mitigate corrosion is by application of different coatings

with functional surface, resistant to corrosive environment. In crystalline materials corrosion mainly occurs due to chemical inhomogeneity of the material leading to galvanic coupling between the phases. Alloying addition is one of the plausible routes to improve the corrosion resistance in metallic materials with more noble metals and also by adding metals forming protective oxide layers. Polycrystalline materials contain grain boundaries that act as active sites for initiation of corrosion. In contrast, an amorphous material due to their excellent chemical homogeneity throughout the sample reduces the galvanic action substantially compared to crystalline compounds with secondary phases. Furthermore, the absence of grain boundaries also mitigates corrosion by restricting the diffusion of ionic species reducing corrosion. In general, the corrosion resistance is observed to increase with increase in solute concentration of the corrosion resistant elements. In crystalline materials, the concentration of these elements in elemental form is limited and restricted by the maximum solubility of these alloying elements given by the solvous line. However, the concentration of these alloying elements can be increased substantially by synthesizing amorphous compositions with high concentration of corrosion resistant elements.

Furthermore, nature of the oxide film is the most important factor influencing the corrosion resistance. It is believed that an amorphous oxide film forms on a metallic glass where as a crystalline oxide layer form on a crystalline substrate. The ion transport in case of amorphous oxide film drastically reduces due to absence grain boundaries and other defects. In contrast, in case of crystalline oxide layer, the diffusion of ions takes place through defects leading to corrosion. In addition to nature of the film, corrosion resistance also improves with the elements stabilizing the oxide film. The protective ability of the passive film depends on the supply of corrosion resistant ions to the passive film. For instance, it has been reported for metal-

metalloid amorphous alloys that the corrosion resistance is dependent on the availability of chromium ions. Thus corrosion resistance increased with an increase in chromium concentration [29]. This is attributed to the ability of the amorphous phase to effectively supply the Chromium ions to the passive film [29].However; it is challenging to synthesize amorphous materials in bulk form. Therefore, application of amorphous materials in the form of coatings is a plausible route. Although retaining fully amorphous phase in coating is difficult to achieve, composite microstructure with crystalline phases embedded in amorphous matrix have also shown significant improvement in corrosion resistance [30].Different processing routes are adapted to synthesize corrosion resistant amorphous coatings that include spray techniques like HVOF [31,32,33,34,35,36,37], HVAF[31,38,39,40], Plasma spray and [38,40,41,42,43] Laser processing [16,44,45,46,47,48,49]. Coatings with high GFA and ability to retain better corrosion resistance after crystallization are extensively studied in view of their commercial importance. The above mentioned characteristics are mainly met by Zr-based [16], Fe-based [50,51,52] and Ni-based [47] amorphous alloys. In addition, there are few reports on Cu-based, Al-based and other amorphous alloys. The exchange current density during corrosion is defined by [53].

$$i_0 = zfF\ \alpha\left(\frac{N}{N_0}\right) e^{\frac{-\Delta G}{RT}}$$ ----------Equation 1.1

It has been shown that the exchange current density during corrosion depends on the fraction of surface atoms which are electrochemically active sites defined by α. In crystalline materials, defects like ledges, dislocations, grains boundaries, etc act as active sites there by increasing the corrosion current. Hence the chemical and structural homogeneity of the amorphous materials increase the corrosion resistance. Nonetheless, the amorphous phase is a metastable phase and thus the ΔG term will be affected, ΔG represents the activation energy for the reaction. Hence the activation energy for the ions in amorphous phase is lower compared to crystalline phase. Thus

corrosion resistance depends on both the factors structural and chemical uniformity as well as activation energy for dissolution. It is shown that Ni-Cr-Mo corrodes along the grain boundary whereas Fe-Cr-Mo amorphous corrodes uniformly [51] indicating that the uniformity factor has a merit over the activation energy in the present case. Therefore, the effect of structure on the corrosion rate is important and supports the above discussion for Fe-Cr-Mo-Y-B-C system

The present amorphous system $Fe_{48}Cr_{15}Mo_{14}C_{16}B_6Y_2$ has been extensively studied due to its improved glass forming ability and easy processing [54]. Furthermore, it also has excellent corrosion resistance attributed to high amounts of highly corrosion resistant elements like Chromium and Molybdenum. It is reported that these alloy system has exceptional corrosion resistance in highly corrosive environments like HCl and hot calcium brine solutions at the elevated temperature [30,55,56] The combined effect of Cr and Mo in improving corrosion resistance is reported by several researchers [57,58,59]. Yttrium destabilizes the crystalline carbide phase and thus improves the glass forming ability [60]. The present amorphous material (SAM 1651) is under development for potential use in the nuclear industry, as coatings for containers used in transportation and disposal of spent nuclear fuel [61]. Furthermore, due to the absence of hazardous elements, these coatings can also be used for bio-implant applications which demand excellent corrosion resistance in aggressive environments [50]. Hence due to the above mentioned advantages, this system is used for coating purpose.

1.3.2.2 Effects of Crystallization on Corrosion Resistance

As mentioned earlier, the corrosion resistance depends on the stability of the oxide film which inturn depends on the availability of the oxide stabilizing elements. Furthermore, structural relaxation affects the corrosion property by altering the free volume [62]. This can be explained on the fact that the ion transport is altered by changing the active sites. There have

been contradicting reports on the effects of crystallization on the corrosion behaviour. Devitrification leads to precipitation of secondary phases and the nature of the secondary phase will have an effect on the corrosion behaviour. As described in the equation, the ionic transport is dependent on the reduction in free energy as well as presence of activation sites. Thus, crystallization reduces the free energy and hence decreases the corrosion rate. On the contrary, the precipitated phase can form a galvanic couple leading to localized corrosion. Furthermore, if the precipitate formation enriches the corrosion resistant materials like Cr, the corrosion resistance increases. It has been proven for Mg based system that partial devitrification resulted in increased corrosion resistance due to enrichment of alloying element in the matrix whereas complete crystallization showed a decrement in corrosion resistance [62]. However, many amorphous systems including Fe-based are prone to localized corrosion as reported by several researchers

1.3.2.3 Processing Techniques for Synthesis of Amorphous Coatings

Several synthesis routes have been adapted to produce bulk amorphous coatings that include HVOF [63,64,65], thermal spray coatings [66], arc spray coatings [67], and Laser cladding [68,69,70,71]. However, there are several disadvantages associated with different processing routes, typically the spray techniques suffer severe disadvantages like high porosity and debonding of the coating from the substrate surface. It has been reported that spray based processing route suffers corrosion in the intersplat region and porosity within the coatings [32, 33, 34, 38, 39]. In contrast, laser processing has been proven as a promising technique to synthesize bulk coatings on different metallic substrates for wide variety of applications. It offers many advantages like precise control over process parameters, fast processing, and also cost effective over conventional processing techniques. High cooling rates achieved during laser

processing facilitates the retainment of amorphous phase. The precursor amorphous powders are usually expensive due to cost of different alloying elements and the processing route. However Fe-based amorphous powders have been synthesized using gas atomization and are relatively economical compared to other amorphous powders. Fe based amorphous powders have been proven to exhibit excellent glass forming ability (GFA) as well as corrosion resistance [50, 55, 70, 72, 73, 74, 75, 76, 77].

1.3.3 Surface Modification Using Laser Processed HEA Coatings

There has been tremendous interest in developing alloys with multiple elements due to their attractive properties. Conventionally, alloying additions in significant quantities result in formation of intermetallic phases that are undesirable due to the brittle nature of the alloys. However, Yeh [78] and coworkers reported the synthesis of simple solid solution alloy from multiple elements in equi-atomic ratio. The solid solution formation is attributed to high configurational entropy associated with the addition of multiple elements according to boltzmans hypothesis. In addition to excellent bulk properties that include soft magnetic property, mechanical strength and ductility, they also exhibit superior surface properties like wear resistance, corrosion resistance, and high temperature oxidation resistance. Due to the above mentioned surface properties, these materials are promising for coating applications. Laser processing has many advantages over other deposition techniques due to which variety of materials are synthesized as coatings like ceramics, metals, amorphous materials, also high temperature alloys and also high entropy alloys. Laser processing offers a particular advantage in synthesizing HEA coatings as high instantaneous temperatures can be reached and can be rapidly quenched to restrict the diffusion. Rapid quenching becomes important as HEA may undergo various phase transformations like spinodal decomposition, ordering, precipitation due to

reduction in thermodynamic driving force at lower temperatures attributed to reduction in mixing entropy. However, rapid quenching restricts the diffusion of the elements and also restricts the nucleation and growth of brittle intermetallic compounds [79] and thus HEA phase can be retained. There have been reports recently on synthesizing HEA coatings using laser processing. [80][81][82][83].

Zhang et al [80] reported the synthesis of FeNiCoSiCrAlTi HEA coating on 1045 steel substrate. It was observed that HEA coating formed for higher concentration of Fe. The evolution of HEA microstructure was attributed to the rapid quenching during laser processing. A simple BCC HEA phase is reported after laser cladding. The microstructure consisted of equiaxed grains, polygonal and dendritic structure. A considerable amount of low angle grain boundaries are observed between the interfaces of the polygonal grain and the interdendritic grains. This is attributed to the sluggish diffusion kinetics of the atomic species. Furthermore, the coatings also exhibited good soft magnetic behavior. Xiaoyang et al successfully synthesized $Al_xFeCoNiCuCr$ HEA alloy by laser cladding. The high temperature hardness, abrasion performance, and corrosion response of the coatings synthesized with varying amounts of dilution were tested. It was shown that higher dilution from aluminum substrate showed better properties. Although there have been reports on synthesis of coatings and studies of these coatings on mechanical and corrosion response, good understanding of the microstructural evolution during synthesis by rapid quenching processes has not been addressed. Furthermore, using laser processing, composition gradient microstructure can be obtained. Thus, the composition window for the feasibility of synthesizing high entropy alloy phase can be determined.

CHAPTER 2

EXPERIMENTAL PROCEDURES

2.1 Laser Processing

2.1.1 Surface Treatment of Fe-Si-B Amorphous Ribbons Using CW Laser

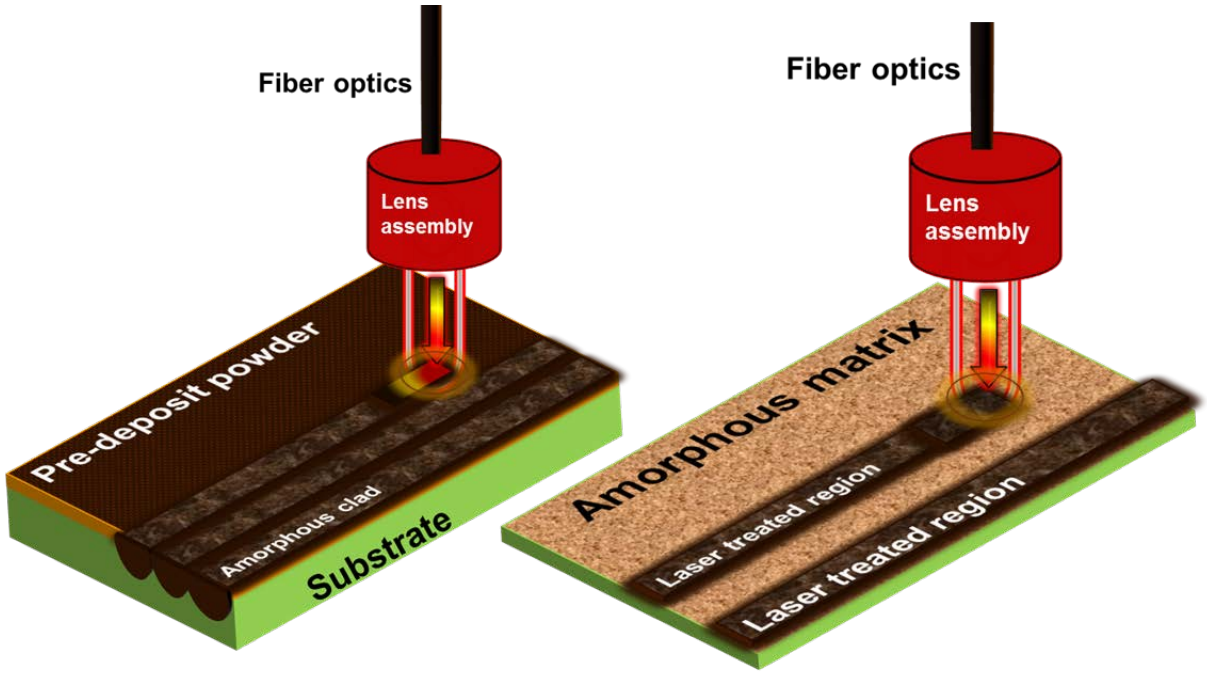

Figure 2.1 Schematic of laser processing

Iron-based amorphous ribbons (Metglas Inc., Product No.: 2605 SA1) with a nominal composition of $Fe_{85–95\%}Si_{5–10\%}B_{1–5\%}$ in atomic percent and thickness of 28μm were used for the laser-patterning/surface heat treatment experiments The laser patterning was carried by scanning parallel tracks with a continuous wave ytterbium doped Nd-YAG laser beam at a wavelength of 1.064 μm. The laser material interaction was studied by varying the laser power density from 0.8 to 0.23J/mm^2. The lateral spacing between the centers of two consecutive laser-scanned tracks was maintained at 5mm, thereby retaining an untreated track of width 2.5mm between consecutive laser tracks.

The experiments for multi-pass laser processing were performed by employing a laser power of 100W and the laser beam was scanned 20 times with a velocity of 500 mm/s resulting in 0.33J/mm^2 laser energy density. The lateral spacing between the centers of two consecutive laser-scanned tracks was maintained at 1mm, thereby retaining an untreated track of width 0.4 mm between consecutive laser tracks.

The magnetic field assisted laser patterning experiments on the amorphous ribbons were performed while the ribbon was rested on a strong Nd-Fe-B magnetic substrate with a surface field value of 0.4 T. Thus, the hard magnet not only acted as a sample support, but also provided an external magnetic field perpendicular to the amorphous ribbon surface. The lateral spacing between the centers of two consecutive laser tracks was maintained at 1mm, thereby retaining an untreated track of 0.4mm width between tracks to reduce the effects of re-heating during subsequent laser passes. A laser power density of 0.33J/mm^2 was used with a power of 100W and scan speed of 500mm/s for the patterning experiments

The sample for conventional furnace annealing was prepared by sealing the sample in a glass tube in an Argon atmosphere, the glass tube was placed inside the furnace at 823K. The heat treatment was done for 1 hour in order to achieve considerable amount of crystallization as short term annealing results in very less amount of phase transformed [84, 85]. The time and temperature of heat treatment are reported in many earlier reports [86, 87, 88]

2.1.2 Laser Synthesis of Amorphous Fe-Cr-Mo-Y-C-B Coating on Steel Substrate

Amorphous alloy powders were prepared by high pressure gas atomization. A mixture of pure elemental powders of Fe, Cr, Mo, Y, C and B (all with greater than 99.9 wt.% purity) with nominal chemical composition of $Fe_{48}Cr_{15}Mo_{14}Y_2C_{15}B_6$ (in at.%) was induction melted under

high purity argon atmosphere and then atomized using high purity He gas. The atomized powders were mechanically sieved to obtain powder within a narrow size range (10–20 μm).

Table 2.1 Laser parameters employed in the present work

Name	Value or Expression [units]	Description
P	1000 [W]	Laser Power
T_{on}	0.333[s]	Residence time or on time
d	1[mm]	Laser beam diameter on the surface of the sample
S	((pi/4)*(d^2))	Surface area of the laser beam
V_{in}	30 [mm/s]	Laser scan speed
P_{in}	P/S*((t<=Ton)*(t>=0)) W/m^2]	Power density of the laser beam
ϕ	D/6 [mm]	Standard deviation
P_g	Pin*exp (-(x-Vin*t)^2/(2*σ^2)) [W/m^2]	Moving Gaussian beam in X direction

The substrate used in the present study for developing amorphous coating was AISI 4130 steel. Rectangular substrate plates (50×25×7 mm^3) (Original dimensions) were sand blasted followed by washing with acetone and methanol to clean and degrease the surface. The amorphous alloy powder was suspended in water soluble organic binderLISI W 15853 obtained from Warren Paint andColor Company (Nashville, TN, USA) to form thick slurry. The slurry was then air-spray deposited on the substrate to a uniform thickness (100 μm) which was subsequently dried at 75 °C for 30min. A 3kW diode pumped Yb-YAG(YLS-3000 IPG) continuous wave fiber laser equipped with a fiber optic beam delivery system was employed for laser processing of amorphous coating on steel substrate. Laser assisted surface melting of the pre-deposited powder layer was carried out with a laser power densities varying from 73 J/mm^2 to 186J/mm^2. The laser parameters employed in the present study (Table 2.1) were derived from number of processing trials that ensured synthesis of uniform coatings with sound metallurgical bonding at the coating/substrate interface.

2.2 Phase Analysis

2.2.1 XRD

Phase analysis for the amorphous coating samples is done by slightly polishing the coating to remove the oxide layer and also to reduce the surface roughness.

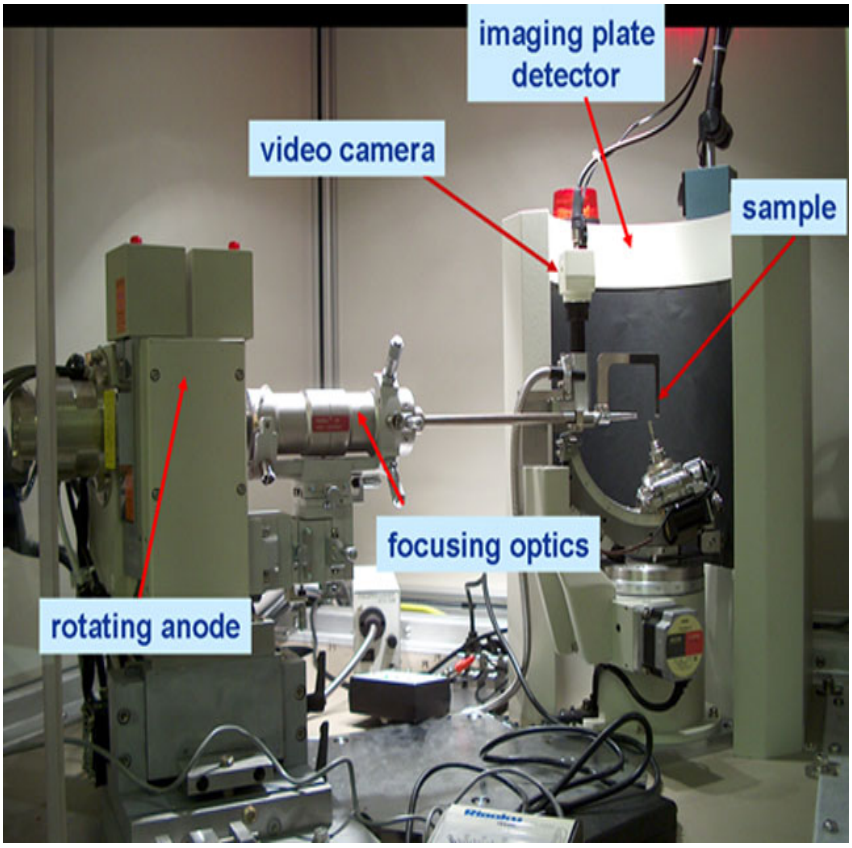

Figure 2.2 Micro-XRD setup used for multi-pass laser processed samples

The phases in the precursor material and laser processed samples were characterized by Rigaku III Ultima X-ray diffractometer (XRD) with Cu K_α radiation of wavelength 0.15418 nm. The XRD system was operated at 40 kV and 44 mA in a 2θ range of 20 - 90° using a step size of 0.025° and a scan speed of 2 degree/minute. The phases present were identified by comparing the XRD spectra with standard ICDD (International center for diffraction data) files obtained from the joint committee of powder diffraction standards (JCPDS). Spatially-resolved micro-XRD was performed for the multi-pass laser heat treated samples using a Rigaku Rapid II system equipped with a rotating Cr anode (35 kV, 25mA, λ = 0.22910 nm) and a 2-dimensional image plate detector. The sample was positioned perpendicular to the 10 μm diameter incident beam

and was moved in 10 μm steps to record patterns across the laser tracks. The phases present were identified by comparing the XRD patterns with standard international center for diffraction data (ICDD) patterns. The micro-XRD setup is shown in the Figure 2.2

2.3 Surface and Composition Analysis

2.3.1 SEM:

Microstructural characterization of the amorphous coatings was conducted by cutting the sample in the cross section at a plane perpendicular to the laser processing direction before mounting the piece using a Bakelite hot mounting powder. The samples were further polished under a grinding machine using 400, 600, 800, and 1200 grit SiC pads. It is followed by polishing the sample on a micro-cloth with aluminum suspension of 1μ, 0.3μ and 05μ particle sizes. The samples were then cleaned in an acetone bath using a ultrasonic cleaner. The steel samples were etched with Nital to reveal micro-structural features of interest under the microscope. Aqua-regia was used as an etchant for the high entropy alloy coatings

2.3.2 LEAP (Atom Probe)

Samples for atom probe tomography (APT) studies were prepared by the focused ion beam milling technique. For this purpose, samples were prepared by dual-beam FIB FEI Quanta 3D FEG system using Ga ion beam. The ion beam thinning was carried out in multiple steps, starting with 30 kV ions, followed by finishing with 5 kV ions to reduce surface damage caused by the higher energy ions [89]. The final tip diameter of the atom probe specimen was ~ (50 – 80) nm. The APT experiments were carried out in voltage evaporation mode with 25% voltage pulse fraction at sample temperature of 40K and evaporation rate of 0.5% using either LEAP 3000XHR or LEAP 4000XHR local electrode atom probe system from CAMECA Instruments Inc. The reconstruction of the APT data was performed using IVAS software and the tip

diameter and shank angle during reconstruction were determined using a high magnification SEM image taken after final milling. De-convolution of overlapping peaks in mass to charge spectra were performed using the ion counts of the non-overlapping isotope peaks. The overlap of Si_{28}^{+1} and Fe_{56}^{+2} peaks in the mass to charge spectrum was de-convoluted using the ionic count of non-overlapping Si_{30}^{+1} isotope peak to estimate the count of Si_{28}^{+1} peak based on expected natural abundance ratio of isotopes.

2.4 Sample Preparation Techniques for Microscopy

2.4.1 Site Specific Sample Preparation Using FIB

The site specific TEM sample preparation was done using FEI Nova 200 Nano Lab dual-beam focused-ion beam. A platinum layer was initially deposited in the electron beam in order to reduce the beam damage. The deposition was done by tilting the stage perpendicular to the ion beam, and the interaction of the Ga ions with the Pt gas source resulted in a uniform deposition of Platinum layer. A beam current of 0.1nA and 30kV voltage was used to deposit ~2μm thick Pt layer. Furthermore, rectangular trenches were made parallel to the length axis to either sides of the Pt deposition. The millings were performed at ion beam voltage of 30 kV and beam current of 7nA. It is then followed by milling out a small portion perpendicular to the Pt deposition and creating a free standing cantilever by cutting the sample below the Pt deposition at zero degree tilt position. A micro manipulator is used to transfer the sample from stage to a Cu grid. The sample was welded onto a post on the Cu grid and further thinned by tilting the sample perpendicular to Ga ion beam. A final thinning is done at 5kV and 0.12-0.23nA to thin the sample till it became electron transparent.

2.4.2 Atom Probe Sample Preparation Using FIB

A similar procedure is adapted to prepare needle shape samples for LEAP analysis. The milling in this case is done at 22 degree tilt of the stage on either side of the Pt deposition to obtain a wedge shaped sample. Subsequently, the needle shape samples suitable for Atom Probe studies are made by a series of milling steps followed by cleaning at 5kV milling. The final diameter of the tips was close to 100 nm.

2.5 Formulation of Thermal Model

The thermal histories were simulated using a finite element (FE) based heat transfer model employing COMSOL^{TM} multi-physics software. Appropriate heat transfer boundary conditions were employed for different boundaries to simulate the thermal histories under various laser processing conditions used to synthesize the coatings.

The model was developed considering the thermo-physical properties using the rule of mixtures. Conduction, convection and radiation phenomena are considered to develop the heat transfer model. A rectangular block with dimensions (25x50x0.7 mm^3) as pre-cursor deposit was built on another rectangular substrate (25x50x0.7 mm^3) and respective materials were selected for the corresponding blocks. A physics-controlled mesh was chosen to model laser processing with maximal element size of 1.38 mm and minimal element size of 0.1 mm for the substrate coating composite. The residence time (t_{on}) of the laser beam is defined by the following equation:

$$t_{on} = \frac{D}{V_{in}} \qquad \text{equation 2.1}$$

Here, D is the laser beam diameter on the surface of the sample and V_{in} is the laser scan speed.

The following equation describes the energy balance between total heat flux and the temperature rise within the sample for a three dimensional geometry.

$$\rho C_p \frac{\partial T(x,y,z,t)}{\partial t} = k\left[\left(\frac{\partial^2 T(x,y,z,t)}{\partial^2 x}\right)+\left(\frac{\partial^2 T(x,y,z,t)}{\partial^2 y}\right)+\left(\frac{\partial^2 T(x,y,z,t)}{\partial^2 z}\right)\right]$$ --------*equation 2.2*

Here, k is the thermal conductivity, C_p is the specific heat and ρ is the density of the material,.

Different boundary conditions are assigned to the surfaces corresponding to different heat transfer phenomena describing the surface during laser processing.

The equation combining all the three boundary conditions heat flux, convection, and surface to ambient radiation is given by

$$-k\left[\left(\frac{\partial T}{\partial x}\right)+\left(\frac{\partial T}{\partial y}\right)+\left(\frac{\partial T}{\partial z}\right)\right] = P_g - \varepsilon\sigma\left[T^4 - T_0^4\right] - h\left[T - T_0\right]$$ ----------*equation 2.3*)

here h is heat transfer coefficient (h=10 for natural convection), ε is emissivity (ε = 0.7 for the pre-cursor deposited powder particles) , P_g is three dimensional Gaussian laser beam distribution, σ is Stefan-Boltzman constant, and T_0 is ambient temperature .

The boundary conditions corresponding to convective heat transfer and surface to ambient radiation is given by the mathematical equation below:

$$-k\left[\left(\frac{\partial T}{\partial x}\right)+\left(\frac{\partial T}{\partial y}\right)+\left(\frac{\partial T}{\partial z}\right)\right] = h\left[T - T_0\right] + \varepsilon\sigma\left[T^4 - T_0^4\right]$$ ----------*equation2.4*

The laser track is assigned a heat flux boundary with a moving Gaussian laser beam with a spatial distribution defined by the following equation 2.5. The position of the beam within the track is governed by the velocity and the time terms in the equation given below.

$$P_g = \left(\frac{P}{\left(\frac{\pi}{4}D^2\right)}\right)\exp\left(-\frac{\left(x - V_{in} * t\right)^2}{\left(2\phi^2\right)}\right)$$ ---------- *equation 2.5*

where P is laser power, x is the distance along the x-axis and ϕ represents the standard deviation of laser beam intensity.

The heat transfer for the laser track is governed by equation 2.3 as it accounts for the irradiation of laser beam as heat flux, convective cooling by air and also radiation heat loss from surface to ambient environment. Similarly, the rest of the boundaries are governed by equation 2.4 that takes into account convection cooling and surface to ambient radiation mode of heat transfer. Different boundary conditions adapted in the model for the present study are shown in the schematic:

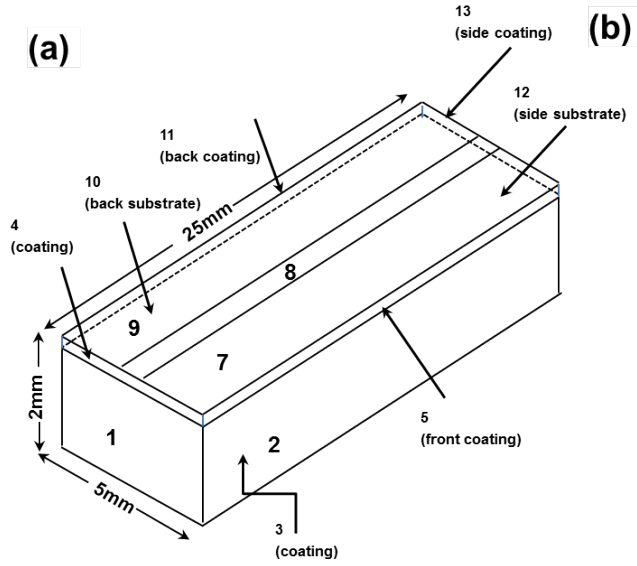

(b)

Boundary #	Boundary Condition 1	Boundary Condition 2
1	Convective Cooling	Surface-to-ambient Radiation
2	Convective Cooling	Surface-to-ambient Radiation
3	Insulation	-
4	Convective Cooling	Surface-to-ambient Radiation
5	Convective Cooling	Surface-to-ambient Radiation
7	Convective Cooling	Surface-to-ambient Radiation
8	Heat Flux	Convective Cooling and Surface-to-ambient Radiation
9	Convective Cooling	Surface-to-ambient Radiation
10	Convective Cooling	Surface-to-ambient Radiation
11	Convective Cooling	Surface-to-ambient Radiation
12	Convective Cooling	Surface-to-ambient Radiation
13	Convective Cooling	Surface-to-ambient Radiation

Figure 2.3 (a) Schematic showing different boundaries used in the model; (b) table showing the corresponding boundary conditions.

CHAPTER 3

LASER THERMAL TREATMENT OF FE-SI-B AMORPHOUS RIBBONS

3.1 Single Pass Laser[1]

The understanding of the laser material interaction is very important to choose appropriate parameters for processing of the ribbons in an industrial scale. Initially the laser material interaction is studied by irradiating the amorphous ribbons with the laser and forming a single line pattern. The laser parameters are optimized to achieve crystallization. It can be observed that the crystallization starts for 0.33J/mm^2 laser energy density below which the material undergoes structural relaxation. The present chapter describes the changes in the microstructure of an amorphous Fe-Si-B alloy after irradiating with a continuous wave laser beam with a Gaussian beam profile. The microstructure evolution across the laser irradiated region is characterized using TEM, and resistivity changes. The microstructure evolution at the edge and center region of the laser track is compared by site specifically making TEM samples using FIB (Focused Ion Beam) techniques. The results are rationalized based on a thermal model developed.

3.1.1 Phase and Microstructure Evolution

The phase evolution was predicted using x-ray diffraction patterns from different Fe-Si-B samples, processed systematically varying the laser energy densities as shown in Figure 3.1. It can be observed that crystallization did not occur for all the laser processed samples and there is a steady increase in the amount of crystallization of the amorphous Fe-Si-B phase (Figure 3.1) with an increase in laser energy density (residence time). Crystallization peak became noticeable

[1] Parts of this section have been previously published, either in part or in full, from (1) Shravana Katakam, Jun Y. Hwang, Hitesh Vora,aSandip P. Harimkar, Rajarshi Banerjee and Narendra B. Dahotre: ScriptaMaterialia (2012), v-66, pp-538 with permission from the Elsevier, and (2) Shravana Katakam, S. Pandian, Hitesh Vora, Narendra Dahotre: Philosophical Magazine Letters (2012) vol-92, pp-617 with permission from Taylor and Francis publishing .

at laser energy density of 0.33J/mm^2. The SEM micrograph of the sample processed with 0.33J/mm^2 indicates a thermal stress at the edge region of the laser track as shown in Figure 3.2.

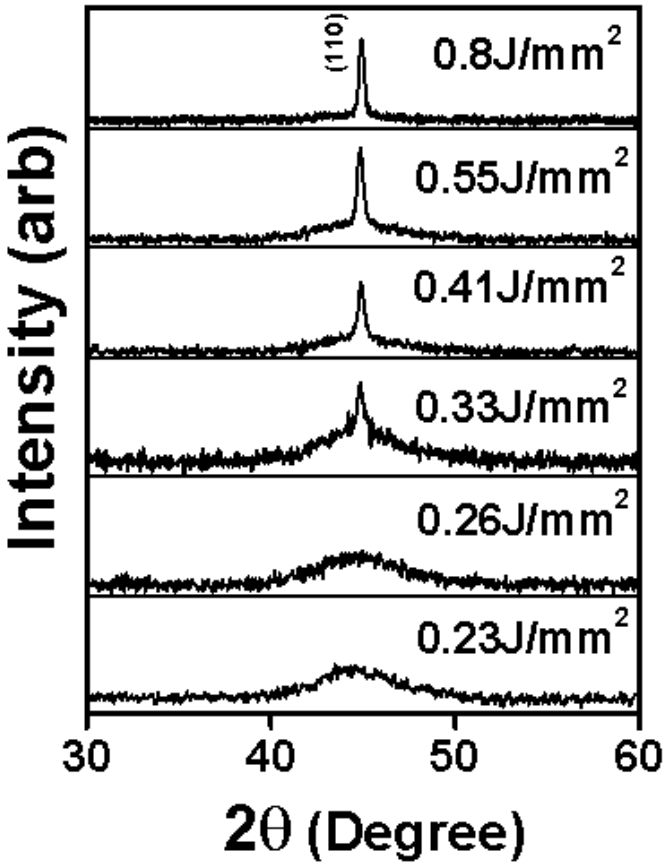

Figure 3.1 XRD scans of laser processed sample

Further analysis of the grain size and morphology was done using transmission electron microscopy (TEM), site-specific dual-beam focused ion beam (FIB) liftouts was used to prepare samples from the edge denoted by region **A**, near edge denoted by region **B** and from the center of the laser track, region **C** as indicated in the schematic (Figure 3.3a) . The corresponding TEM micrographs to the three regions (Figure 3.3b, Figure 3.3c, and Figure 3.3d) are shown respectively. The micrograph from region A (Figure 3.3b) indicates the formation of a completely de-vitrified region consisting of nano-crystalline precipitates within the range of 20-30nm. A selected area electron diffraction pattern from region A is shown as an inset in Figure

3.3b, and the rings in this diffraction pattern can be consistently indexed based on the body-centered cubic (bcc) for α-Fe(Si) phase which is in good agreement with the XRD spectra **(**Figure 3.1**)**.

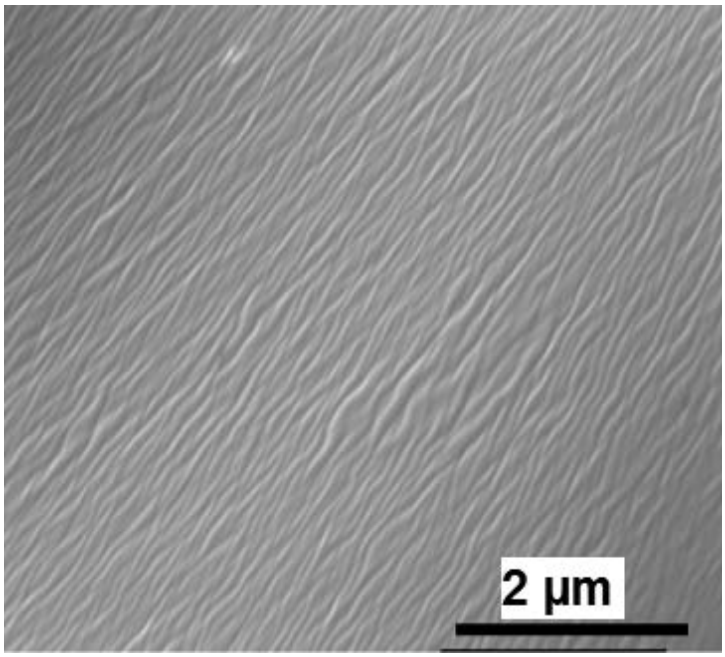

Figure 3.2 SEM micrograph of the edge region for the sample processed with 0.33J/mm^2 laser energy density

In contrast to the microstructure in region A, region B exhibits a composite microstructure consisting of a high number density of refined α-Fe(Si) nanocrystals embedded in a partially untransformed amorphous matrix (Figure 3.3). The diffraction pattern shown as an inset in Figure 3.3c can be indexed based on nanocrystals of the α-Fe(Si) phase embedded in an amorphous matrix and hence the composite nature of the microstructure is realized. The region C at the center of the laser track, consists of predominantly amorphous phase with very low number density of nanocrystals embedded in this matrix (shown in Figure 3.3d).On further analysis of the diffraction pattern shown as an inset in Figure 3.3d, the faint, but sharper, diffraction rings correspond to the same α-Fe(Si) phase and the diffuse rings in the same pattern are indicative of the surrounding amorphous matrix.

Thus a gradual change in microstructure from a uniform nanocrystalline microstructure at the edge of the track to predominantly an amorphous phase, with a small number density of nanocrystals, at the center of the track is clearly visible.

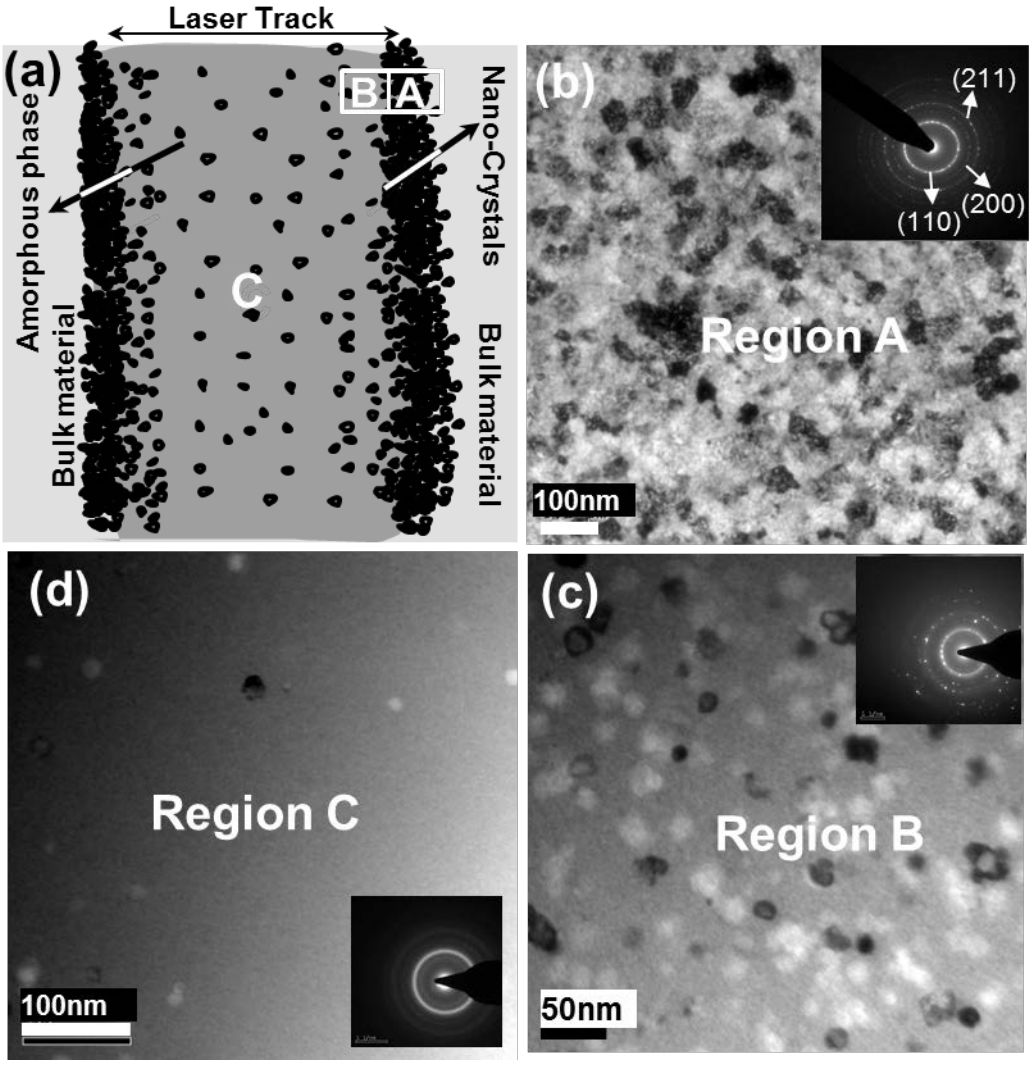

Figure 3.3 Microstructure evolution across laser track (a) Schematic; (b) Bright field TEM from edge; (c) near edge region; (d) center region

This change in microstructure along the width of the laser track can be attributed to the different thermal histories experienced by different regions, due to the nature of the laser beam. The intensity of the beam has a Gaussian distribution due to which the intensity at the center of the beam is maximum and exponentially decreases away from the center. Crystalline phases

form only when the temperature attained is above the crystallization temperature and the kinetics of heat transfer (cooling rate) is appropriate. In light of this, attempts were made to estimate the temperatures and cooling rates and their effects on microstructural evolution during laser processing, through development of a multi-physics based computational model based on heat-transfer mechanisms in COMSOL's^{TM} heat transient mode.

3.1.2 Thermal Effects

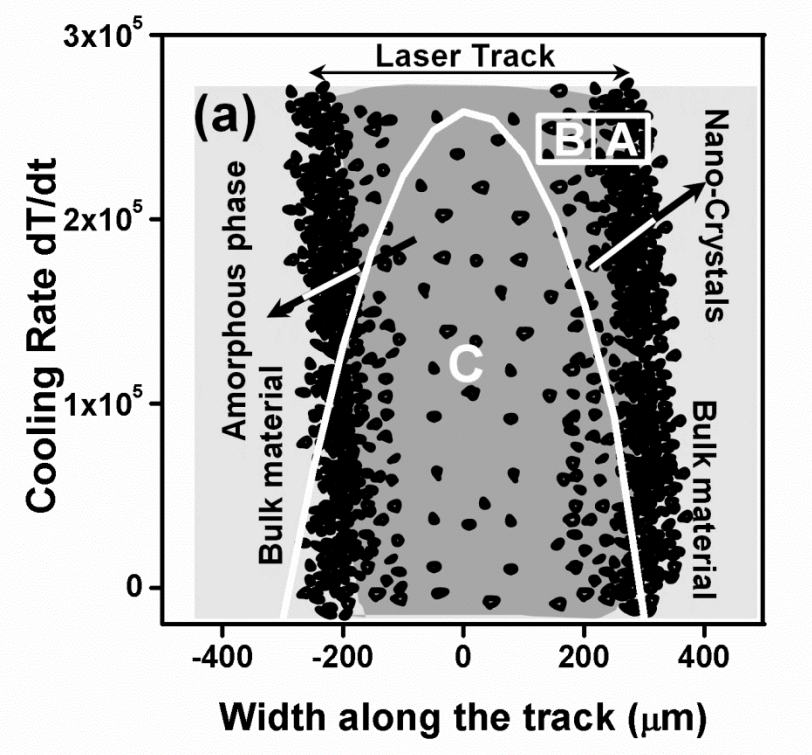

Figure 3.4 Cooling rates along the width of the laser track

The temperature evolution and the cooling rates are predicted using a thermal model developed using COMSOL TM multi-physics software. The details of the model are given in section 2.5. The cooling rates predicted through this model along the width of the laser track are shown in Figure 3.4. The average peak temperature reached during processing at the edge

(511±11K) is different compared to the center (808±23K) of the laser track, as predicted by the computational model (Figure 3.5).

While the heat-transfer model, described in the previous paragraph, is successful in predicting the temperature profile and the cooling rates associated with different spatial locations along the laser track, this information needs to be coupled with thermodynamic-kinetic models to predict the resulting crystallization behavior.

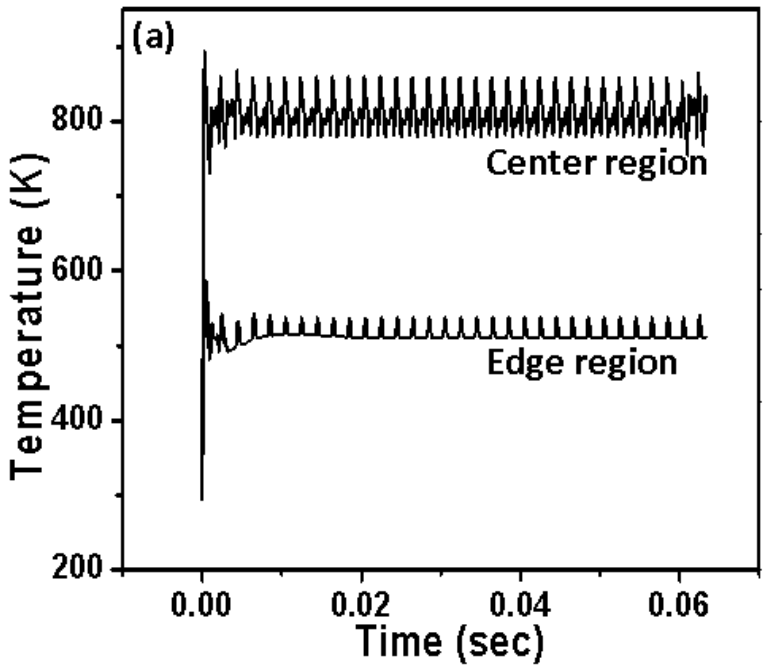

Figure 3.5 Temperature evolution at center and edge of the laser track

The resultant crystallization kinetics can be explained by the classical-Johnson-Mehl-Avrami(JMA) model given by the following equation [h]

$$f = 1 - \exp(-kt^n)$$ ----------equation 3.1

where,f is the volume fraction of the transformed phase, t is the time and k denotes the rate constant of the transformation and n is the Avrami exponent. The temperature dependent rate constant is given by

$k=k_{0.}\exp(-E_g/RT)$----------equation 3.2

$$\text{where}k' = \frac{dk}{dT}\left(\frac{dT}{dt}\right) = \left(\frac{\alpha E_g}{RT^2}\right)k$$ ----------equation 3.3

and the temperature is assumed to vary linearly given by equation (5)

$T=T_0+\alpha t$ ----------equation 3.4

As the heat transfer is dynamic, differentiating equation (1) and integrating within the limits of residence time t gives

$$\int_0^f \frac{1}{1-f}df = \int_0^t n(kt)^{n-1}[k + \acute{k}T]dt$$ ----------equation 3.5

Solving equations (4), (5) and (6) and substituting the values of k_0(frequency factor)=2.7366sec^{-1}[90], t(residence time)=10^{-6} sec, E_g(activation energy)=260kJmol^{-1}, T=808K, and solving for f gives f =0.024 which is indicative of low crystallization density within center region of laser track (Figure 3.3d). On the contrary, the volume fraction transformed was not calculated for the edge region, as the average temperature reached (511$\pm$11K) is below the reported crystallization temperature (780K).

The crystallization temperature for the formation of α-Fe(Si) phase in amorphous Fe-Si-B, based on DSC experiments, has been reported to be ~780K [91]. Additionally, in situ hot stage TEM studies on an Fe-Si-B-Cu alloy, indicate a crystallization temperature ~583 K for the formation of the α-Fe(Si) phase [92]. The decrease in the crystallization temperature in the second case can be attributed to the presence of Cu in Fe-Si-B which leads to a high number density of α nucleation sites [93]. Furthermore, a low activation energy (~260kJ mol^{-1}) has been reported for the formation of the αFe(Si**)** phase [92]. In addition, an Avrami index of 3 has been associated with the formation of αFe(Si) suggesting that this phase forms rather rapidly and does

not involve any long range diffusion in the amorphous matrix [92]. In the present study, the temperature experienced by the center of the laser track is 808 $\pm$ 23 K that is above crystallization temperature, while that at the edge of the track is 511 $\pm$11 K**,** as predicted by the heat transfer model (Figure 3.5) [91, 92].

However, there is a substantial difference in the cooling rates experienced by these two regions, with the center of the track cooling at a rate ~ $3x10^5$ K/s, while the edge cools at ~ $1x10^5$ K/s (Figure 3.4). Therefore, the extremely high cooling rate at the center of the track (region C) severely restricts even short-range diffusion and consequently only a small number of crystallites of α-Fe(Si) are observed (Figure 3.3d). Considering a cooling rate of $3x10^5$ K/s, the time required for the center of the track to cool from 808K to the crystallization temperature of 780K is ~$9.3x10^{-5}$s. Previous reports exhibit a large number density of α crystallites on annealing amorphous Fe-Si-B alloys at the crystallization temperature for periods ~ 8 mins (480s) [94]. Hence the formation of fine nanocrystals can be attributed to rather limited growth of the quenched in nuclei in the amorphous matrix.

It is interesting to note that the edge of the laser track (region A) develops a completely de-vitrified or crystallized microstructure, consisting of ~20-30 nm α grains, despite the fact that this region experiences a maximum temperature ~511K, substantially below the crystallization temperature (~780K). The formation of such a completely crystallized microstructure can be attributed to thermally-induced compressive stresses. Previous reports, based on high resolution TEM (HRTEM) studies, indicate that the reduction in excess free volume has a direct influence on the transformation of an amorphous phase to a nanocrystalline phase [95]. In the present work, due to thermal expansion, the material at the interface between the laser processed and unprocessed regions is likely to experience a compressive force, resulting in the formation of a

dense and homogeneous distribution of nanocrystalline grains (Figure 3.3b) [95]. Thus, in addition to a decrease in activation energy, the presence of stress at the interface is also an important factor contributing to the formation of a continuous nanocrystalline layer along the edge of the laser track. The development of such diverse microstructures, resulting from various thermal conditions generated by the selection of appropriate laser processing parameters, can influence the desired functional properties of these amorphous Fe-Si-B alloys.

3.1.3 Stress Induced Phase Transformation

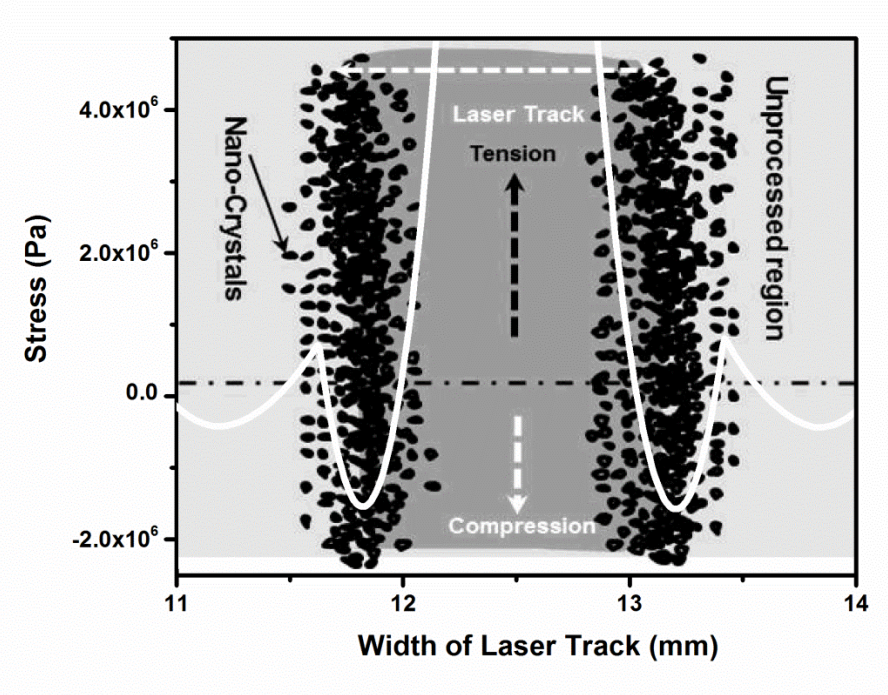

Figure 3.6 Thermal stresses along the width of the track

It must be noted that the laser beam has a Gaussian distribution of intensity which results in inhomogeneous heating across the laser beam diameter and consequently within the laser track on the material. The laser energy density decreases exponentially in the radial direction and has a maximum value at the center. The center of the laser track being at highest temperature and due to negative temperature gradient from the center to the edge of the track, the irradiated region at

the center of the laser track, experiences a tensile thermal stress. On the other hand, the region near the edge of the track, which is also the interface between the laser processed and unprocessed region, suffers a compressive stress. In order to evaluate the thermal histories and also the magnitude and nature of thermal stress (tensile or compressive), a Finite Element Analysis (FEA) based heat transfer model was developed using COMSOL^{TM} multi physics software. The details of the heat transfer boundary conditions and physical constants used in this model are given in section 2.5. The thermal stresses developed due to heat transfer are governed by the following equation:

$$\sigma = \frac{E\alpha}{1-\nu}[T_i - T_f]$$----------equation 3.6

where σ-thermal stress, E-Young's modulus (100 GPa) [96], ν-Poisson's ratio 0.3 [96] and α-coefficient of thermal expansion [$7.6x10^{-6}/^{0}C$][96] and T_i and T_f are initial and final temperatures. The model results indicate that the temperature attained at the center of the laser track (~808 ± 23K) (Figure 3.5) is above glass transition temperature whereas the temperature attained at the edge of the laser track (511± 11 K)(Figure 3.5) is well below the glass transition temperature. Furthermore, the numerical model based computations indicated that the center of the laser track experiences a tensile thermal stress while the interface between the processed and un-processed region experiences a compressive stress (Figure 3.6). The intermediate region experiences a gradual decrease in the value of thermal stress from center to the edge of the track and results in partial crystallization (Figure 3.3c).

Previous reports on indentation studies [97] and bending experiments [98][8] indicate that phase transformation from amorphous to crystalline phase is observed in the presence of a compressive stress. It was proposed that the transformation is due to enhanced atomic mobility across the shear band. It is also well known that most of the transformations are diffusion-driven

and for diffusion to occur, it requires excess free volume within the amorphous phase for the atoms to move either over shorter or longer distances. The excess free volume, which is considered as the analog of vacancies in crystalline materials, controls diffusion rate in amorphous materials. The diffusion in metallic glasses or any amorphous material depends upon the amount of excess free volume, as amorphous materials do not contain defects like vacancies that aid in diffusion. The diffusion in amorphous materials is assumed to be due to stretching of bonds by the neighboring atoms, thus providing a pathway for atomic migration, similar to interstitial diffusion in crystalline materials.

Thus, the excess free volume does influence the diffusivity of atoms and with an increase in free volume, the diffusivity of the components in the amorphous phase increases. Since plasticity in amorphous materials is usually mediated via localized shear bands, comparable to dislocation-mediated plasticity in crystalline materials, when the stress within an amorphous material increases beyond a critical value, shear bands are formed. It has been previously reported and proven that shear bands contains homogeneously distributed excess free volume [95] and thus it is logical to assume that diffusion will be pronounced within these shear bands. The SEM micrograph (Figure 3.2) indicates a large number of shear bands propagated near the edge of the laser track (compressive region) and it can be anticipated that this region experiences a large increase in free volume resulting in enhancement of diffusion. Furthermore, the TEM analysis shows a phase transformation from amorphous to crystalline phase in this region as discussed previously in this letter. The generation of compressive stresses (-1.5 MPa), due to the local thermal expansion near the edge of the laser track, coupled with the fact that the relatively high temperature (513K) further reduces the local yield stress [99], facilitates the initiation and propagation of the shear bands. It can be further noticed from the modeling efforts described

above that the compressive region extends to a distance about 400 μm from the interface between the processed and un-processed region (Figure 3.6). It has been reported elsewhere that the size effects play a significant role in initiation and propagation of shear bands [100] and in the present case, due to a large size of the region of the compressive stress near the edge of the laser track, the stress-induced deformation is very rapid and the deformation is expected to be via rapid propogation of shear bands at the edge of the track. In contrast, the center of the laser track experiences a temperature above the glass transition temperature, and also experiences a tensile stress arising from the local temperature gradient, resulting in more homogenous plastic deformation retaining the amorphous phase. Although, the temperature reached at the center is above crystallization temperature no significant phase transformation was observed and the crystallization kinetics was explained in the earlier section by the classical Johnson-Mehl-Avrami model. Based on a JMA model, the volume fraction of nanocrystals was estimated and these computations were in good agreement with the TEM observations. The excess free volume generated due to the tensile stress is compensated by the annihilation of free volume due to temperature rise resulting in collective motion of atoms. Thus in contrast to the material at the center of the laser track the material in the edge region of the laser track suffers inhomogeneous deformation leading to phase transformation due to propagation of shear bands.

In case of a crystalline solid, the diffusion is controlled by jumping of the atom from one lattice site to another due to vibration energy that involves instantaneous rearrangement of neighboring atoms to create space for the jumping atom to migrate to another position. The enhancement of diffusion in the presence of excess free volume can be rationalized based on the fact that an increase in empty space decreases the energy required for the migration of the atom, i.e. the activation energy for migration is reduced. Furthermore, in the presence of a compressive

stress, the local shear experienced by the atoms results in structural reordering. This structural re-ordering further decreases the activation energy and as a consequence diffusion is enhanced.

If the diffusion of atoms is assumed to be a random walk process, involving uncorrelated jumps, and the diffusion length is assumed to be the size of nano-crystals, then the radius of nano-crystals, diffusivity and time can be correlated in the following manner:

$$R = (Dt)^{0.5} \text{----------equation 3.7}$$

where D is the diffusivity, t is the time taken (residence time) and R is the radius of the nano-crystal. From the TEM micrograph (Figure 3.3) the average nano-crystal size is ~20nm. Hence, by substituting this value in equation 3.7 provides the diffusivity (D) value of the Fe atom to be $4x10^{-13}m^2s^{-1}$. Furthermore, the activation energy for self-diffusion of Fe atom in the amorphous matrix can be calculated using the following equation [101].

$$D = D_0 \exp(-E_a/K_B T) \text{----------equation 3.8}$$

here E_a is the activation energy for self-diffusion jump, K_B is the Boltzmann constant, T is the temperature of transformation and D_0 (4.6×10^{-5}) is the pre-exponential factor which has been reported for self-diffusion of Fe in amorphous Fe-Si-B [102]. The calculated value of the activation energy for the diffusion jump of Fe atom obtained by substituting the constants in the above equation is 0.7eV. This calculated value is substantially lower than the earlier reported value of 2.10 eV [102] which does not account for the role of stress. The lower activation barrier for diffusion can be attributed to structural rearrangement of atoms due to localized shear.

3.1.4 Summary

A homogeneously devitrified nano-crystalline microstructure is observed at the interface between the processed and un-processed regions at the edge of the laser track, while predominantly an amorphous phase is observed at the center of the laser track. Furthermore, the

microstructural evolution at the center of the laser track has been rationalized based on a multi-physics based computational thermal model capable of predicting the maximum temperatures and cooling rates across the width of the laser track. The microstructural evolution at the edge has been correlated to the nature of thermal stresses developing during laser processing. The development of these stresses, in turn, have been rationalized based on predictions of the temperature and cooling rates at different locations along the laser track, afforded by a thermal model. The retention of an amorphous phase in the regions experiencing a tensile stress state while de-vitrification occurs in the regions experiencing a compressive stress state are in good agreement with experimental observations. The enhanced diffusivity in the compressive regions, at the edge of the laser track, can be attributed to a substantial decrease in computed activation barrier for diffusion. Thus, laser processing can be employed as a very effective technique for site-specific stress-induced nano-crystallization of amorphous materials.

3.2 Multi-Pass Laser Processing[2]

3.2.1 Phase Transformation and Microstructural Evolution

The DSC results of the as received amorphous ribbon indicate the presence of two strong exothermic peaks at ~780 K (T_{x1}) and ~830 K (T_{x2}) (Figure 3.7) respectively. This is indicative of the decomposition of the amorphous phase through two crystallization events. The first crystallization temperature corresponds to the formation of the primary BCC α-Fe(Si) phase and the second crystallization peak corresponds to the formation of intermetallic phases. It has been reported that the initial amorphous phase decomposes into primary α-Fe(Si) and Fe_3B intermetallic and further decomposition of metastable Fe_3B phase occurs to Fe_2B [103,104]. The

[2] Parts of this section have been previously published, either in part or in full, from Shravana Katakam, Arun Devaraj, Mark Bowden, Daniel Perea, S.Santhanakrishnan, Cassey Smith, Raju Ramanujan, Rajarshi Banerjee, Theva Suntharampillai and Narendra Dahotre:.Journal of Applied Physics (2013), Vol-114, page-184901 with permission from American institute of Physics

peaks corresponding to the formation of Fe_3B and the transformation from Fe_3B to Fe_2B overlap and hence only two exothermic peaks are observed in the DSC curve

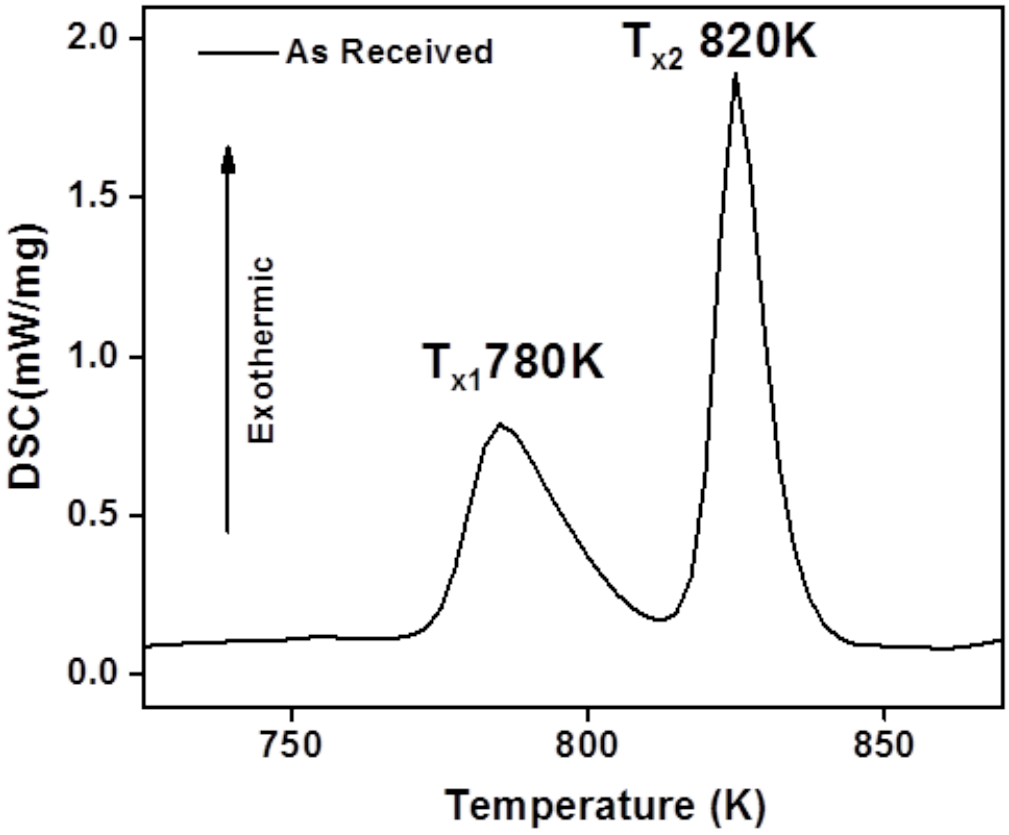

Figure 3.7 DSC of as received amorphous ribbon

The formation of these phases is further confirmed by XRD and TEM analyses discussed in the following section. XRD results from the furnace-annealed and laser-annealed Fe-Si-B ribbons, shown in Figure 3.8a, reveal the formation of the BCC α-Fe(Si) phase along with the Fe_2B phase. In addition to phase analysis, the crystallite size distribution and also the volume fraction transformed across the laser-annealed region were evaluated using micro-XRD (Figure 3.8c and Figure 3.8d). The area of the α-Fe(Si) (200) peak increases towards the edge of the laser track compared to the center, as seen from the XRD pattern (Figure 3.8d). It is also worth noting that significant peak intensity of α-Fe(Si) phase is observed in the unprocessed region (Figure

3.8). The average crystallite sizes were estimated in the laser annealed regions using the Scherer equation.

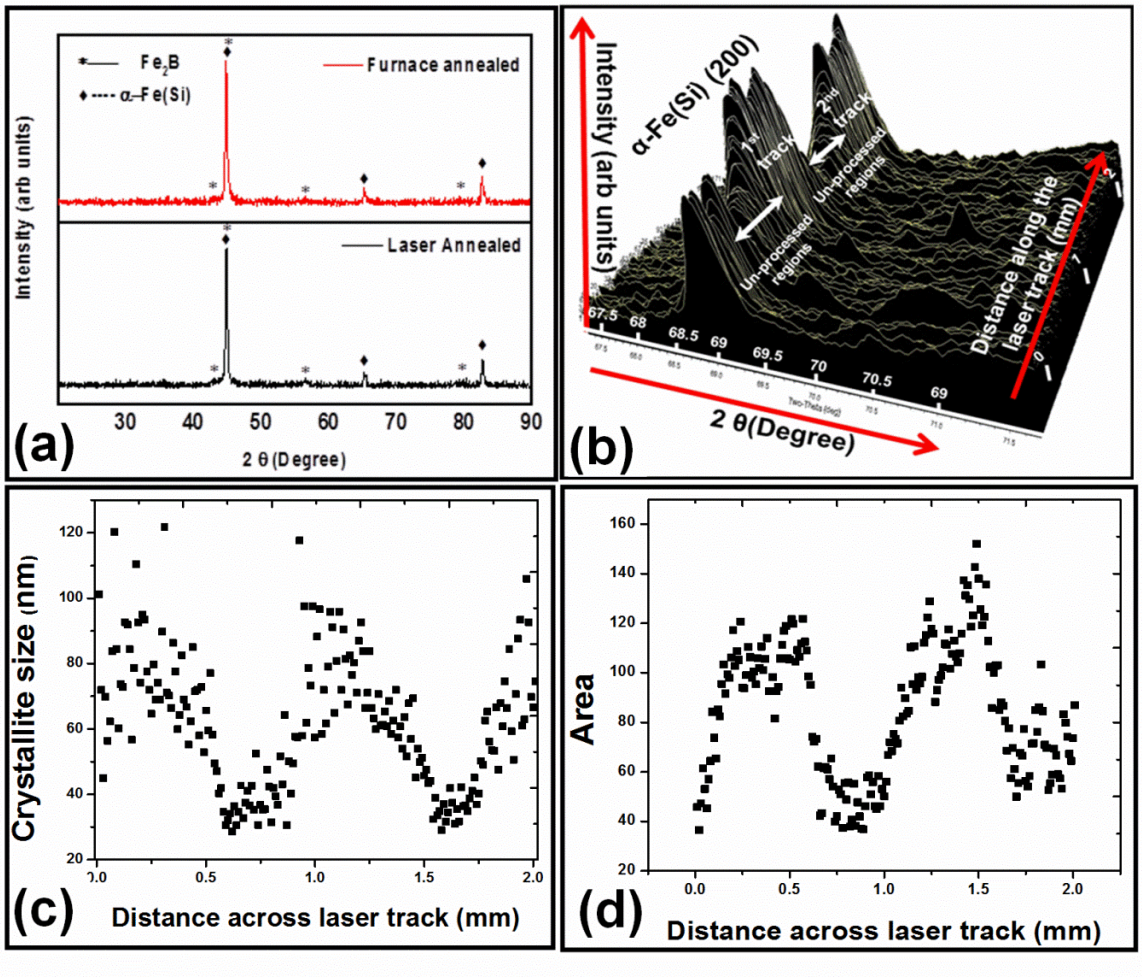

Figure 3.8 (a)XRD patterns; (b) Micro-XRD spectra corresponding to laser annealed sample across laser track; (c) crystallite size distribution across laser track; (d) area of the 200 peak across the laser track

The crystallite size at the laser annealed region was higher having a mean crystallite size of 70nm with a standard deviation of 16 compared to the unprocessed region having a mean crystallite size of 35nm with a standard deviation of 4. In addition, the presence of BCC α-Fe(Si) and Fe_2B phases is further confirmed from the TEM diffraction patterns shown as insets in Figure 3.9a and Figure 3.10a respectively in both laser-annealed as well as furnace-annealed samples

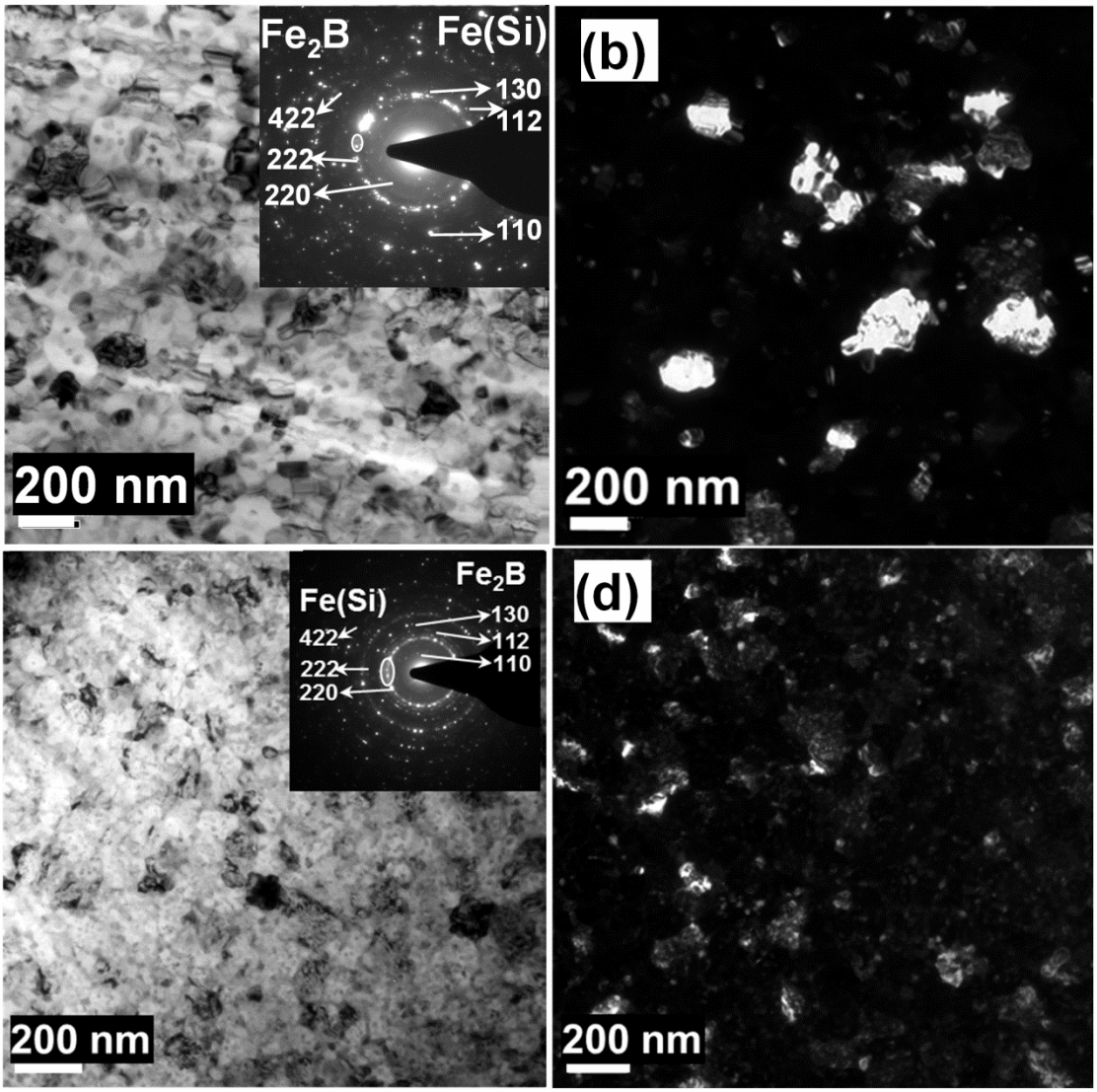

Figure 3.9 TEM micrograph of laser annealed sample. (a) bright field image with corresponding SAD of center region of laser track; (b)dark field image of center region of laser track; (c)bright field image with corresponding SAD of edge region of laser track; (d)dark field image of edge region of laser track

Furthermore, the analysis of morphology and distribution of different phases was also carried out using TEM analysis, as discussed in the following section. The distribution of phases and the respective crystallite sizes have a strong influence on the magnetic properties. TEM bright field images and corresponding diffraction patterns show that significant crystallization took place after laser annealing (Figure 3.9a,c). The average precipitate size was estimated by

measuring individual precipitate sizes employing commercially available ImageJ software. The TEM micrographs reveal a clear difference in the crystallite size between the furnace-annealed sample (average particle size ~100nm) (Figure 3.10) compared to the laser-annealed sample (70nm) (Figure 3.9). In addition, the equiaxed morphology is associated with the laser-annealed sample (Figure 3.9), whereas the furnace-annealed sample exhibits precipitates with a dendritic morphology (Figure 3.10)Further, the laser-annealed sample exhibits a wide distribution for precipitate size (~20nm-200nm) in both center and the edge of the laser track (Figure 3.9). It can be seen from the XRD (Figure 3.8a) and TEM analyses (Figure 3.9a,c and Figure 3.10a) that Fe_2B and α-Fe(Si) are the major crystallization products in both laser-annealed and furnace-annealed samples.

Although the temperature at the edge region of the laser track is less than the temperature attained at the center region of the laser track, significant crystallization is observed in both the center and edge regions as seen from the electron diffraction pattern (Figure 3.9a,c).

This is attributed to the steep thermal gradient and associated distribution of thermal stresses due to the Gaussian beam distribution of the laser beam intensity. The presence of stresses is likely to alter the amount of free volume and also the diffusion kinetics, leading to rapid crystallization as discussed earlier in section 3.1.3. It has been reported earlier that the phase fraction transformed in the edge region longer than that at the center of the laser track for isolated single laser pass. Similarly, in the present case, it is likely that the phase fraction transformed is greater towards the edges of the laser track for multi-pass laser processing. This could be the reason for increase in area fraction of the crystalline peak (Figure 3.8d) at the edge of the laser annealed region. Thus, an increased fraction of amorphous material was transformed to the crystalline phase (due to enhanced diffusion kinetics). It has been reported from first principle calculations that the

Fe_2B phase has a reduced magnetic moment due to anti-ferromagnetic exchange interactions [105].

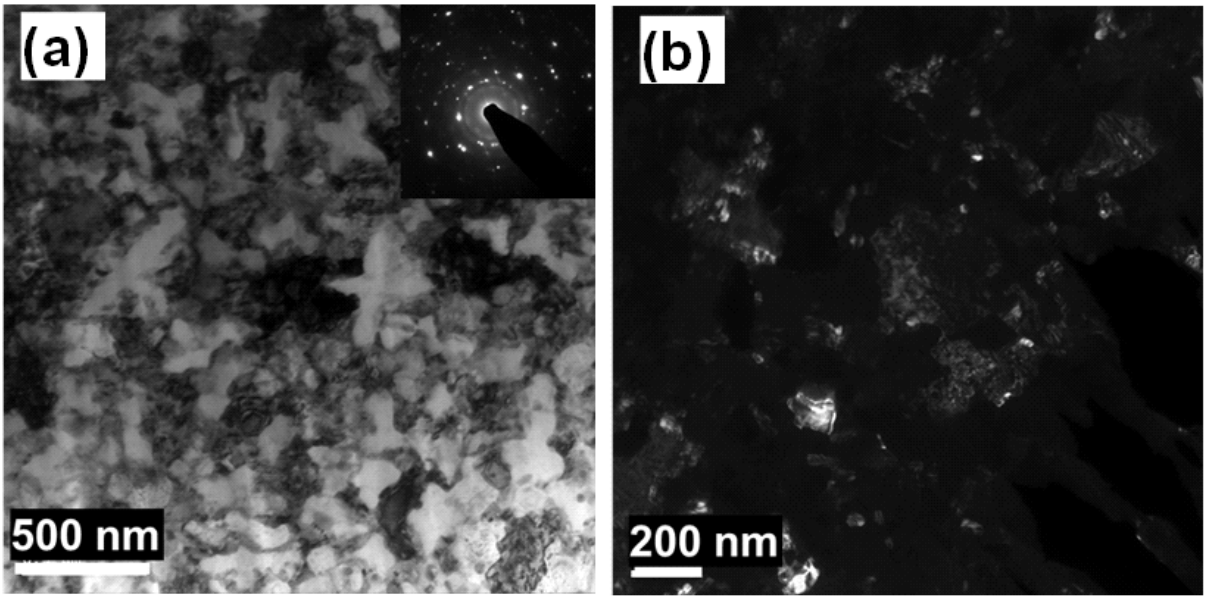

Figure 3.10 TEM micrographs of furnace annealed sample. (a) bright field image with corresponding SAD image and (b)dark field image

Hence, the presence of Fe_2B reduces the saturation magnetization due to an overall reduction in magnetic moment

It can be seen from the XRD (Figure 3.8a) and TEM analyses (Figure 3.9a,c and Figure 3.10a) that Fe_2B and α-Fe(Si) are the major crystallization products in both laser-annealed and furnace-annealed samples. Although the temperature at the edge region of the laser track is less than the temperature attained at the center region of the laser track, significant crystallization is observed in both the center and edge regions as seen from the electron diffraction pattern (Figure 3.9a,c). This is attributed to the steep thermal gradient and associated distribution of thermal stresses due to the Gaussian beam distribution of the laser beam intensity. The presence of stresses is likely to alter the amount of free volume and also the diffusion kinetics, leading to rapid crystallization [18]. It has been reported earlier that the phase fraction transformed in the edge region longer than that at the center of the laser track for isolated single laser pass [17].

Similarly, in the present case, it is likely that the phase fraction transformed is greater towards the edges of the laser track for multi-pass laser processing. This could be the reason for increase in area fraction of the crystalline peak (Figure 3.8d) at the edge of the laser annealed region. Thus, an increased fraction of amorphous material was transformed to the crystalline phase (due to enhanced diffusion kinetics). It has been reported from first principle calculations that the Fe_2B phase has a reduced magnetic moment due to anti-ferromagnetic exchange interactions [105]. Hence, the presence of Fe_2B reduces the saturation magnetization due to an overall reduction in magnetic moment. The transformations are accompanied via partition of different alloying elements, as investigated using atom probe tomography (APT).

3.2.2 Thermal Modeling

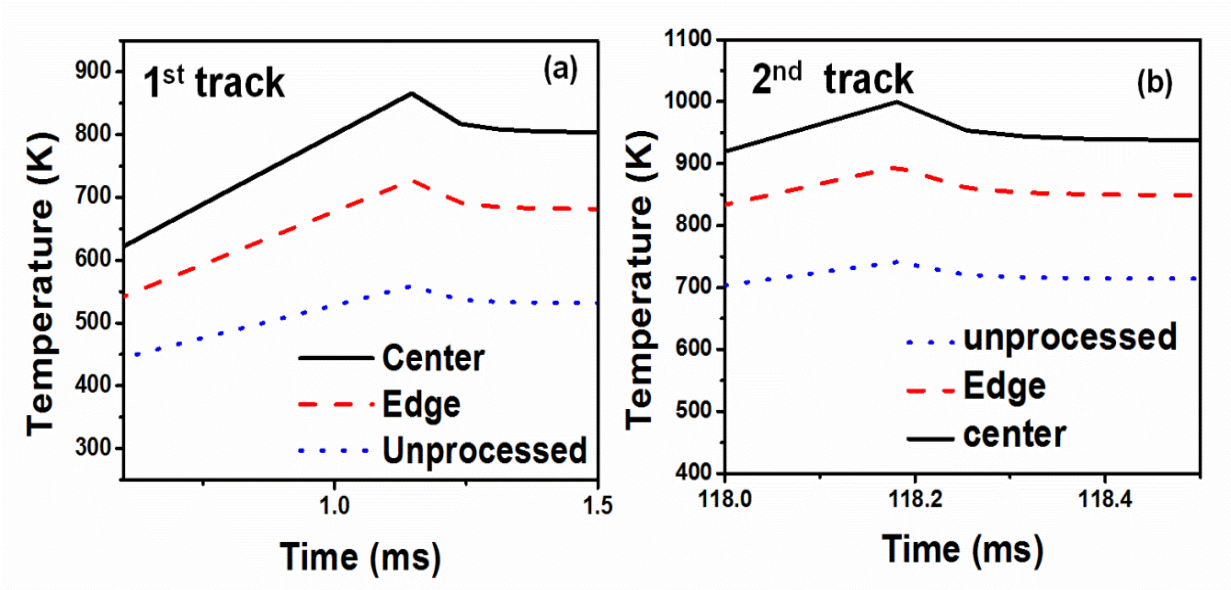

Figure 3.11 Peak temperatures predicted by the thermal model (a) first laser track; (b) second laser track

Using a computational model, the thermal histories have been generated at the center region, edge region and the region, between the consecutive tracks. It can be clearly seen that the peak

temperature (~850 K) at the center of the laser track for the first laser track reaches above the crystallization temperature (780 K) and lower temperatures (~720 K) are obtained at the edge of the laser track (Figure 3.11a).

Table 3.1 Comparison of properties for different processing conditions

Property	Furnace annealing	Laser annealing	As received
Coercivity H_c (Oe)	64	37	0.45
Saturation magnetization (emu/g)	155	175	136
M_r/M_s	0.42	0.37	0
Heating rate (K/s)	isothermal	$6x10^3$	NA
Cooling rate (K/s)	Air cooled	$1.3x10^3$	NA

The temperature profiles generated for the second laser track indicate a substantial increase in temperature above crystallization temperature (780 K) both at center region (950 K) as well as at the edge region (850K) of the laser track (Figure 3.11b). Moreover, it can be noted that the temperature in the unprocessed region (~760 K) is close to the primary crystallization temperature (780 K) (Figure 3.11b) for the second laser track. This explains the low intensity in micro-XRD data for the un-processed region between two consecutive laser tracks (Figure 3.8b). In addition to temperature evolution during laser annealing, the heating and cooling rates are also estimated using the thermal model (Table 3.1). The high cooling rates experienced during laser annealing (10^3K/s) (Table 3.1) are expected to have a strong influence on the partitioning of silicon as explained subsequently in this paper.

3.2.3 Compositional Effect on Magnetic Property

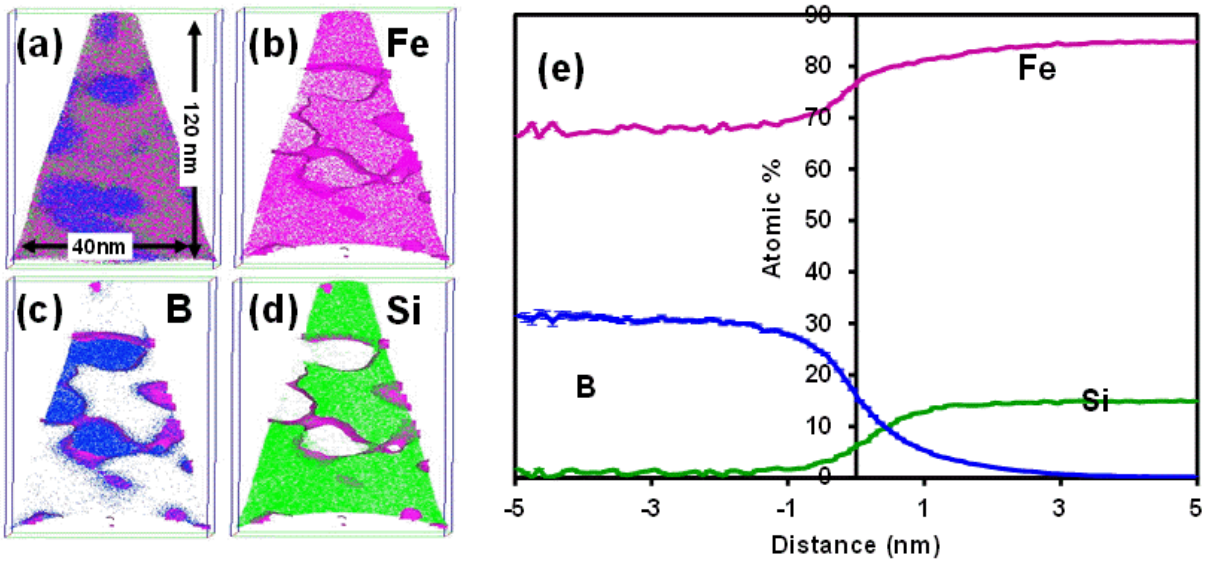

Figure 3.12 Atom probe reconstruction from the edge of laser track with (a)all ions; (b)slice view of tip with iron ions; (c) slice view of tip with boron ions; (d)slice view of tip with silicon ions; (e) proximity histogram across 80 at% iso-surface

The APT results from edge and center regions of the laser track show clear segregation of B and Si to these distinct regions within the reconstructed volume (Figure 3.12,Figure 3.13). A suitable isoconcentration (isosurface) is choosen in such a way that it delineated both the phases, and then a proximity histogram is generated across the interface to determine partitioning of the elements into the respective phases [106,107]. The 80 at% Fe isocomposition surface delineating the boundary between boron rich regions and silicon rich regions within the reconstruction are shown in Figure 3.12(b-d) and Figure 3.13(b-d). For better understanding of elemental distribution a 5nm slice of the entire APT reconstruction is shown with Fe ions (Figure 3.12b,Figure 3.13b), B ions (Figure 3.12c,Figure 3.13c) and Si ions (Figure 3.12d,Figure 3.13d) overlaid on the 80 at% Fe isocomposition surface. A proximity histogram plotted perpendicular to the 80at% Fe isocomposition surface is used to quantify the compositional partitioning between the B rich regions and Si rich regions. It can be observed that within the laser track

(center and edge regions) boron concentration reaches ~33 at% (Figure 3.12e,Figure 3.13e) which is equivalent to the Fe_2B composition, in agreement with the XRD results. .

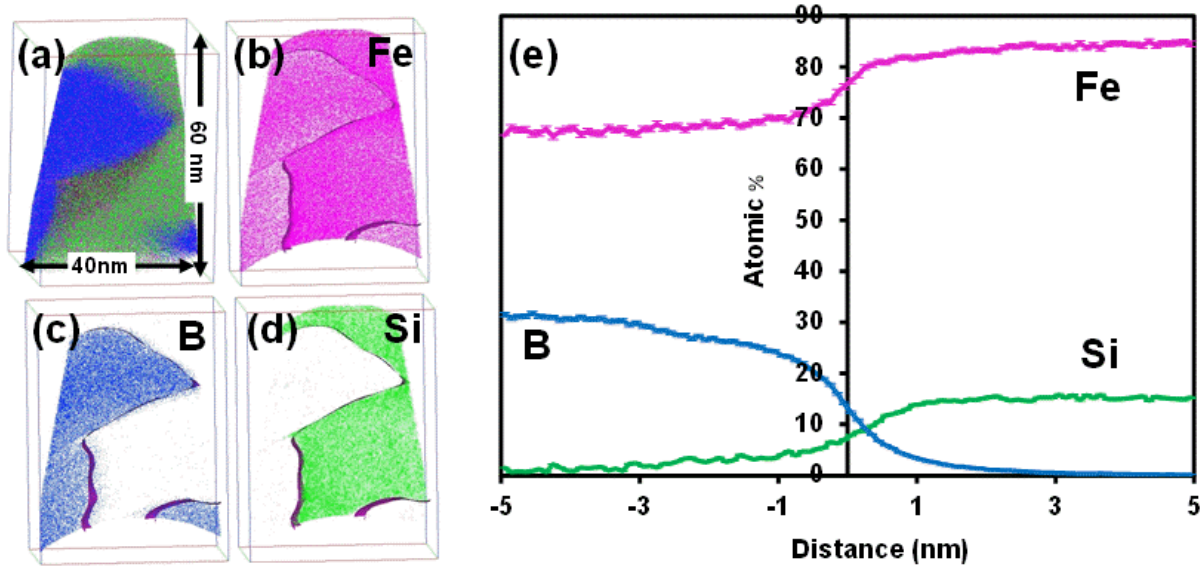

Figure 3.13 Atom probe reconstruction from the center of laser track with (a) all ions; (b)slice view of tip with iron ions; (c) slice view of tip with boron ions; (d) slice view of tip with Si ions; (e) proximity histogram across 80 at% iso-surface

Similarly it can also be observed that the silicon concentration is about 15 at% in the α-Fe(Si) phase for both at the edge region as well as at the center region of the laser track (Figure 3.12e,Figure 3.13e). The atom probe analysis for the furnace annealed sample also revealed the formation of silicon rich and boron rich phases (Figure 3.14a). The segregation of alloying elements is further emphasized in the 5nm slice view (Figure 3.14(b-d)). The isoconcentration surface at 77at% of iron delineates the boron and silicon rich phases; a proximity histogram is generated across the interface to quantify the compositional partitioning. Although boron concentration (32 at%) in the boron rich phase is similar to Fe_2B region concentration in laser annealed sample, the partitioning of silicon (~20 at%) (Figure 3.14e) to the α-Fe(Si) phase shows a significant change compared to the silicon partitioning in the laser annealed samples (~15 at%).

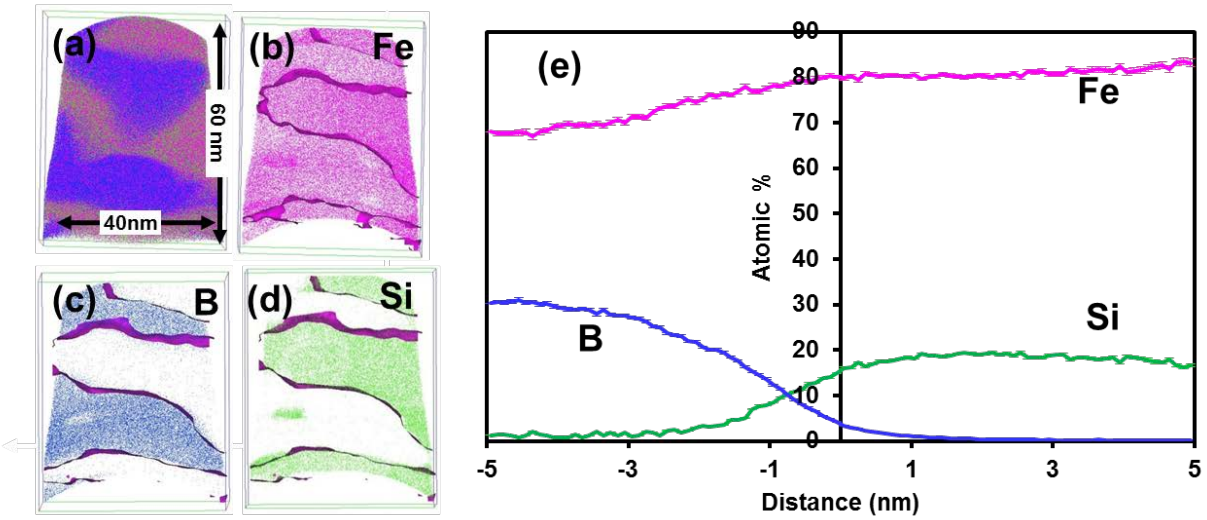

Figure 3.14 Atom probe reconstruction from the furnace annealed sample (a)all ions ;(b)slice view with iron ions ;(c) slice view with boron ions ;(d) slice view with silicon ions ;(e) proximity histogram across 77 at% iso-surface

The evolution of microstructure and the partitioning behavior can be explained in terms of difference in their thermal histories. The thermal histories during laser annealing have been evaluated using a thermal model and the results are discussed in the next section. The saturation magnetization and magnetocrystalline anisotropy of α-Fe(Si) depends on the solute content. Although boron has very little solubility in the BCC α-Fe phase, silicon can partition into the α-Fe phase. It has been reported that the partitioning of silicon into primary α-Fe is lower during initial stages of crystallization but as annealing progresses, more and more silicon partitions into the α-Fe phase. When the Si concentration reaches about 20 at% of silicon, chemical ordering takes place resulting in the degradation of saturation magnetization and magnetostriction [108]. It is also reported that lower concentration of silicon increases the saturation magnetization and reduction in saturation magnetization starts to occur above 16 at% of silicon [109]. Simulations based on density functional theory (DFT) indicate that the magnetic moment of iron decreases with the increasing number of silicon atoms as nearest neighbors. Thus with an increase in

silicon concentration in the α-Fe phase, the magnetic moment of one iron lattice site decreases due to hybridization between iron-d orbitals and silicon s,p orbitals [110].

Table 3.2 Comaprision of magnetization values

Process	Supercells configuration	Nearest neighbor configuration	Magnetic moment (μ)	Average moment per cell (μ)	Normalized magnetic moment (emu/gm)	Experimental value
Furnace annealing 20at% Si	4 cells with 13Fe 3Si	5 Fe atoms with 0 Si atoms as NN	11	22.064	153.341	155
		13 Fe atoms with 3 Si atoms as NN	12			
	1 cell with 12Fe and 4 Si	4 Fe atoms with 0 Si atoms as NN	8.8			
		12 Fe atoms with 4 Si atoms as NN	9.52			
Laser annealing 15at% Si	2 cells with 13Fe 3Si	5 Fe atoms with 0 Si atoms as NN	11	25.76	173.98	175
		13 Fe atoms with 3 Si atoms as NN	12			
	3 cell with 14Fe and 2 Si	6 Fe atoms with 0 Si atoms as NN	13.2			
		8 Fe atoms with 2 Si atoms as NN	14.4			

The magnetization value can be calculated based on number of Fe nearest neighbors [111][112].The magnetization (emu/gms) was estimated by calculating the magnetic moment of the DO_3 supercell for both furnace and laser annealed samples by considering the silicon content in the α-Fe(Si) phase obtained from the atom probe data (Figure 3.12,Figure 3.13Figure 3.14). As mentioned earlier, the Si concentration in furnace annealed sample is ~20 at% compared to ~15at% in laser annealed samples.

Fe_3Si phase has a DO_3 structure formed by 4 inter penetrating FCC sublattices with their origins at A(0,0,0) B(1/2,1/2,1/2), C(1/4,1/4,1/4) and D(3/4,3/4,3/4) [113]. As each FCC sublattice contains 4 atoms, there are 16 atoms in a supercell. Fe atoms occupy (A,C) sublattices with 4 Si atoms and 4 Fe atoms as NN (nearest neighbors) . In addition, Fe atoms also occupy (B) sublattice with 8 Fe atoms as NN. The D sublattice is occupied by Si atoms with 8 Fe atoms as NN. Fe atoms occupying the B sublattice have only Fe atoms as NN compared to 4 Si atoms as NN at (A,C) sublattice. Hence the magnetic moment of Fe atom is lower for (A,C) sublattice compared to B sublattice. When Si concentration decreases, Fe atoms substitute the Si atoms at the D sublattice. Hence, the magnetic moment of Fe atoms at (A,C) sublattice increases due to decrease in number of Si atoms as NN.

In the case of furnace annealed sample, 20 at% Si corresponds to an average of 3.2 Si atoms and 12.8 Fe atoms in a supercell. Similarly, for laser annealed sample, 15 at% Si corresponds to an average of 2.4 Si atoms and 13.6 Fe atoms per supercell. Hence, when 5 supercells are considered, they contain a total of 80 atoms. The furnace annealed sample has (16 Si , 64 Fe) whereas (12 Si, 68 Fe) atoms are present in the laser annealed sample. It has been reported that the magnetic moment of Fe decreases linearly with increase in number of Si atoms as NN [112]. The magnetic moment of Fe atoms as a function of Si NN has been calculated for each supercell configuration and an average magnetic moment per supercell was obtained. The obtained magnetic moment value was normalized w.r.t the average mass of the super cell to obtain saturation magnetization (Table 3.2). The calculated values are in close agreement with experimental observations (Table 3.2) indicating a low volume fraction of Fe_2B phase as only Fe(Si) phase was considered for theoretical calculation. This result is in agreement with the XRD analysis (Figure 3.8a).

In the present work, the processing conditions employed result in incomplete partitioning of silicon in the α-Fe phase due to rapid quenching during laser annealing. The α-Fe(Si) phase contains about 15 at% of silicon in the laser-annealed sample (Figure 3.12e Figure 3.13e), as indicated by the proximity histograms created from the atom probe reconstruction. Thus, due to less partitioning of silicon in laser-annealed sample, the magnetic moment of iron atoms is larger than conventional furnace-annealed samples, (Table 3.1). This can rationalize the increase in saturation magnetization observed in case of the laser-annealed sample. In addition, crystallization within the region between the consecutive laser tracks can be attributed to increasing temperature (Figure 3.11) close to the primary crystallization temperature (>780K)(Figure 3b), which also contributes to the increment of saturation magnetization (Figure 3.15).

The TEM micrographs clearly indicate that the precipitate density is quite high for laser-annealed samples (Figure 3.9) compared to furnace-annealed samples (Figure 3.10a,b). Significant crystallization is observed for the laser-annealed sample as indicated by the TEM diffraction patterns (Figure 3.9a and Figure 3.9c) although the processing time involved (1.2 ms) in laser annealing is many orders of magnitude shorter than conventional annealing (1hr). This is indicative of high nucleation rate for laser-annealing compared to furnace-annealing. The nucleation rate is governed by both thermodynamic and kinetic factors. During laser annealing, the temperature of annealing is considerably higher (>950K) than furnace annealing (823K), as evident from the thermal model (Figure 3.11). Furthermore, diffusion in amorphous materials is governed by the amount of available free volume. During furnace annealing, diffusion as well as annihilation of free volume (relaxation) takes place simultaneously. In contrast, laser annealing involves rapid heating rates and generation of localized thermal stresses that in turn increases the

amount of available free volume [18]. Thus, diffusion during laser annealing is enhanced compared to furnace annealing. In addition, the precipitate size in a microstructure depends on both nucleation rate as well as growth rate. During crystallization, the temperature (T_{Imax}) at which maximum nucleation rate occurs is observed at intermediate temperatures between T_m (melting temperature) and T_g (glass transition) as shown in the schematic (Figure 3.15b). This is attributed to lower thermodynamic driving force at very high temperatures and lower atomic mobility for lower temperatures [114] (Figure 3.15b). In contrast, the temperature at which the maximum growth rate (T_{Umax}) occurs is above maximum nucleation rate temperature (T_{Imax}) and just below melting temperature (T_m) (Figure 3.15b). Thus in laser annealing, the nucleation rate is much higher relative to the growth rate where as in furnace annealing, the nucleation rate is lower compared to growth rate as shown in the schematic (Figure 3.15b).

Both thermodynamic and kinetic factors favor faster diffusion for increased nucleation density. This increase in nucleation density results in the overlap of diffusion fields, resulting in soft impingement and as a consequence, finer crystallite size is achieved. In multi-pass laser annealing, considerable amount of re-heating takes place (Figure 3.11b) during subsequent laser passes, resulting in further growth and nucleation of new precipitates. This results in a wide size distribution of precipitates (~25-200nm) (Figure 3.9a-d) across the laser track with a mean precipitate size of 70nm. The precipitate size has a very strong influence on the magnetic properties like coercivity.

The coercivity is strongly influenced by the grain size (D), it has a D^6 relationship till the threshold size (ferromagnetic exchange length) and changes to 1/D for grain sizes greater than the ferromagnetic exchange length [6]. It is reported by many researchers that the precipitate size within the ferromagnetic exchange length (typically~30nm) has zero anisotropy based on the

random anisotropy model [115]. In the present case, larger precipitates (with size more than the ferromagnetic exchange length) possess significant magneto-crystalline anisotropy and hence contribute to the increase in coercivity. Furthermore, the presence of Fe_2B also contributes to coercivity due to higher magnetocrystalline anisotropy. In addition to coercivity, as mentioned earlier, the remnant magnetization (moment at B=0) remains the same (~65emu/gm) for both furnace and laser annealed samples, as indicated by the arrow in the hysteresis plot (Figure 3.15). It has been reported [116] that formation of Fe_2B is the major contributing factor for increase in remanence due to higher magnetocrystalline anisotropy value (430 kJ/m^3) [116] compared to Fe(Si)(8kJ/m^3). Thus, a small amount of Fe_2B results in substantial increment of remanent magnetization. Hence, it is speculated that the volume fraction of Fe_2B phase to be same in both furnace and laser annealing. Although remanent magnetization remains same, the Mr/Ms value for laser annealed is less(0.37) compared to furnace annealed(0.42) sample indicating better softmagnetic behavior for the former case. This is attributed to higher M_s (Table 3.2) value of laser annealed sample due to less Si partition as explained earlier.

Furthermore, it has been previously proven by Lorentz microscopy that the presence of iron borides acts as domain wall pinning centers, thereby strongly increasing coercivity [117]. During the formation of primary α-Fe(Si) crystallite dendrites in furnace annealed sample, boron is rejected into the amorphous matrix due to very low solubility of boron in the α-Fe(Si) phase [118]. This results in the enrichment of boron at the interface between the crystalline dendrite and amorphous matrix, resulting in the pinning of domain walls during magnetization. This explains the high coercivity for furnace-annealed samples. As annealing progresses, more boron gets enriched into the amorphous phase and finally results in the formation of Fe_2B. Furthermore, as mentioned earlier, furnace-annealed samples developed a dendritic microstructure whereas the

crystallites in the laser-annealed samples exhibited equiaxed morphology. This could be due to less partitioning of silicon, the partitioning has an influence on the interface stability. Thus, shape anisotropy factors may further increase the coercivity of the furnace-annealed samples. Hence, the increase in coercivity of furnace annealed samples can be explained based on Fe_2B formation, crystallite size and morphology and the increase in saturation magnetization for laser annealed samples can be attributed to less partitioning of Si.

Future work will be aimed at designing efficient heat transfer strategies during laser-annealing to obtain a finer grain size and retain a lower coercivity with substantial increases in the saturation magnetization. The present work demonstrates that laser processing can also be utilized to generate patterned nano-structures by direct laser irradiation without using masks. It is clearly indicative from the current work that shape of the laser beam plays a crucial role in altering the microstructure at a very fine scale (Figure 3.8b-d). This phenomenon can be extended to generate variety of patterned nano-structures by shaping the laser beam according to the requirement.

3.2.4 Magnetic Response of Multi-Pass Laser Processed Samples

The hysteresis curves (Figure 3.15) clearly indicate that the saturation magnetization of both furnace annealed as well as laser annealed samples increased compared to the as-received amorphous ribbon. In addition, a sharp increase in coercivity is observed for both laser and furnace annealing samples compared to as-received amorphous ribbon (Table 3.1). For laser-annealed sample, the coercivity is smaller (~42%) and the saturation magnetization is greater (by 12%) compared to that of furnace-annealed sample (Table 3.1). It is interesting to note that the remanent magnetization remains the same for both furnace and laser annealed samples (Figure

3.15).

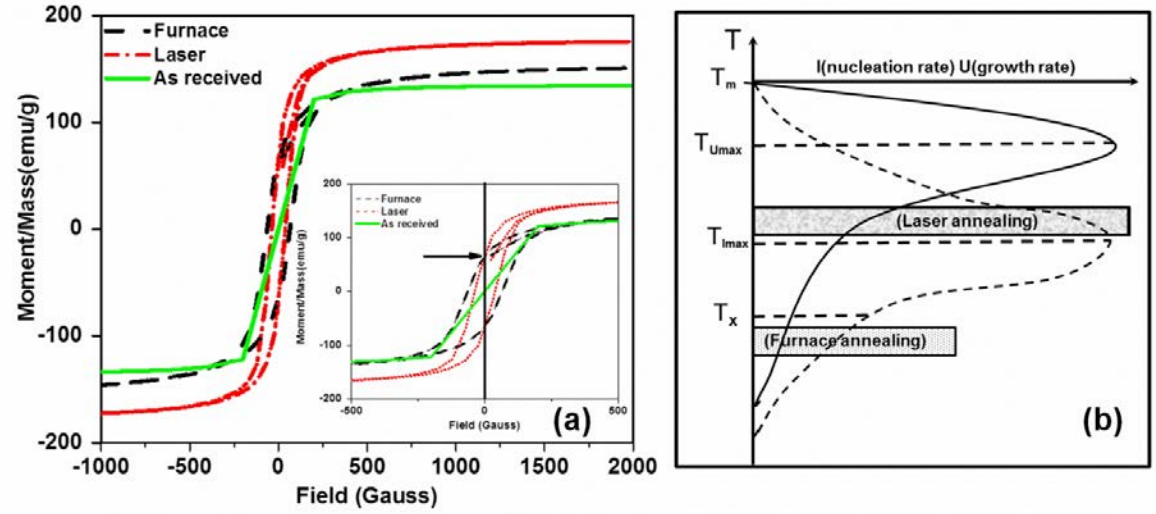

Figure 3.15 (a) Hysteresis curves ; (b) Schematic showing temperature dependence of nucleation and growth rate

3.2.5 Summary of Multi-Pass Laser Processing

In conclusion, laser annealing resulted in significant crystallization of amorphous ribbons and enhanced saturation magnetization compared to the as received ribbon as well as furnace-annealed samples. The XRD and TEM based analyses revealed the formation of the BCC α-Fe(Si) and Fe_2B phase in both laser and furnace annealed samples. Silicon partitioning into α-Fe phase for furnace annealed sample was higher (~20at %) compared to that in laser annealed samples~(15at%). The peak temperatures achieved during laser processing, both within the laser track as well as in between these tracks, exceeds the crystallization temperature, as predicted by our heat transfer model. The enhancement in magnetic properties in the case of the laser-annealed samples can be attributed to a finer grain or crystallite size as well as less silicon partitioning into the α-Fe(Si) crystallites.

3.3 Magnetic Field Effects during Crystallization by Laser Processing[3]

The present study focuses on the changes in the microstructure of an amorphous Fe-Si-B alloy after irradiating with a continuous wave laser beam of a Gaussian energy profile in the presence of external magnetic field. The microstructure evolution during laser processing was evaluated using site specific transmission electron microscopy (TEM) analysis along the laser track. The ability to site-specifically manipulate crystallization in an amorphous matrix via laser-based processing without and with application of an extermal magnetic field offers a tremendous potential for precise engineering of microstructure, thereby producing desired functional properties. This work not only demonstrates an advanced processing route to obtain nano-crystallization using laser processing, but also opens a new perspective to generate patterned magnetic structures at an ultra-fine scale.

3.3.1 Phase and Microstructural Evolution

The crystallization temperatures of the present amorphous system were evaluated using DSC analysis. Two exothermic peaks can be clearly seen in the DSC graph at 780K and 820 K respectively indicating two crystallization events (Figure 3.7). The equilibrium phases corresponding to the two exothermic peaks are reported to be α-Fe(Si) and Fe_2B respectively [103,104]. The schematic of microstructure evolution and high resolution TEM microstructures within the laser processed sample on a magnetic substrate is presented in a schematic. (Figure 3.16a). The boundaries of central and edge regions were defined based on distribution of temperature, stresses, and microstructure reported in previous work [17,18]. Although there was a continuous variation of these parameters within these regions, the associated distinct changes were realized only across the boundary between central and edge regions. This can be attributed

[3] Parts of this section either in part or in full, are taken from Shravana Katakam, and Narendra B. Dahotre submitted to Applied Physics A for prospective publication.

to subtle variation in temperature evolution within these individual regions due to the broad Gaussian beam with steep gradient towards the wing section of the beam. The analysis of selected area diffraction (SAD) patterns obtained from the center region indicate the formation of α-Fe(Si) phase along with Fe_2B phase (Figure 3.16b) with a random texture. However, only α-Fe(Si) phase was observed within the edge region (Figure 3.16c) indicating development of lower temperature in this region compared to center region of the laser track. Furthermore, aclear indication of crystallographic texture can be observed from the arcs in the diffraction pattern of the sample analyzed from the edge region of the laser track (Figure 3.16c). The average grain size was estimated by taking an average of manually measured grain sizes of several grains from the TEM micrographs using the image J^{TM} analysis. It is observed that the average grain size in the center region (40 nm ± 11) is more than 5 times larger than the average grain size from the edge region (7 nm ± 1.5) of the laser track.

On the contrary, the TEM analyses of the sample processed without backing of a magnetic substrate indicated the formation of α-Fe(Si) and Fe_2B within both center and edge regions of the laser track (Figure 3.17).This has been attributed to poor heat transfer away from the laser irradiated region and hence enhanced preheating effects occurred during multi-pass laser processing without a magnetic substrate as explained in our previous report [119]. Additionally, significant grain growth occurred both within the center region (90 nm± 50) and the edge region (70 nm ± 40) of the laser track for the sample processed without a magnetic substrate. (Figure 3.17a and Figure 3.17b respectively). The grain size variation is summarized in Table 3.3 and the rationale behind the microstructural evolution (Figure 3.16 Figure 3.17) for the samples laser processed with or without the application of magnetic field is further explained in the following section.

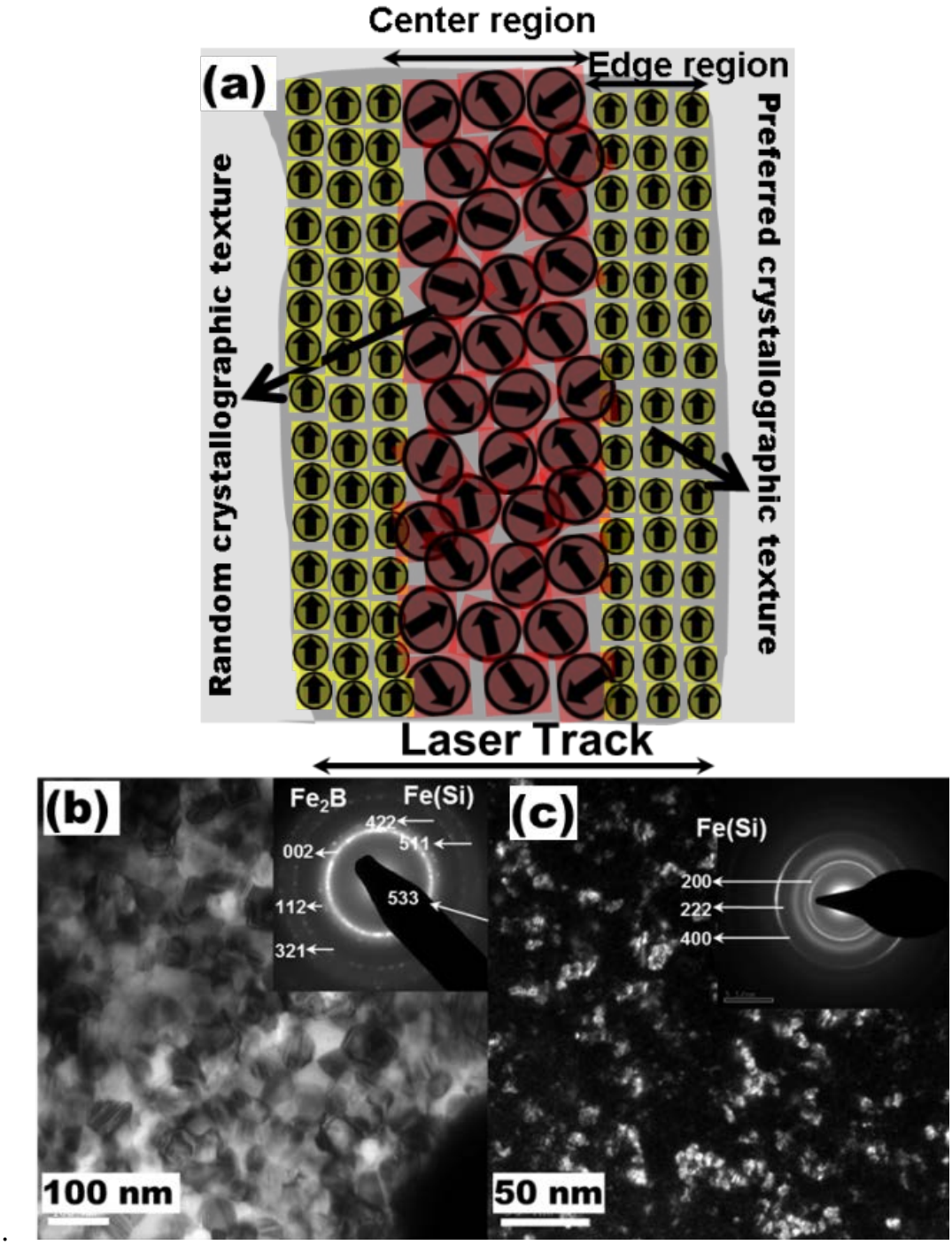

Figure 3.16 Microstructure of the laser processed region for sample processed on a magnetic substrate; (a) schematic of microstructure evolution; (b) bright field TEM image from center; (c) dark field TEM image from edge region

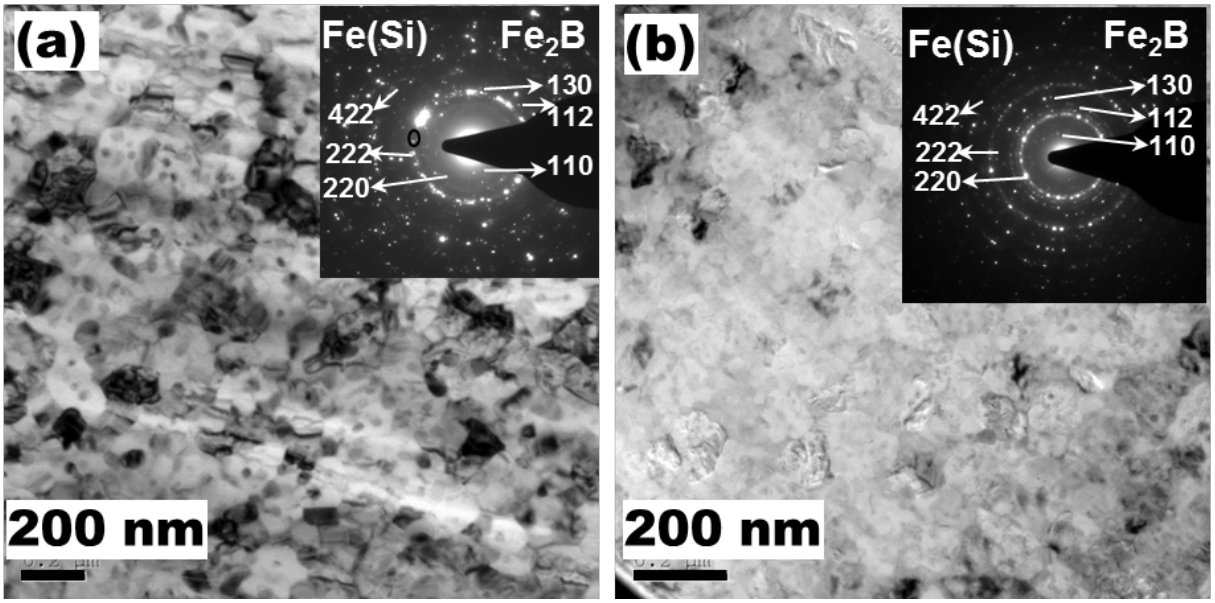

Figure 3.17 Bright field TEM micrographs within the laser processed track of the sample without a magnetic substrate; (a) center region; (b) edge region

3.3.2 Temperature Evolution based on Diffusion based Calculations

In general, the evolution of microstructure depends on the thermal histories experienced by the material. Thus, the temperatures attained within the edge and center regions of the laser track during laser processing are predicted by diffusion based calculations.

Table 3.3 Measured and computed physical parameters associated with laser processed samples with and without magnetic substrate

	Diffusivity (m^2s^{-1})		Temperature attained (K)		Average grain size (nm)	
	Center	Edge	Center	Edge	Center	Edge
Laser annealing without magnetic substrate	$6.75x10^{-12}$	$4.083\ x10^{-12}$	1548	500	90±50	70±40
Laser annealing with magnetic substrate	$1.875\ x10^{-13}$	$4.083\ x10^{-14}$	1261	390	40±11	7±1.5

As mentioned earlier, if the diffusion process is based on the random walk phenomenon and the diffusion length d traveled by the atom can be expressed in terms of the diffusivity and time taken for diffusion as indicated Equation 3.7, in this case, time taken for diffusion is assumed to be the residence time of the laser beam. The residence time is defined as the time required by the laser beam to travel one beam diameter distance. Assuming that development of nano crystal size (Figure 3.16 Figure 3.17) is predominantly based on grain growth without coarsening due to rapid laser processing (laser beam residence time of 1.2 milliseconds), diffusivity is calculated within the edge and center regions of the laser track (Table 3.3) based on the random walk phenomena. Further, estimation of diffusivity considered the diffusion distance d traveled during the laser beam residence time as equal to the radius of average nano particle size measured from TEM micrographs (Figure 3.16 Figure 3.17). Thus, the temperatures within the center and edge regions of the laser track are predicted using Equation 3.7 (Table 3.3).

$$D = D_0 \exp\left(\frac{-E_a}{k_B T}\right) \qquad \text{Equation 3.8}$$

where D_0 (4.6×10^{-5}) is the pre-exponential factor[102], k_B is Boltzmann constant (4.617×10^{-5}), T is the temperature and E_a is the activation energy for diffusion jump (2.1 eV for the center region [102] and 0.7 eV for the edge region [18]). The activation energy for the center region of the laser track is assumed to be equal to activation energy for self-diffusion of Fe atom estimated by calorimetric studies [102] and the activation energy for the edge region of the laser track was estimated in the earlier work in reference [18]. It was observed that the edge region of the laser track has substantially lower activation energy due to generation of thermal stresses [18]. The large difference between the temperatures within the edge and center regions of the laser track (Table 3.3) can be attributed to the Gaussian nature of the laser beam intensity. The laser beam

intensity is maximum in the center region and drops down exponentially towards the edge region of the laser track.

It has been reported in previous studies that crystallization occurs at lower temperatures within the edge region of the laser track than reported crystallization temperatures in these amorphous material systems. The reduction in crystallization temperature can be due to generation of thermal stresses during laser processing. It has been demonstrated in our previous works that laser annealing is a complex crystallization process which has contributions from both thermal [17] and stress factors [18]. Especially, the generation of high magnitude stresses results in substantial decrease of activation energy for diffusion of atomic species within the edge region of the laser track. The magnitude of compressive stresses within the edge region near the interface between the laser processed and unprocessed regions even exceeded the yield strength resulting in generation of shear bands leading to rapid crystallization well below the crystallization temperature [18]. Furthermore, a clear reduction in temperature values both within the center and edge of the laser track are realized for the sample processed on a magnetic substrate (Table 3.3). This can be attributed to efficient heat transfer away due to increase in contact area between the amorphous ribbon and the magnetic substrate. Thus the heat transfer will have an influence on the evolution of microstructure that is further discussed in the following part of the paper. In addition to temperature variation, a significant variation in diffusivity of the atoms is also observed for the sample processed on a magnetic substrate (Table 3.3).

3.3.3 Magnetic Field Effects on Nucleation and Growth

The microstructure evolution during crystallization can be explained by nucleation and growth phenomena. In general, both nucleation and growth rates are lower at higher

temperatures, as the thermodynamic driving force decreases for both nucleation and growth at low undercooling. In contrast, at low temperatures and associated higher undercooling, although the thermodynamic driving force increases, the atomic diffusion becomes sluggish leading to lower nucleation and growth rates. Thus, maxima in nucleation and growth rates prevail at intermediate temperatures as proposed by various researchers [114,120,121]. Based on the above mentioned arguments, typical nature of nucleation and growth rates during crystallization are schematically illustrated in Figure 4 [114,120,121]. Furthermore, the maximum nucleation rate (I_{max}) occurs with higher undercooling ($T_{Imax} < T_{Umax}$) compared to growth rate (U_{max}) as a large driving force is required to nucleate a crystalline phase by overcoming the amorphous/crystalline interfacial energy (Figure 3.15).

Earlier reports clearly indicate that conventional furnace annealing at low temperature experiences a very slow growth rate requiring an excessively long duration to obtain significant amount of crystallization whereas, annealing at higher temperature results in higher growth rate leading to rapid growth of the grains [84,85,122,123]. During crystallization, steady state nucleation rate is given by $I_{st} = I_0 * e^{-\left(\frac{Q}{RT}\right)} * e^{-\left(\frac{\Delta G_c}{RT}\right)}$ [124] where I_0 is the pre-exponential coefficient, Q is the activation energy and ΔG_c is the free energy change for the formation of critical nucleus. Thus, it is evident from the above expression that the change in free energy from amorphous to crystalline phase has an effect on the nucleation rate. Additionally, the free energy change during crystallization is influenced by the external magnetic field as described below.

In the presence of a magnetic field, the change in free energy is given by $\Delta G_c = \frac{16\pi\sigma^3}{3\left[\left|\Delta G_v\right| + \frac{1}{2}H^2(\mu_2 - \mu_1)\right]^2}$ [125] where σ is the interfacial energy between the amorphous matrix and crystalline phase, ΔG_v is the volume free energy change between the

crystalline and amorphous phase, H is the external magnetic field, and μ_2 and μ_1 are the permeabilities of the resultant crystalline phase and the residual amorphous phase [125]. It was reported that partial devitrification of the same alloy increased the permeability by 3 times attributed to precipitation of α-Fe(Si) [126]. This indicates a higher permeability of crystalline α-Fe(Si) compared to amorphous phase. Thus, nucleation of crystalline phase is promoted for the present alloy system in the presence of magnetic field. Based on the above mentioned phenomena, the microstructure evolution in the sample laser processed on a magnetic substrate is compared with the sample laser processed without magnetic substrate.

It has already been reported in our earlier report that laser processing without a magnetic substrate results in finer grain size (70 nm within edge region and 90 nm in center region) compared to furnace annealing (100 nm) due to higher nucleation rate for the former process [119]. In the present report, finer grain sizes (40 nm within center region and 15 nm within edge region) are observed in case of sample processed on a magnetic substrate using the same laser processing conditions as those used for the sample without a magnetic substrate. This is clearly indicative of a higher nucleation rate due to the magnetic field effects. The sharp diffraction rings for both the samples laser processed, with and without magnetic substrate indicate significant crystallization after laser processing (Figure 3.16 and Figure 3.17). Thus, the finer grain size for the sample processed on a magnetic substrate is likely due to increase in nucleation rate. In addition to grain refinement due to enhanced nucleation rate, application of magnetic field also influenced the diffusion due to additional force by the magnetic field on Fe atoms by virtue of their magnetic moment [127,128,129,130] and subsequently the grain morphology.

The effects of magnetic field on the diffusion processes have been reported by many researchers including the application of magnetic field during annealing to obtain uniform grain size

distribution by grain boundary engineering [130,131]. The magnetic field restricts the abnormal grain growth of nano-crystals which usually occurs during conventional heat treatments performed without magnetic field. The abnormal grain growth in conventional annealing is due to the instability of the interphase associated with the segregation of solute elements at high energy grain boundaries [127,128]. However, application of magnetic field likely to reduce the diffusion of alloying elements to these high energy sites avoiding the instability of the interface. Therefore, in the present case, it is speculated that the magnetic field reduces the segregation of Si to high energy grain boundaries of Fe resulting in equiaxed microstructure with narrow grain size distribution. Furthermore, the magnetic field also has an effect on the crystallographic texture for the sample processed on a magnetic substrate.

3.3.4 Induced Crystallographic Texture by Magnetic Field Processing

It can be noticed that the temperature within the center region (1261K) of the laser track for the sample laser processed on a magnetic substrate is above Curie point (668K) of the present alloy resulting in its crystallization in the paramagnetic state. In contrast, although the crystallization temperatures (>780K) predicted by calorimetric analysis (Figure 3.7) are greater than the Curie temperature, the computed temperature within the edge region of the laser track (400K) is well below Curie point indicating that the crystallization had occurred in the ferromagnetic regime. The reduction in crystallization temperature within the edge region during laser processing is likely due to the generation of thermal stresses as discussed in the earlier sections.

It has been reported [132,133] that annealing of ferromagnetic materials in the presence of magnetic field is likely to result in a crystallographic texture due to the magneto-crystalline

anisotropy of the material. The torque experienced due to magnetocrystalline anisotropy of the ferromagnetic phase is likely to be more than the shape anisotropy and the thermal disordering effects leading to a crystallographic texture [134,135,136]. This explains the evolution of crystallographic texture evident from the arcs in the SAD (selected area diffraction pattern) obtained for the sample from the edge region of the laser track (Figure 3.16c). In contrast, as mentioned earlier, the temperature attained (1261K) within the center region of the laser track for the sample processed on a magnetic substrate is above Curie temperature of both α-Fe(Si) (800K) [137] and Fe_2B (1015K) [138] phases. Hence, the magnetic torque experienced by the phases in the paramagnetic state is likely to be less effective in overcoming the thermal and shape anisotropies resulting in random texture evident from the sharp circular ring pattern for the sample from the center region of the laser track.

Thus, in the present work, it is demonstrated that a patterned magnetic structure with different magnetic properties within the edge and center regions of the laser track can be generated using laser processing. Furthermore, the new processing route can be further explored to obtain nanocrystalline anisotropic hard magnetic materials with high energy product $(BH)_{max}$ with many potential applications.

3.3.5 *Magnetic Property Comparison*

As mentioned earlier, low coercivity values are the characteristic of good soft magnetic property. The hysteresis curves indicate a sharp decrease in coercivity value for the sample processed on a magnetic substrate compared to both laser annealed without a magnetic substrate as well as furnace annealed sample. This is likely due to extremely refined microstructure for the sample processed on magnetic substrate. As mentioned earlier, the coercivity value is a strong function of grain size and decreases as D^6 where D is the grain size. Furthermore, in addition to

decrease in coercivity, a significant increase in saturation magnetization for the sample processed on a magnetic substrate is observed compared to furnace annealed and as received sample.

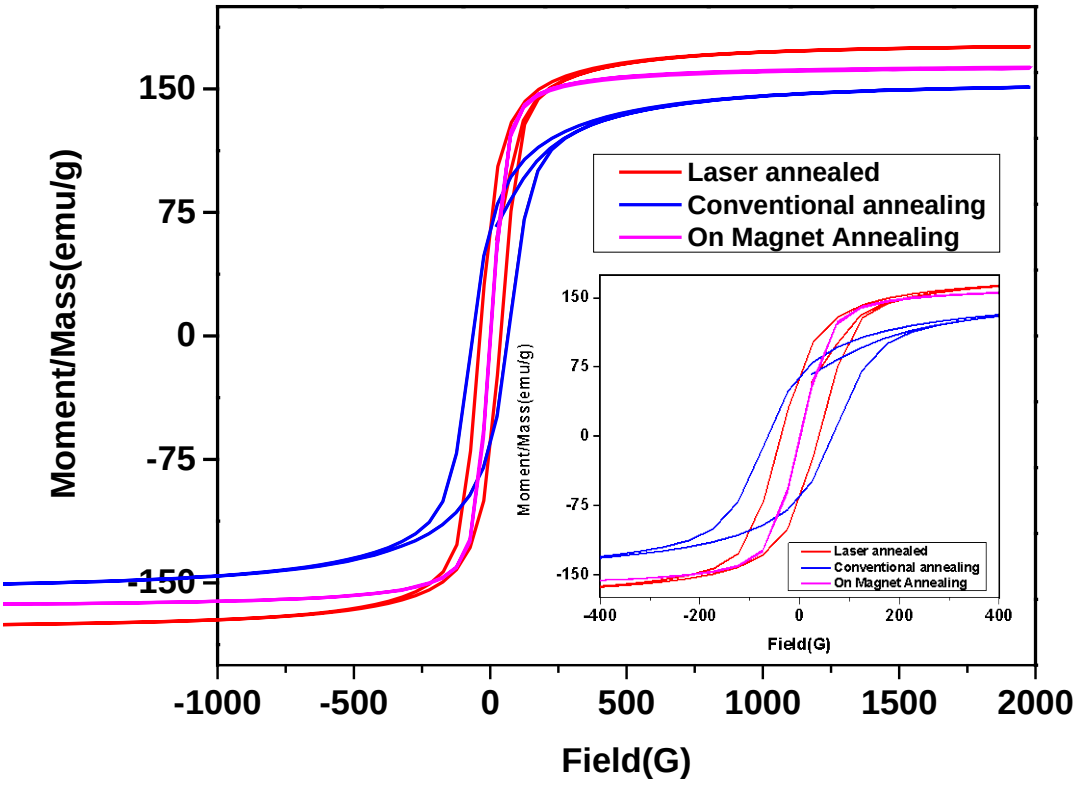

Figure 3.18 Comparison of magnetization curves

This is likely due to the high saturation magnetization of the crystalline phase compared to amorphous phase. As mentioned in the previous section, the partitioning of Si into the BCC Fe phase also has an effect on the saturation magnetization. The influence of Si concentration on the saturation magnetization will be further explored using atom probe tomography.

3.3.6 Summary of Magnetic Field Processing

The effects of magnetic field on laser assisted crystallization of amorphous Fe-Si-B were identified. Site specific microstructural characterization revealed a significant refinement in grain size in the sample processed on a magnetic substrate compared to sample processed without a

magnetic field. The TEM diffraction analysis of the laser processed sample on a magnetic substrate revealed no significant crystallographic texture within the center region of the laser track where as a crystallographic texture was developed within the edge region. Diffusion based computations revealed a significant decrease in temperature of phase transformation within the edge region compared to the center region of the laser track. The crystallographic texture within the edge region of the laser track is attributed to reduction in crystallization temperature below Curie temperature due to generation of thermal stresses during laser processing

CHAPTER 4

LASER SYNTHESIS OF AMORPHOUS FE-CR-MO-Y-C-B ON STEEL SUBSTRATE

4.1 Characterization of Coating[4]

4.1.1 Phase Evolution

The x-ray diffraction (XRD) profile of the precursor $Fe_{48}Cr_{15}Mo_{14}Y_2C_{15}B_6$ powder (Figure 4.1**)** exhibited a single diffuse and broad peak confirming its amorphous nature.

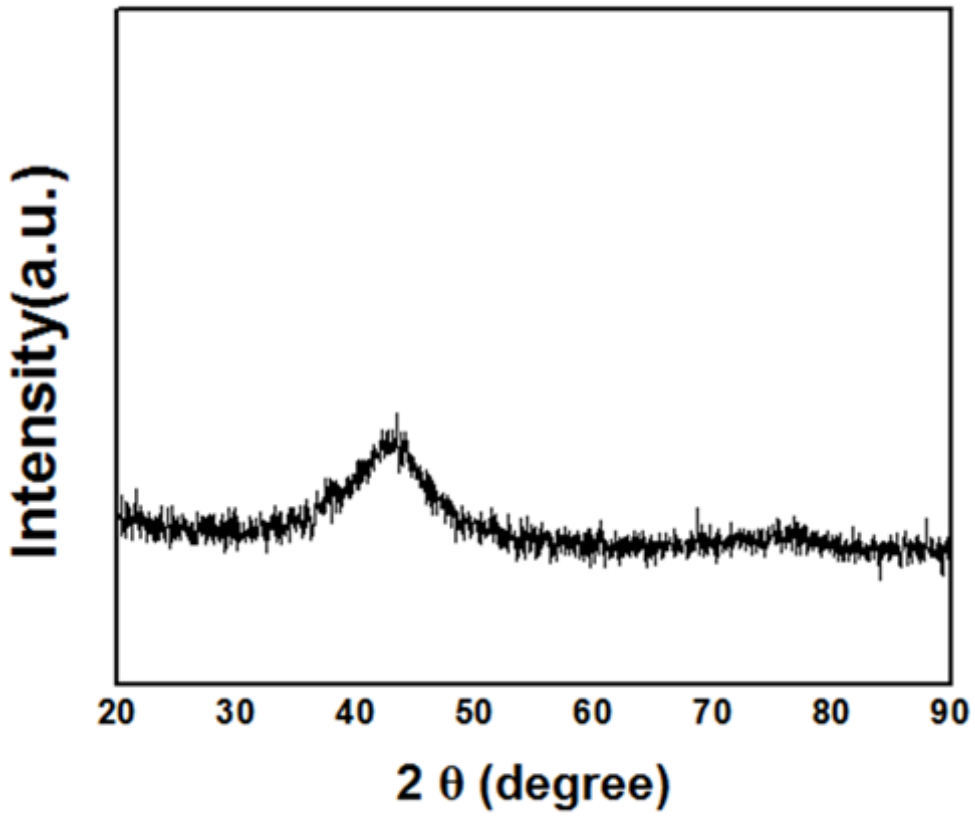

Figure 4.1 X-Ray diffraction pattern of $Fe_{48}Cr_{15}Mo_{14}Y_2C_{15}B_6$ coating precursor powder

The powder has a distinct glass transition at 848 K followed by double exothermic crystallization peaks [139]. These results confirm that the precursor powder used in the present study is suitable

[4] Parts of this section have been previously published, either in part or in full, from Shravana Katakam, Jun Y. Hwang, Sameer Paital, Narendra B. Dahotre: Metallurgical and Materials Transactions A (2012), Vol-43, pp 4957-496

for the proposed objective of developing an amorphous coating on steel substrate by laser surface coating. The XRD results from a series of layers, each deposited by employing a different laser energy density and are shown in Figure 4.2.

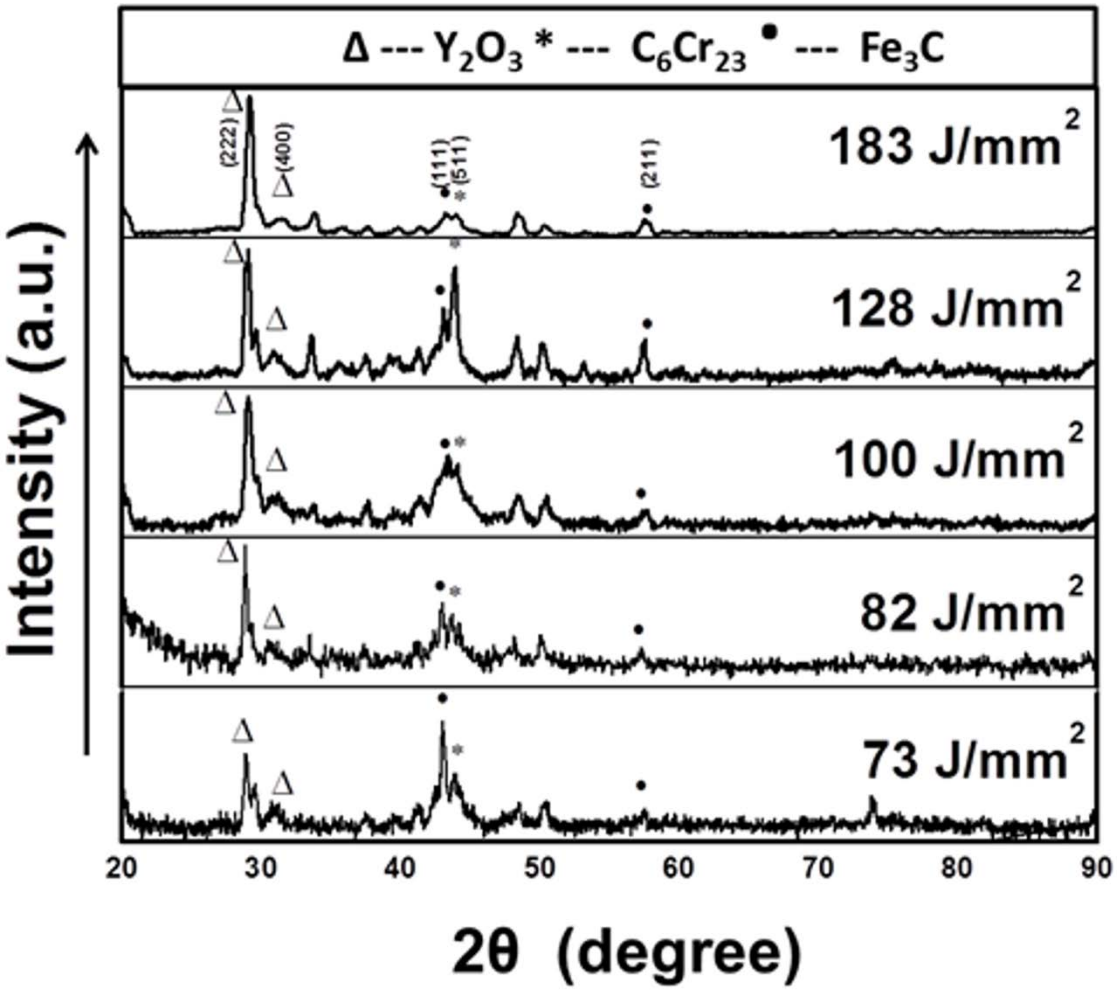

Figure 4.2 X-Ray diffraction patterns of samples processed with varying laser energy density

The XRD spectra of the laser-processed samples (Figure 4.2) exhibit a diffuse peak in the same 2θ range (40^o-50^o) as the amorphous powder (Figure 4.1) indicating the presence of the amorphous phase in the as-deposited coatings. Additionally, the spectra also exhibit sharp peaks that can be attributed to the formation of crystalline phases. These crystalline peaks correspond to various oxide and carbide phases that usually form in the absence of yttrium [54] which in the

present case has been consumed in formation of yttrium oxide (Figure 4.2). Therefore, based on the XRD results the laser-processed coatings exhibit both amorphous and crystalline phases. This composite nature (amorphous + crystalline) of the coating is further evident from the TEM bright field image (Figure 4.3a) of the sample processed with laser energy density 100J/mm^2.

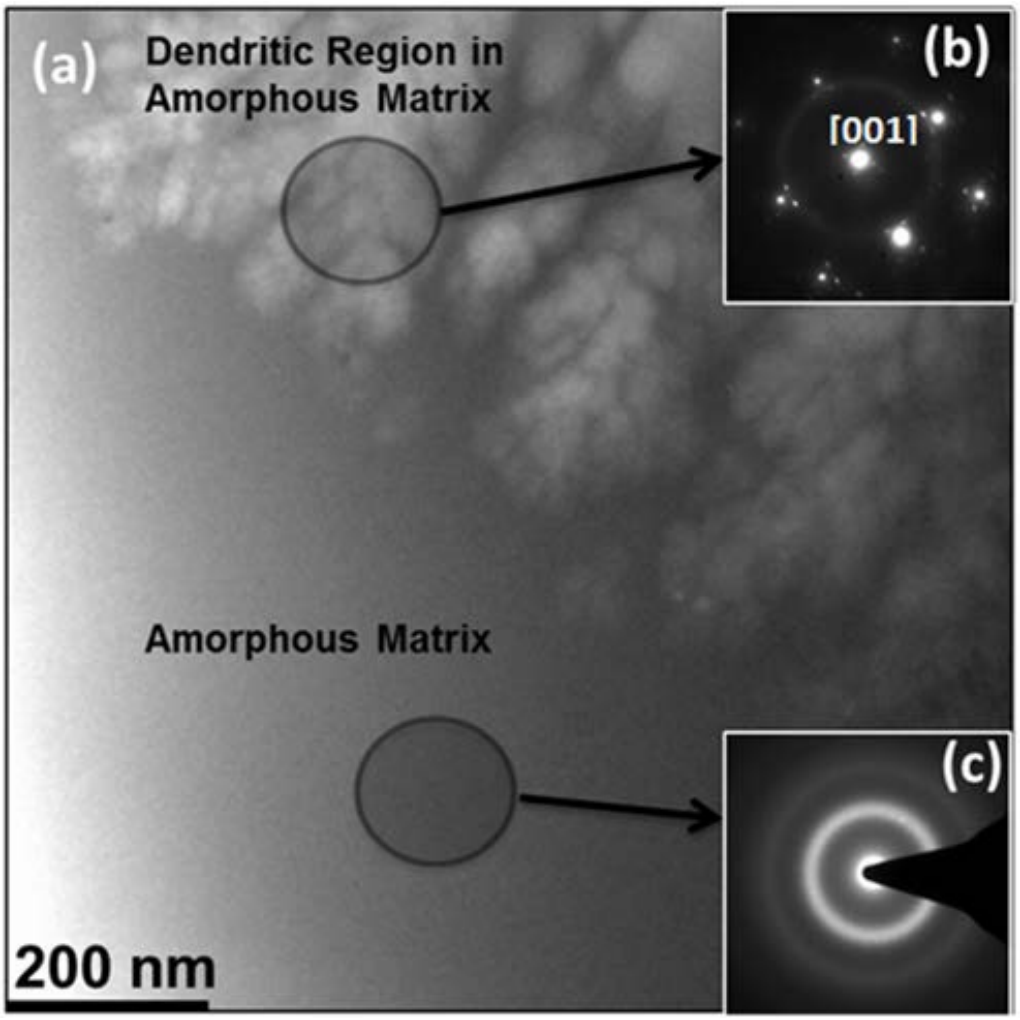

Figure 4.3 (a)TEM bright field image of the coating in the sample laser processed with 100J/mm^2 energy density; (b) and (c) are diffraction patterns from the highlighted regions

The inset (Figure 4.3b) corresponds to SAD pattern taken from the dendritic region which can consistently indexed as the <0 0 1> zone axis of a face centered cubic (fcc) austenitephase. It can be observed that the diffraction pattern also contains a diffuse ring pattern apart from the spots which is a clear indication of composite microstructure consisting of both crystalline and

amorphous phases. The TEM bright field image of the featureless region corresponds to the amorphous phase, further confirmed by the diffraction pattern, comprising broad and diffuse rings, shown in the inset, Figure 4.3c.

A detailed view of the diffraction spectra from the laser processed samples, in the range of 2θ (41^0-47^0),corresponding to the diffuse (broad) peak observed in case of the precursor powder (see Figure 4.1) is shown in Figure 4.4.

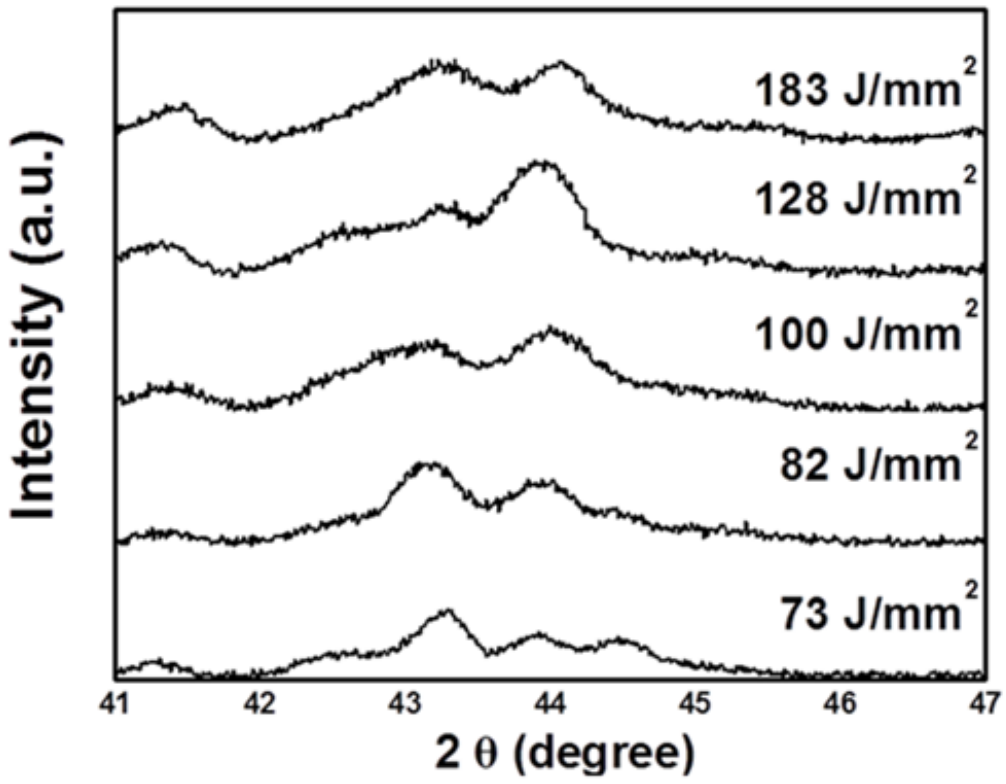

Figure 4.4 X-Ray Diffraction pattern in the 2θ range of 41^0-47^0 of the samples laser processed with varying energy density

Figure 4.4 clearly shows that, in the laser-deposited coatings, this broad diffuse peak is splitting into multiple sharper peaks indicating a clear phase separation within the amorphous phase. On the basis of thermodynamics, it can be argued that in a multi component system the transformation from liquid to solid usually occurs by phase separation. Hence, it can be said that

increase in phase separation tendency is an indication of increase in crystallization tendency. In the present case, the phase separation tendency increases with decreasing laser energy density which can be attributed to the diffusion kinetics and slower cooling rates experienced by the coating in case of the lower energy density. The XRD spectra (Figure 4.2) indicate the formation of various crystalline phases and also amorphous phase separation (Figure 4.4) that require substantial solute redistribution resulting in evolution of different morphologies in the microstructure. The evolution of microstructure and the distribution of different elements are further characterized by microstructure analysis described in the following section.

4.1.2 Microstructure Evolution

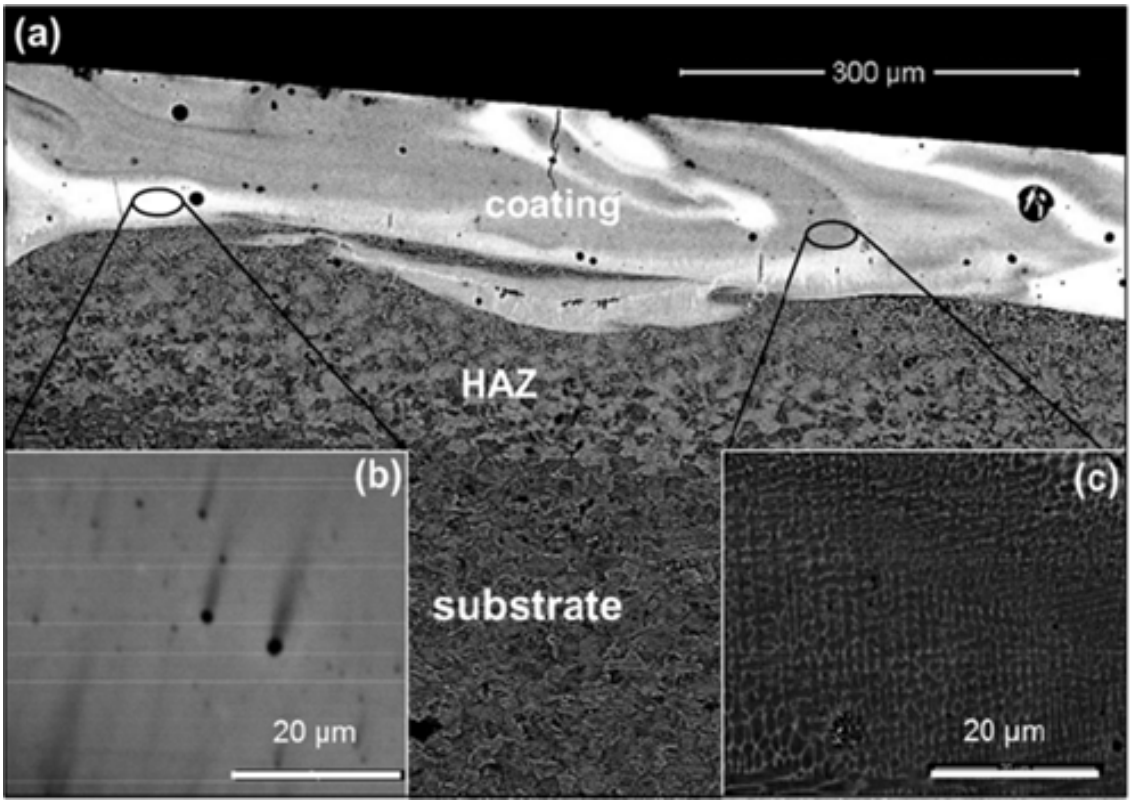

Figure 4.5 SEM back scattered image of the sample laser processed with 100J/mm^2 energy density

SEM and TEM characterizations have been conducted to study the evolution of microstructure and a correlation between the phase evolution and thermal conditions developed

during processing. The redistribution of solute elements is evident from the backscattered SEM micrograph (Figure 4.5a) indicating a distinct contrast between the phases. At higher magnification, different morphologies are observed for bright and dark regions of the micrograph.

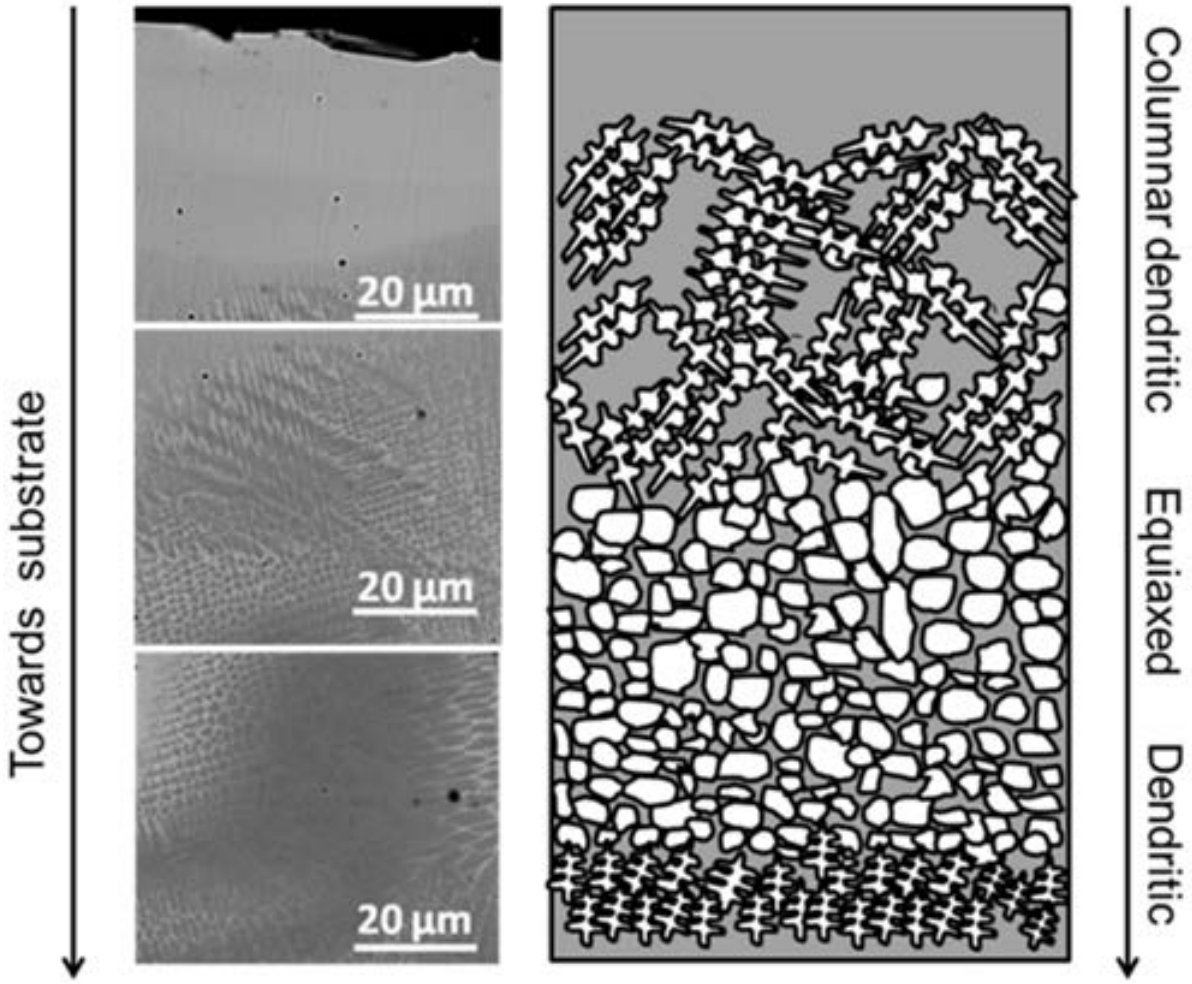

Figure 4.6 SEM secondary electron micrographs of coating in the sample laser processed with energy density 100J/mm^2 and schematic of corresponding region showing evolution of various microstructural features

The white region is featureless due to the formation of an amorphous phase (Figure 4.5b) whereas the dark region has a dendritic/cellular morphology (Figure 4.5c). There is always a competition between the formation of crystalline phase and amorphous phase and glass will form only when the glass transition isotherm T_g is above the growth temperature of all possible

crystalline phases [140][34]. The growth temperature as well as the T_g depends on the composition [141][35]. Furthermore, from the back scattered SEM image (Figure 4.5), a clear composition variation can be observed between the dendritic regions and the amorphous regions indicating the formation of amorphous phase due to local composition variation. The secondary electron images in the coating region indicate development of different microstructures (Figure 4.6) starting from the substrate/coating interface to the surface. The interface has a dendritic morphology and gradually transforms from equiaxed to cellular-dendritic structure due to change in thermal conditions as depicted in the accompanying schematic of microstructural view and further described in the later part of the paper. A detailed TEM characterization was conducted to confirm the retention of the amorphous phase and formation of the crystalline phase, and also to conduct analysis of the interface between amorphous and crystalline phases within the coating.

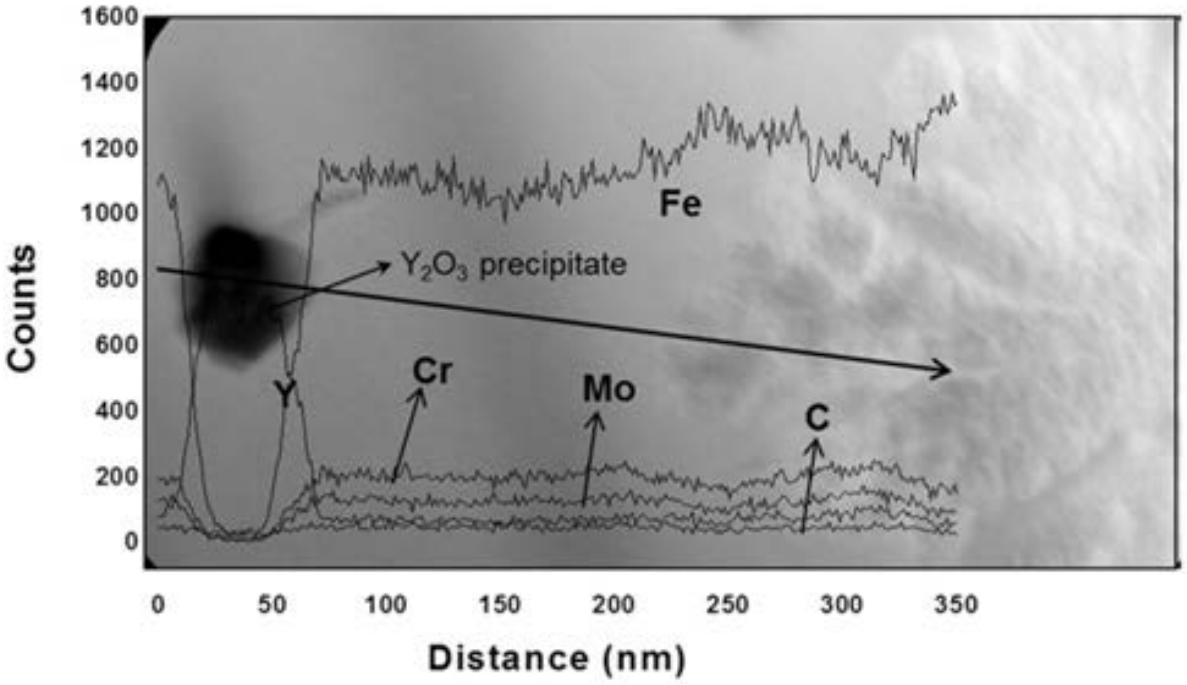

Figure 4.7 TEM bright field micrograph with EDS line profile mapping along the line within the coated region

The interface between the amorphous and crystalline phase consists of a very fine dendritic microstructure as seen from the high magnification TEM bright field images (Figure 4.3 Figure 4.7).

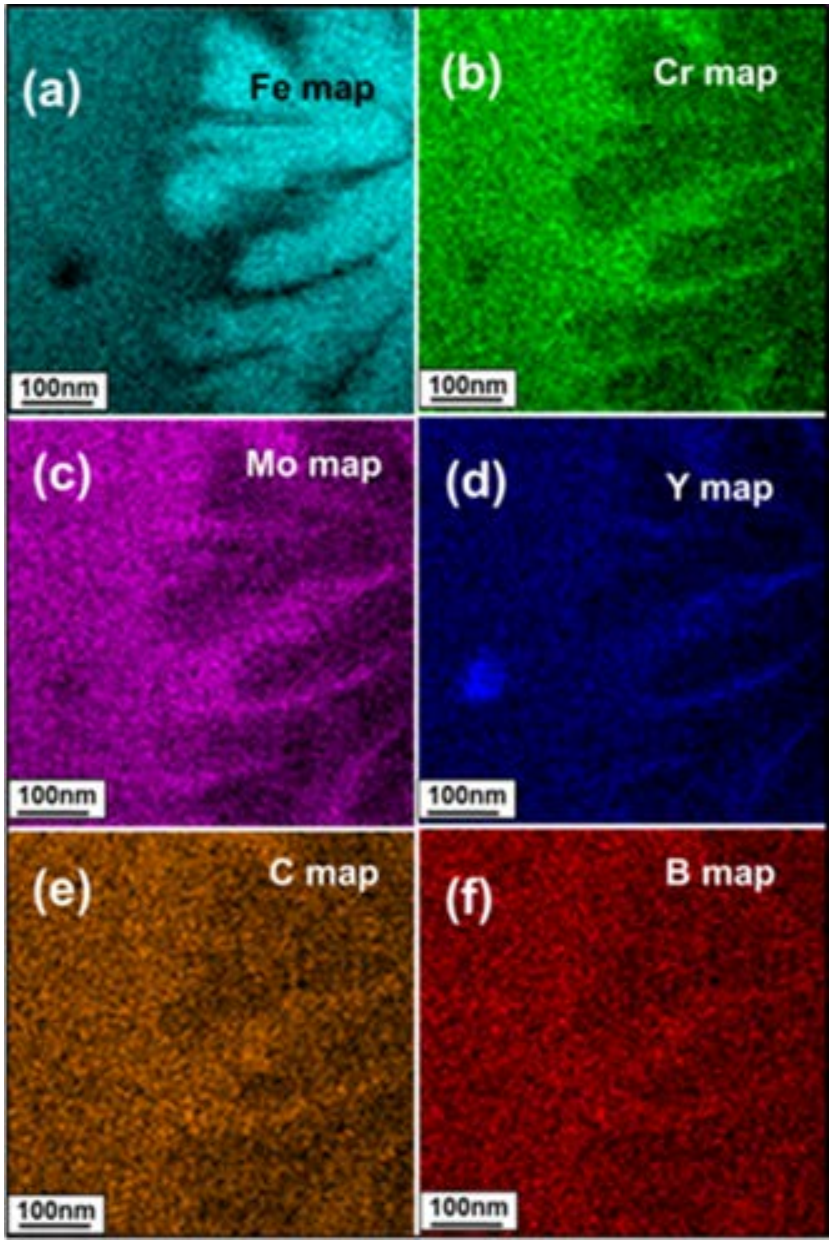

Figure 4.8 High resolution STEM EDS maps of coated region for elements (a)Fe; (b) Cr; (c) Mo; (d) Y; (e) C; (f) B

The EDS line profiles of the different solute elements, across the amorphous/crystal interface have also been plotted in Figure 4.7. From these line profiles, it can be observed that while the concentration of the Fe increases, that of all other solute elements decreases across this interface

when progressing from the amorphous to the crystalline side. The trend appears to reverse within the dendritic crystalline region. EDS maps of this region, for different solute elements, have been recorded in Figure 4.8**.** These maps clearly show that the dendritic phase has a higher amount of Fe compared to the amorphous phase. Furthermore, it can also be inferred from the EDS maps that the solute yttrium appears to be evenly dispersed in the amorphous phase (Figure 4.8d) and depleted in the crystalline phase. The evolution of morphology and distribution of elements can be attributed to change in thermal conditions. As in the laser processing it is difficult to know the thermal histories by in-situ experiments, a computational route was adopted. The evolution of thermal histories is discussed in the following section.

4.2 Thermal Analysis

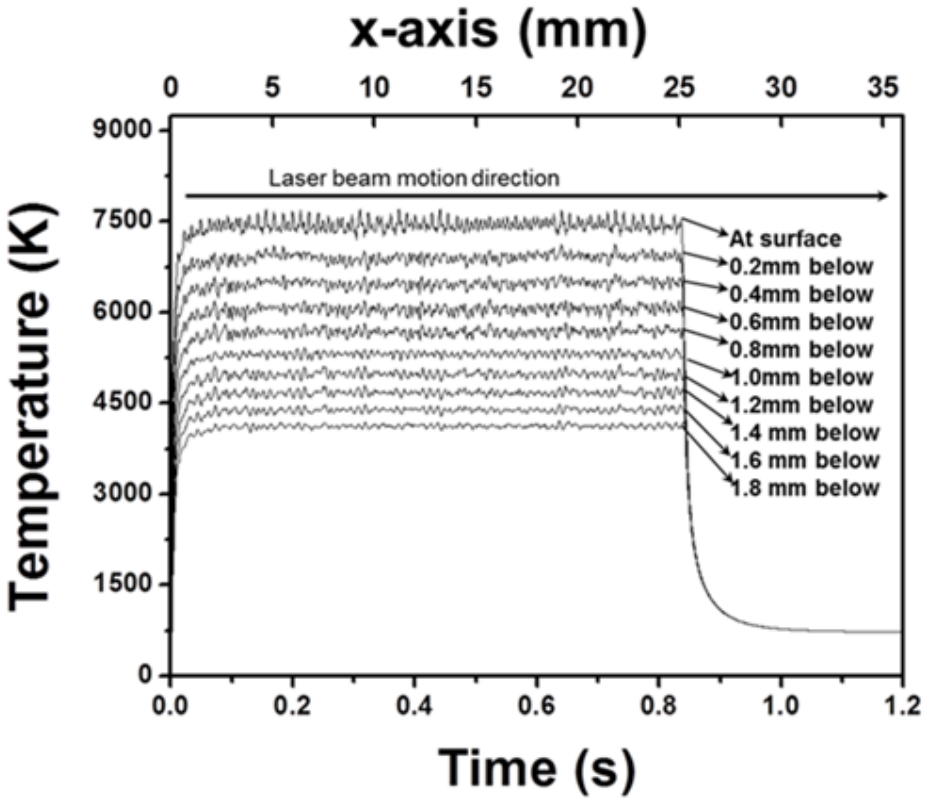

Figure 4.9 Thermal profiles generated by the virtual thermal probes placed along and at different depths, the peak temperature decreases with increase in depth

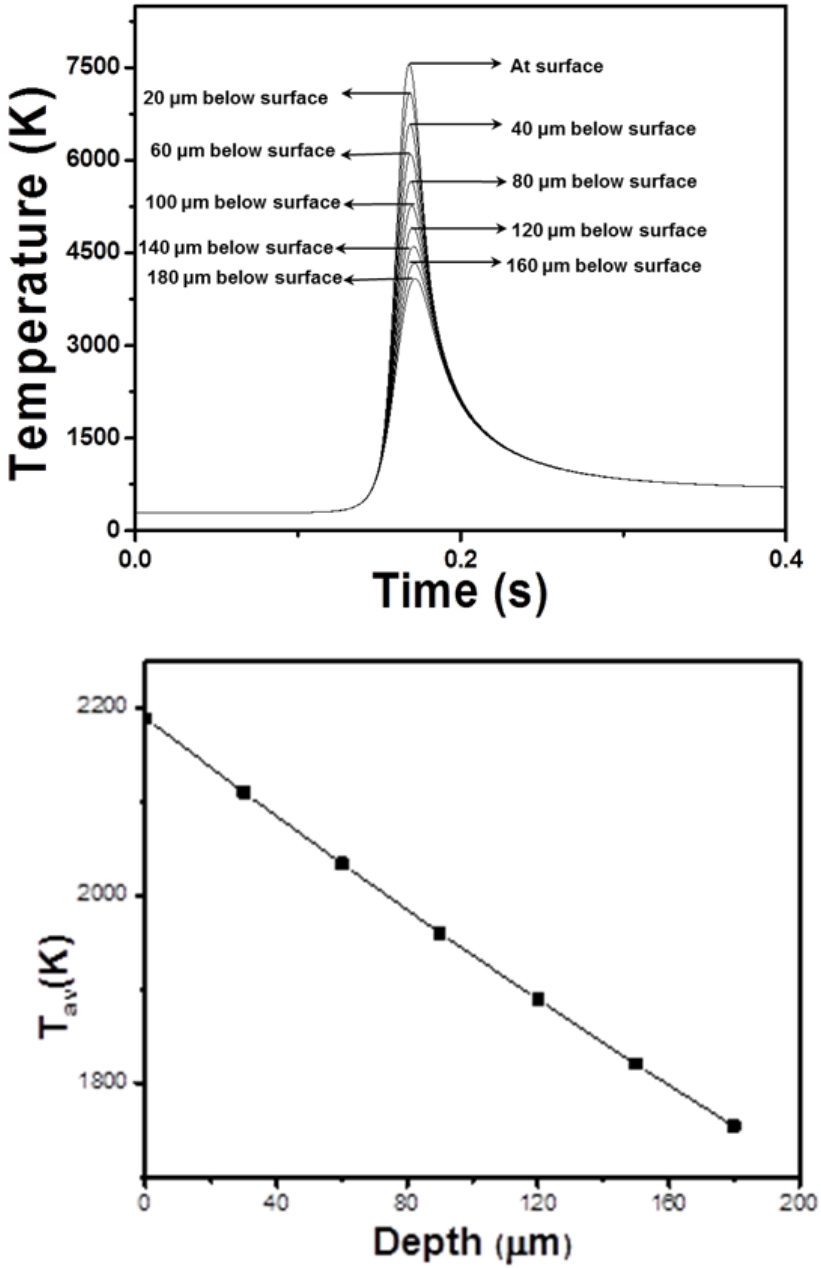

Figure 4.10 Typical thermal depth profiles generated by the virtual thermal probes taken from an arbitrary point on the track (a) instantaneous temperature; (b) average temperature as variation of depth

In order to obtain the cooling rate, which is a critical parameter for the formation of amorphous phase, and various microstructural features, thermal profiles are computationally generated at different locations on surface (x-direction) and in depth (z-direction) of the coating and presented

in Figure 4.9. The exaggerated instantaneous and average thermal profiles generated across the depth at one representative location of the coating are presented in (Figure 4.10). The instantaneous temperatures in laser processing (Figure 4.10a) are high, however, these temperatures are highly localized and are confined within very small volume thereby generating extremely high cooling rates and lower average temperatures (Figure 4.10b).

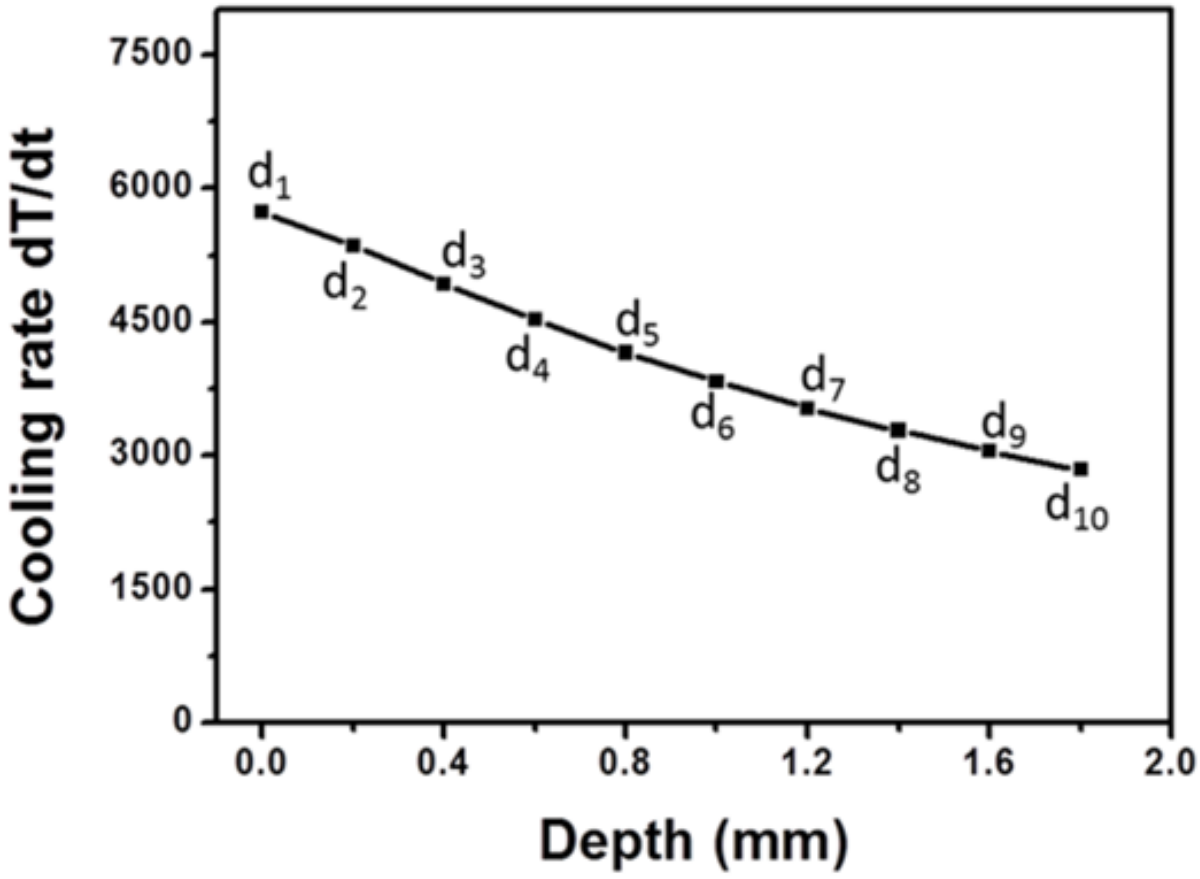

Figure 4.11 Variation of cooling rate with depth

It can be observed from the graphs that, the maximum temperature attained decreases with increase in depth but the maximum temperature attained remains same along the track (x-direction) at a given depth (Figure 4.9). The variation in cooling rates along the depth (z-direction) predicted by the thermal model (Figure 4.11) appears to be directly correlated to the

change in microstructure within the coating (Figure 4.6). The interface between the substrate and the coating is dendritic in nature due to the slow cooling rate experienced by this region (Figure 4.11)coupled with the large amount of compositional dilution from the substrate (Table 4.1).

There is a gradual change in morphology from dendritic and equiaxed to cellular-dendritic away from the interface. The orientation of the cellular morphology is due to the convective heat transfer within the melt occurring during processing. Due to the convective transfer of the melt and diffusion kinetics, a substantial redistribution of solute elements also takes place. The coating also consists of amorphous islands as discussed earlier and it may be pointed out that even the lowest cooling rate predicted by our model ($\approx 10^3$ K/s) is significantly higher than the critical cooling rate necessary to develop amorphous or glassy matrix of the coating alloy used in the present investigation (140–190 K/s [139][33]).

Table 4.1 Compositional analysis in the dendritic phase

Element	Fe	B	C	Mo	Cr	Y
Composition (at %)	70.27	13.59	8.09	1.22	6.23	0.58

Thus, the evolution of morphologies at different depths of the coating (Figure 4.6) is justified based on the cooling rate (thermal effect) and the evolution of the dendritic structure and the formation of amorphous phase is attributed to the distribution of solute elements which will be discussed in the discussion section. In addition, the equiaxed structure can be attributed to the generation of heterogeneous nucleation sites due to chipping of the fine dendritic tips by convectional fluid flow during processing. Furthermore, average composition of different zones of grain morphology as shown in Figure 4.6 measured by EDS indicated a distinct variation in the compositional range of columnar (Y 0.69 at % Mo 6.35 at % Cr 6.87 at % Fe 86.09 at %) and equiaxed grain structure (Mo 3.31 at % Cr 3.94 at % Fe 92.75 at %). The reasons for

amorphous to crystalline phase transformation are explained in detail in the section on discussion.

4.3 Role of Yttrium in GFA (Glass Forming Ability)

It has been shown that minor addition of rare earth materials like yttrium improve the glass forming ability (GFA) of the present system (Fe-Cr-Mo-C-B) drastically [54][142] and the reasons are two fold, 1) yttrium moves the composition of the glassy alloy close to the deep eutectic composition resulting in increase of GFA and 2) it stabilizes the under-cooled liquid by increasing ΔT i.eT_g-T_x (where T_g and T_x correspond to glass transition and crystallization temperatures respectively)[143]. Due to strong affinity of yttrium towards oxygen, yttrium in the present case exists in the form of oxide which is evident from the strong crystalline peak corresponding to (2 2 2) plane of Y_2O_3 (Figure 4.2) observed in the diffraction spectrum of all the samples. It is also reported that presence of oxygen has a very detrimental effect in the formation of a glassy phase in different systems like Zr-based as well as Fe-based amorphous materials. This may be attributed to the influence of oxygen in triggering precipitation of heterogeneous oxide nuclei within the amorphous matrix which in turn results in rapid nucleation and growth of the crystalline phases [54] . The detrimental effect of oxygen in destabilization of amorphous phase has been investigated from the early periods of synthesis of BMGs. The first BMG was synthesized by the addition of boron oxide flux to reduce the effect of oxide inclusions [144]. The intense crystalline peak of Y_2O_3 in the XRD spectra (Figure 4.2) indicates the presence of high amounts of oxygen and therefore, the minor amount of yttrium present in the parent material gets oxidized during processing, resulting in poor glass forming ability of the remaining phase. The evolution of the microstructure can be explained on the basis of rate of cooling as well as the change in composition locally. Numerous nano size precipitates can be

observed within the amorphous phase and these precipitates can be attributed to the formation of different carbides and oxides indicated in the XRD spectra (Figure 4.2). It has been reported that de-vitrification of the parent amorphous phase results in the formation of $M_{23}C_6$ type of carbides [145] (where M can be Mo or Cr) due to strong affinity of these metals towards carbon, and these phases are identified in the XRD spectra of the processed samples (Figure 4.2). The growth of the crystalline phases can be explained by the precipitation of different oxide and carbide phases acting as heterogeneous nucleation sites in the locally formed melt pool from which crystalline dendrites are developed.

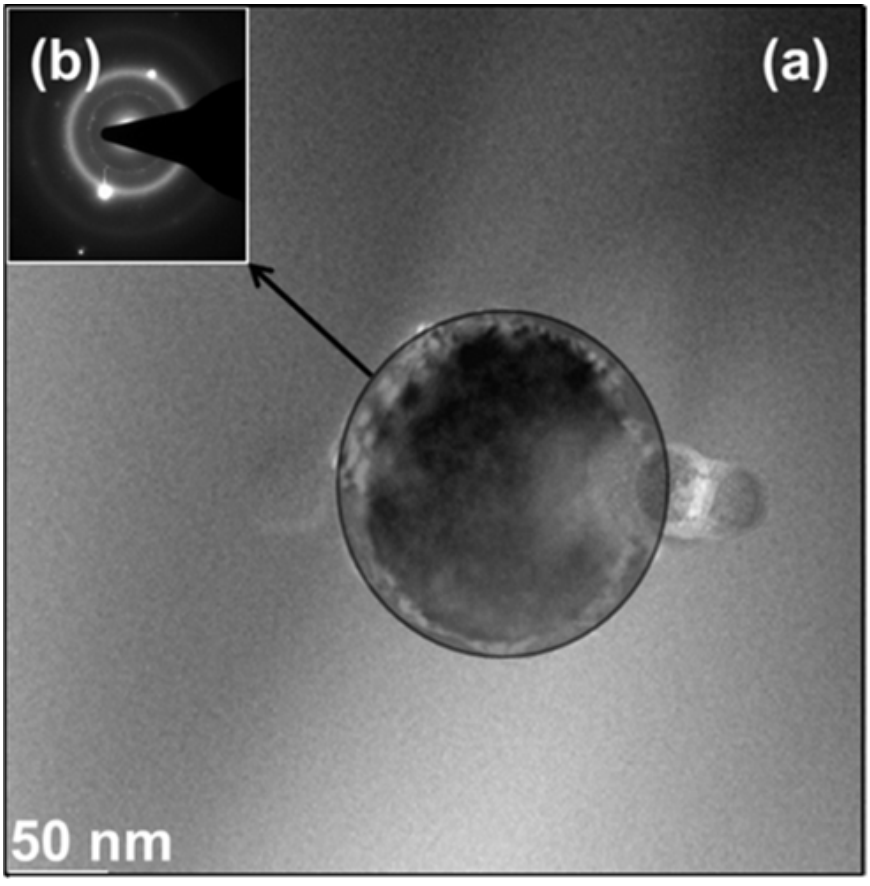

Figure 4.12 (a) TEM bright field image of the precipitate with the amorphous phase of the coating; (b) the inset showing the corresponding diffraction pattern from the region highlighted

Therefore the dominant factor for crystalline phase formation in spite of high cooling rates can be attributed to the formation of large volume fraction of these precipitates, predominantly Y_2O_3, evident from high intensities in XRD spectra (Figure 4.2).On further analysis of the high magnification TEM bright field image of one such precipitate, the diffraction pattern indicates the formation of FCC Fe in the vicinity of the precipitate indicated by the faint diffraction pattern (Figure 4.12). Furthermore, the EDS line profile (Figure 4.7) mapping across the precipitate indicates a clear increase in Fe concentration around the precipitate indicating the growth of Fe phase on the precipitate.

4.4 Morphological Evolution

The evolution of the morphology can be described by the solidification phenomena, as the solidification front from the nucleation site advances; it rejects solute into the remaining liquid resulting in the enrichment of the solute content in the liquid and as a consequence forms an amorphous phase. The reduction in the solute content in the crystalline phase is further confirmed by the spot EDS analysis in the dendritic phase (Table 4.1). The transformation from one phase to another is governed by both driving force (ΔG) as well as the kinetics. Although simulations give instantaneous values of temperature during laser material interactions that in turn dictates the cooling rates (kinetics), the net heat content of the material locally depends on average amount of heat absorbed in a time frame (driving force)d for a phase transformation to occur. Hence the average temperature generated by the spatially varied intensity in a Gaussian manner is an appropriate parameter. The average temperature values are calculated at different depths (Figure 4.10b) by considering the area under the curve within the time limits between the start of temperature rise and the temperature drop to 1000K (Eutectoid temperature). It can be observed that the average temperatures generated at the surface of the coating is around 2200 K

and gradually drops with increase in depth. The temperature reaches around 1754 K at a depth of 200μmthat is comparable to the melting temperature of pure Iron (1812 K) which further can be correlated to the melt depth of~ 300μm from the SEM micrograph (Figure 4.5).

Although the precursor powder has substantial amount of BCC-ferrite stabilizers, the formation of FCC austenite phase can be attributed to the formation of carbide phases that decreases the effect of the α-Fe stabilizers and the presence of carbon in the solid solution of the Fe matrix that stabilizes the Fe austenite phase. The retention of austenite phase in spite of rapid cooling rates (Figure 4.11) can be attributed to strong dependence (drop) of martensite start temperature (M_s) on different alloying elements, predominantly carbon. High amounts of carbon (~8at%) (Table 4.1) in the Fe matrix can be considered as the main contributing factor for the substantial decrease in M_s temperature potentially leading to retention of austenite phase. Thus in the present work the evolution of microstructure and phases in the coating synthesized using laser based technique can be attributed to change in both composition as well as thermal conditions.

4.5 Corrosion Studies[5]

The corrosion response has been investigated on the amorphous composite coatings by processed by varying the laser energy density from 26-46 J/mm^2. The processing conditions were chosen based on the precursor deposit thickness. Although the processing conditions are different, the post process phase and microstructure analysis indicated similar microstructure within the coating. In order to evaluate the microstructural changes occurring due to the corrosive environment, further characterization was also done on the samples after corrosion tests. The SEM micrographs of the corroded samples indicate that the base material corroded

[5] Parts of this section either in part or in full, are taken from Shravana Katakam, and Narendra B. Dahotre submitted to Journal of Alloys and Compounds for prospective publication and from Shravana Katakam, S. Santhanakrishnan, and Narendra B. Dahotre: JOM: TMS Journal. JOM, Vol. 64, No. 6, 2012

uniformly (Figure 4.13a) whereas the corrosion of the processed samples occurred only in certain preferential localized areas (Figure 4.13b-e).The SEM micrographs of the corroded samples indicate that no pits were observed for the samples processed with lower laser energy densities (26-33 J/mm^2) (Figure 4.13b-d). However, pitting occurred on the samples processed at higher energy density (36J/mm^2) (Figure 4.13e) and became extensive for the sample processed at highest energy density (46J/mm^2) (Figure 6(a)). The BSE micrographs (Figure 5(b)-(e)) of the corroded laser processed samples indicate the formation of black residue that is likely to be a carbon deposit as explained in the previous work [146]. It is clearly seen from the SEM micrographs that corrosion takes place predominantly in the inter-dendritic regions and at the amorphous islands for the samples processed with higher laser energy densities (46J/mm^2) (Figure 4.14b). The mechanisms involved during the corrosion process are discussed in the later sections of the paper.

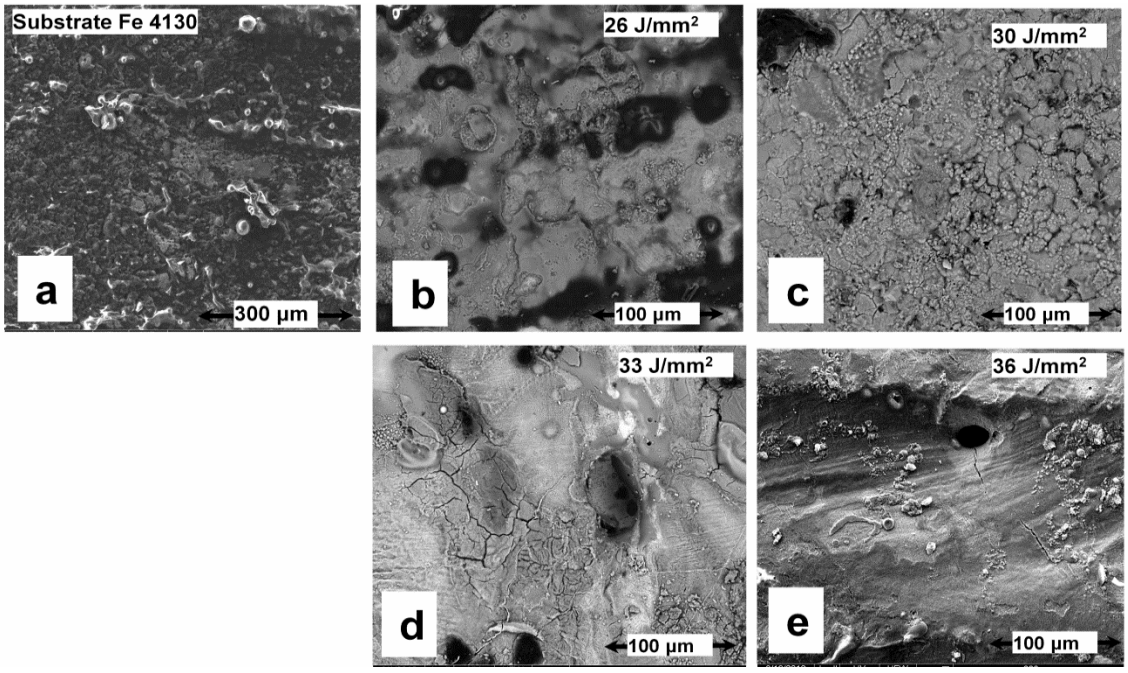

Figure 4.13 SEM micrographs of the corroded (a) base material and coatings processed with laser energy densities (b) 26 J/mm^2;(c) 30 J/mm^2; (d) 33 J/mm,^{2} and (e) 36 J/mm^2

4.5.1 Potentiodynamic Studies

Important corrosion parameters like corrosion potential, corrosion current, and the rate of corrosion are determined using the potentiodynamic polarization plots (Figure 4.15). It is clearly evident that as-received alloy has poor corrosion resistance associated with the high corrosion current densities and low corrosion potential. On the contrary, the laser coated samples exhibited substantial enhancement in the corrosion resistance that is clearly evident from the displacement of cathodic and anodic curves towards lower current densities and increased corrosion potential. The open circuit potential varies within a small range (71 mV) for all the laser processed coatings and it can be observed that the sample processed with highest energy density (46J/mm^2) has a lowest value of negative open circuit potential(-443 mV) (Figure 4.15and Table 4.2)

Table 4.2 Corrosion parameters as a function of laser energy density

Sample ID	Corrosion Rate (Microns/Year)	Corrosion Potential (E_{Corr}), mV	Corrosion Current (I_{Corr}), µA
Substrate	62	-503	46
26 J/mm^2	29	-490	13
30 J/mm^2	32	-482	15
33 J/mm^2	38	-514	18
36 J/mm^2	40	-512	18
46 J/mm^2	67	-443	31

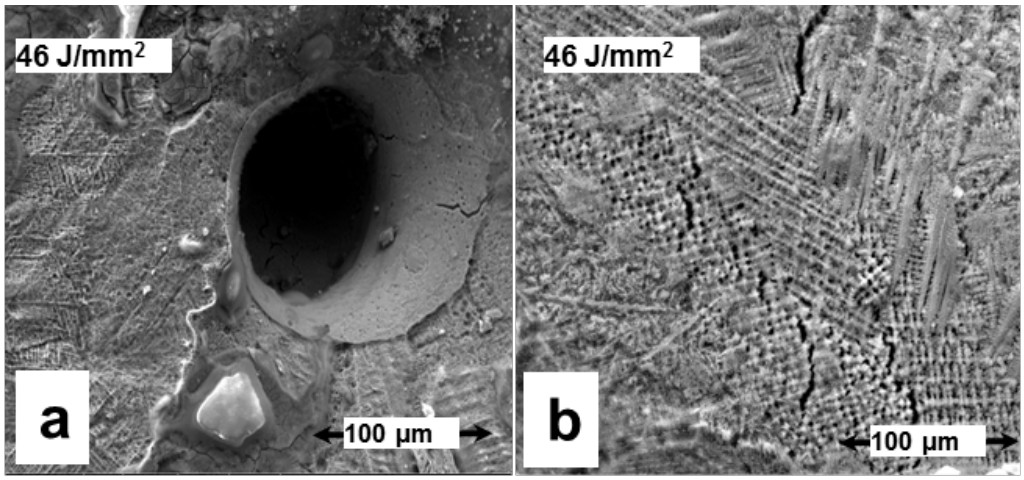

Figure 4.14 SEM micrographs of the corroded coating processed with laser energy density of 46 J/mm^2 (a) pits and (b) high magnification image

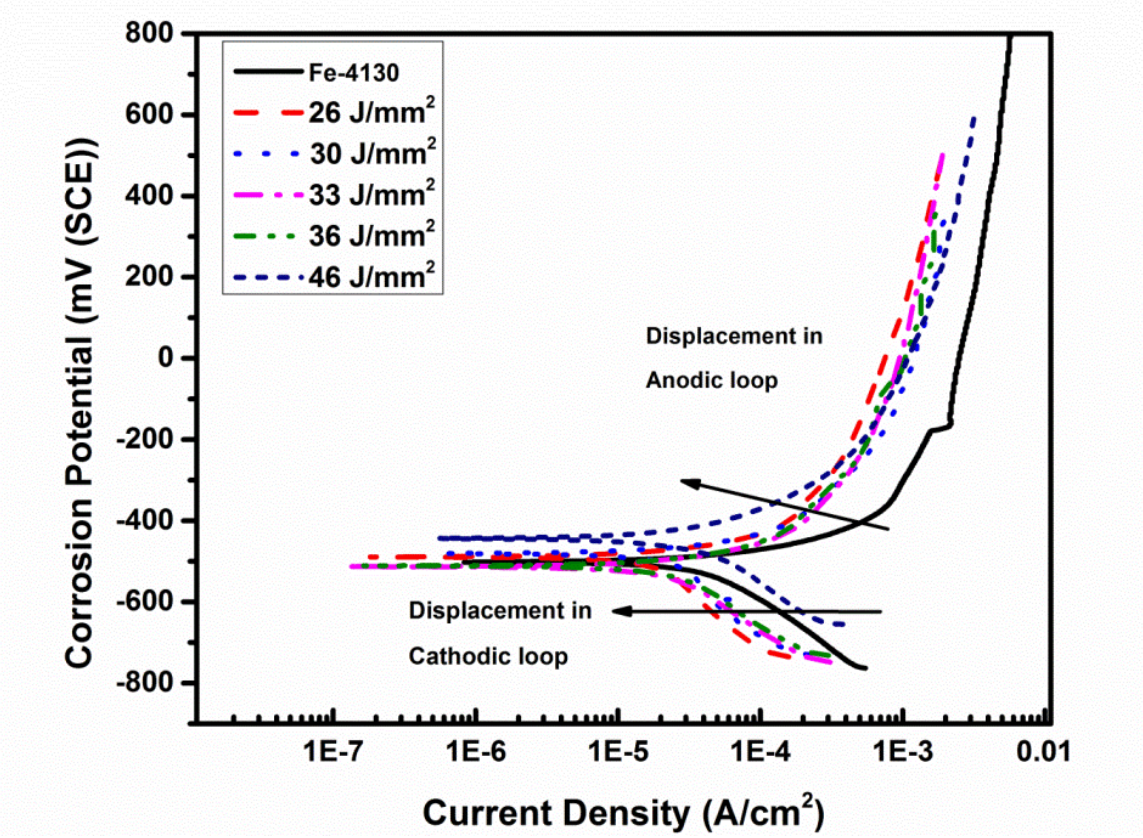

Figure 4.15 Comparison of potentiodynamic polarization curves before and after laser processing of amorphous coatings immersed in 0.01 M HCl solution at pH: 2.

The corrosion currents were determined by using linear extrapolation of the Tafel polarization plots. The results indicate that the coatings exhibit better corrosion resistance than

the substrate as indicated by the lower value of corrosion currents (<30 μA) (Table 4.2). Furthermore, it is also observed that the corrosion current for the sample processed with highest energy density showed lower corrosion resistance compared to the samples processed at different laser energy densities inspite of having largest amount of amorphous content. Thus, it is clearly evident that the processing conditions have a strong influence on the corrosion behavior of the coatings. In order to correlate the processing conditions to the observed microstructure and corrosion property, the thermal histories are simulated via computational thermal model and the results are discussed in the following section.

4.5.2 Thermal Histories Affecting Corrosion

As the thermodynamics and the kinetics govern the evolution of microstructure, the temperatures and the cooling rates are evaluated using a computational thermal model. It can be clearly seen that the instantaneous temperatures reached are well above the melting temperature (Figure 4.16 and Table 4.3) leading to formation of a metallurgical bond between the substrate and the coatings for all the laser processing parameters employed in the present effort. In general, if the nucleation rate is independent on time, the volume fraction of phase transformed after time t varies as a function of t^4 [147]. Based on the thermal model, the time for which the material is within the supercooled liquid region (T_m-T_g) (T_m=1394K and T_g=847K) [142] is measured and the results are tabulated (Table 4.3) It is observed that the sample processed with highest energy density (46J/mm^2) remains in the supercooled liquid region for the highest amount of time (13ms) compared to samples processed with lower energy density (26-36 J/mm^2) (6-9ms) and thus the crystallization can be expected to be more for the sample processed with highest laser energy density. Furthermore, it is also observed that the cooling rate that governs the kinetics of

the phase transformation increases with an increase in laser energy density. The cooling rate also plays a major role in nucleation and growth that is further discussed in the following section.

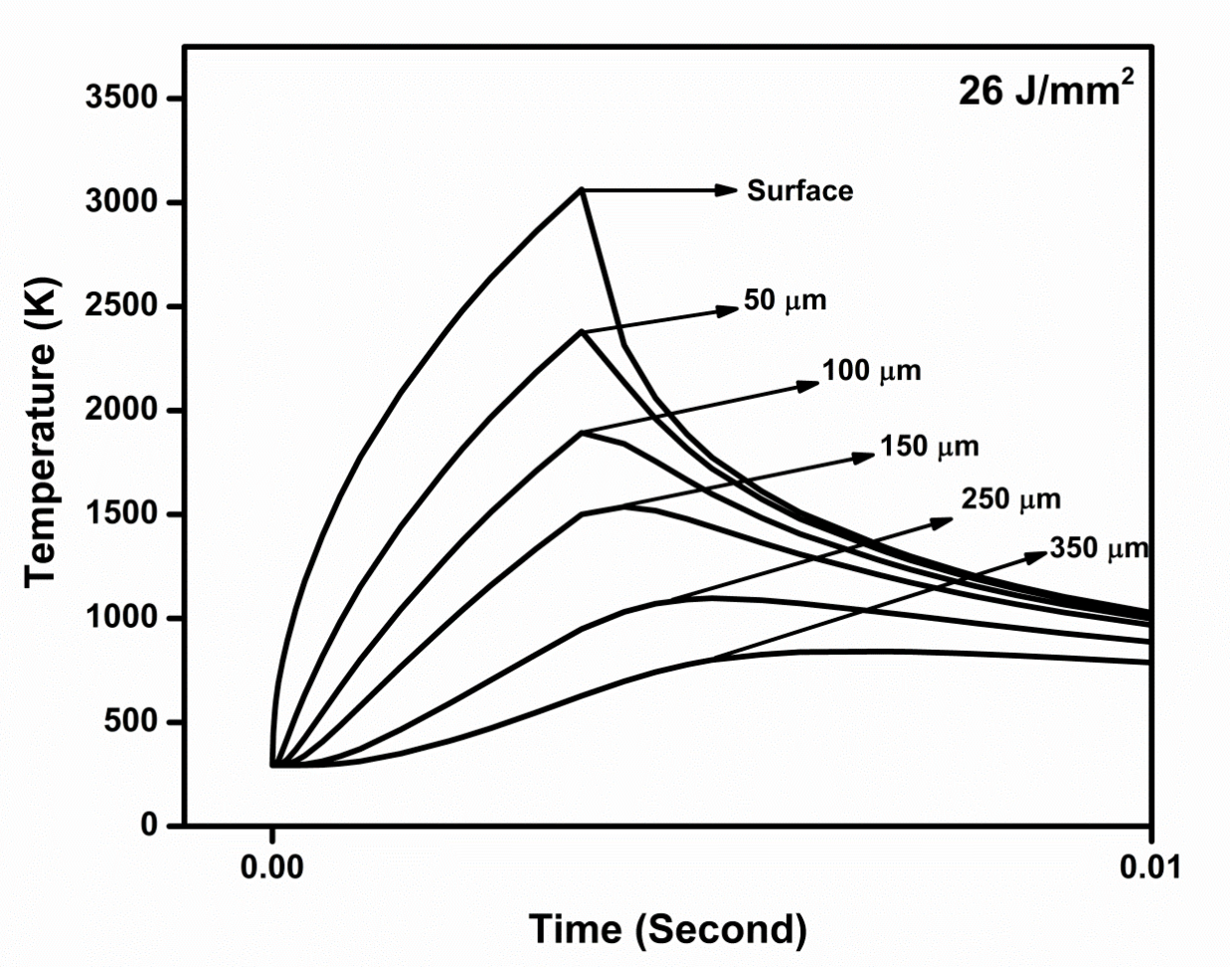

Figure 4.16 Typical thermal depth profiles generated by virtual thermal probes taken from an arbitrary point on the laser track

4.6 Corrosion Mechanisms

The present amorphous system has been extensively studied and the effect of yttrium on the GFA has been reported. The carbide phase is destabilized in the presence of yttrium and it is believed to be one of the reasons for improved GFA [54]. The XRD spectra indicate the formation of yttrium oxide and thereby reducing the GFA of the remaining liquid. Thus the liquid becomes prone to crystallization and results in the formation of composite microstructure.

The solubility of oxygen is higher in the liquid melt pool and the amount of liquid melt increases with an increase in laser energy density (Table 4.3).

Table 4.3 Surface temperatures and cooling rates as function of laser energy density

Laser Energy Density (J/mm^2)	Surface Peak Temperature (K)	Time in Supercooled Liquid Region (T_m-T_g) msec	Cooling Rate (K/sec)x 10^5
26	3063	6	2.196
30	3565	7.5	2.249
33	3783	8	2.324
36	4058	9	2.324
46	4983	13	3.435

Thus the oxide content is likely to increase with laser energy density due to higher peak temperatures (Table 4.3). As a consequence, a higher phase fraction (4%) of Y_2O_3 is associated with increase in laser energy density. Thus the liquid crystallizes due to reduction in GFA due to consumption of elemental yttrium [142] and results in the formation of different carbide and oxide phases along with α-iron. The carbide phases are one of the initial phases that form upon crystallization as reported by previous researchers [145]. The XRD (Figure 4.2) and TEM (Figure 4.17) results also indicate the formation of these carbide phases and hence influence the corrosion properties. The change in phase fraction of these carbides ~(5.5-2%) for different laser processing conditions could be one of the major contributing factors for the observed corrosion property. It is reported that the formation of different oxides and carbides of chromium leads to the formation of chromium depletion regions that are prone to corrosion [30,148]. A similar

phenomenon is the cause of corrosion for the laser processed samples with higher laser energy density. It is clearly seen from the SEM micrographs (Figure 4.14) that the inter-dendritic regions as well as the amorphous islands are corroded. The enhanced corrosion resistance of the fine dendritic phase may be attributed to the supersaturation of different solute elements due to rapid quenching [149]. In addition, high concentrations of Mo develop a trivalent Molybdenum oxide and prevent the dissolution of chromium from the chromium oxide passive layer. Thus, greater concentration of Mo results in spontaneous passivation [59][57,150,151]. Furthermore, it has been reported that carburization of steel improves the corrosion resistance [149] and in the present case, the absence of martensitic phase further confirms the super saturation of solute element (carbon) that is likely to drastically reduce the M_s (martensitic start) temperature and thus avoiding martensitic phase formation. The presence of excess carbon in the solid solution would lead to reduction in thickness of the passive film and thereby reducing the possibility for breaking of the film due to chemo-mechanical stress and formation of pit in the dendritic phase [149]. As mentioned earlier, the TEM analysis of the sample lifted from this amorphous region indicated the formation of nano-crystalline chromium carbide phase (Figure 4.17b) that leads to enhanced corrosion.

In addition to the formation of chromium carbide precipitates during solidification of the melt, re-heating effects can also influence the phase transformation. During multi-pass laser processing, a considerable amount of re-heating of the prior laser tracks takes place and the

temperature rise during re-heating increases with increase in laser energy density [152,153].

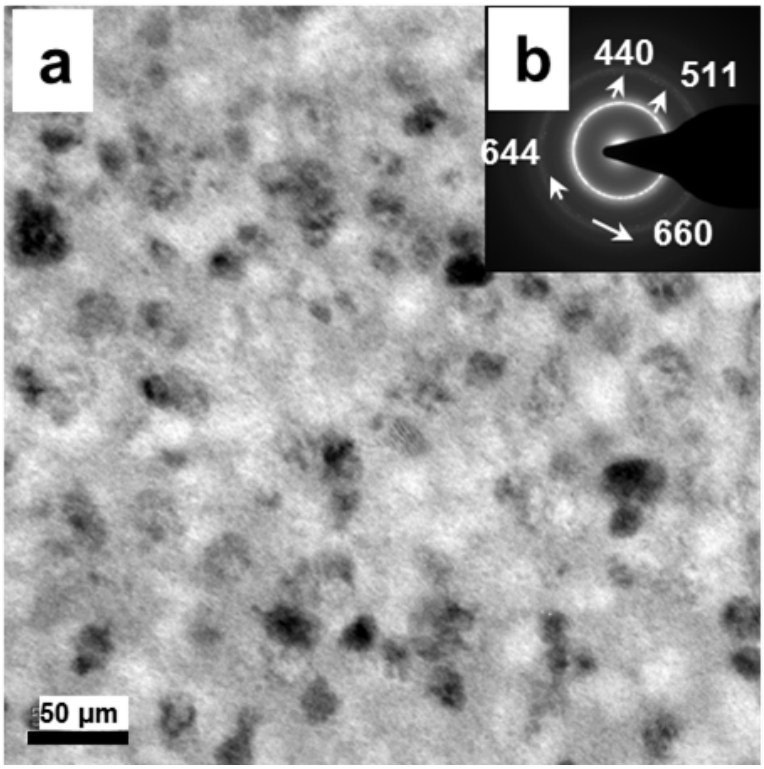

Figure 4.17 TEM micrograph of laser processed sample (46J/mm2) (a) Bright field image and (b) corresponding diffraction pattern

Thus, although rapid quenching results in the increase in phase fraction of amorphous content for the sample processed with highest energy density, the re-heating during subsequent laser passes is likely to increase the temperature of the previous tracks beyond the crystallization temperature leading to formation of nano-crystalline chromium carbide in the amorphous matrix (Figure 4.17). This also explains the increase in phase fraction of chromium carbide from the XRD results.

In contrast, no significant pitting is observed for the samples processed with lower laser energy density and the corroded surface developed a thick dark residue (Figure 4.13). This can be attributed to the formation of carbon residue as a corrosion product of the amorphous phase that has been reported and is in good agreement with the previous findings [146]. It is also

observed in the XRD spectra that no significant $(Fe,Cr)_{23}C_6$ carbide phase was formed for the samples processed with lower energy density. Furthermore, as mentioned earlier, the Y_2O_3 phase fraction decreases (3.5% to 2%) for the samples processed with lower energy density. Hence, yttrium present in the elemental form likely to suppress the formation of carbide phase thereby improving GFA for retention the amorphous phase. Thus the corrosion phenomenon is similar to that in the amorphous phase. It was also reported through scanning transmission electron microscopy) (STEM) EDS studies that the amorphous phase can have a chemical heterogeneity with Y-Mo rich clusters and Fe-Cr rich clusters [145]. In that case, corrosion can mainly occur at the Y-Mo rich clusters leaving behind carbon as the corrosion product. This explains the lower corrosion rate for the samples processed with lower laser energy density.

4.7 Summary of Laser Synthesis of Amorphous Coatings

In summary, an attempt is made to develop an amorphous coating on the steel substrate which resulted in the formation of a composite coating consisting of both crystalline and amorphous phases. The formation of crystalline phase is attributed to the formation of oxides which act as heterogeneous nucleation sites. Due to the formation of Y_2O_3 phase as indicated by XRD and TEM analysis, the role of Yttrium in increasing the GFA is lost and further Y_2O_3 also acts as nucleation site. A thermal model was developed to predict the thermal profiles and cooling rates which are critical for the formation of an amorphous phase. The thermal model predicted a cooling rate which is much higher than the critical cooling rate required for the formation of amorphous phase. The formation of composite microstructure is due to solute redistribution, formation of Y_2O_3, and heterogeneous nucleation sites.

Among the coatings synthesized for corrosion study, the highest laser energy density ($46J/mm^2$) processed coatings in concentrated HCL solution suffered highest corrosion rate.

Although no significant pitting was observed for the samples processed with lower laser energy densities (26-36J/mm^2) pitting increased gradually with increase in laser energy density. SEM and TEM observations revealed that preferential corrosion of amorphous phases is due to the existence of fine non-crystalline $Cr_{23}C_6$ phase within the amorphous islands. A carbon layer as the corrosion product was developed on the corroded surface of the samples processed with lower energy density. The corrosion behavior of the samples processed with lower energy density is similar to corrosion of bulk amorphous alloy but the samples processed with highest energy density suffered significant pitting corrosion.

CHAPTER 5

HIGH ENTROPY ALLOY COATINGS USING LASER

5.1 Characterization of Coating

5.1.1 Phase and Microstructure Analysis

The phase evolution of the samples was done using XRD analyses. Similar phase evolution was observed for all the samples processed with different laser processing condition. Phase analysis revealed the existence of Al phase along with body centered cubic (BCC) HEA peaks indicated in the pattern.

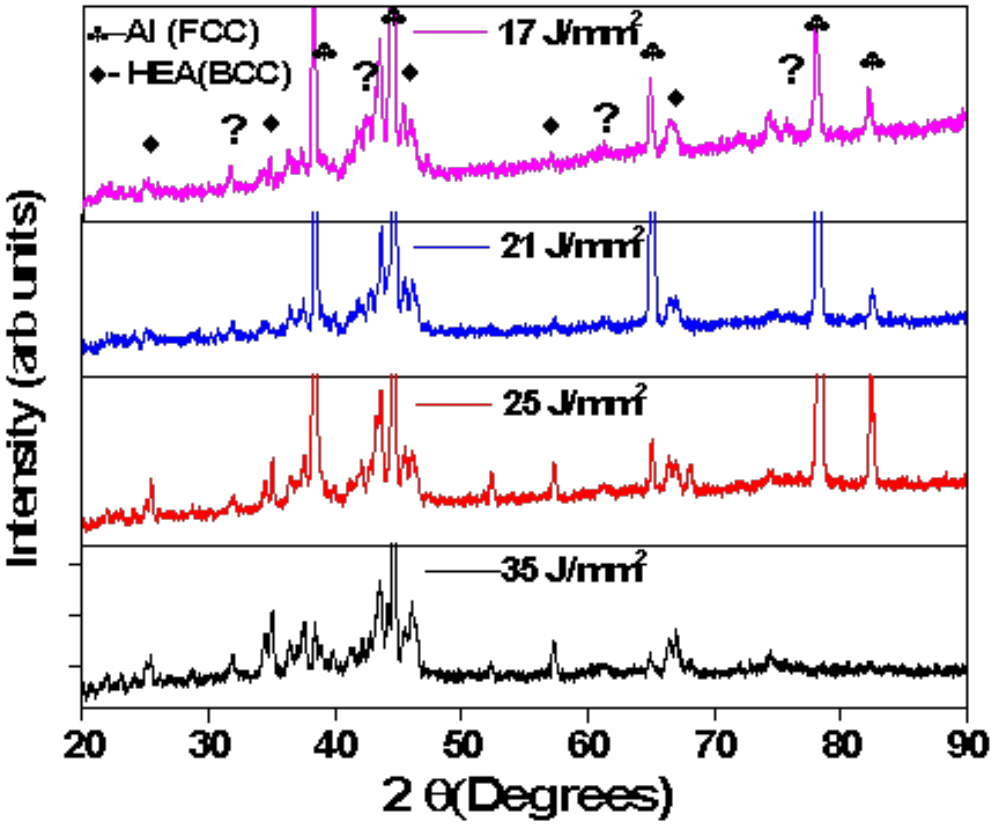

Figure 5.1 XRD of HEA coatings

Clear superlattice reflections are seen in the XRD pattern. This is attributed to the difference in atomic scattering factor of the elements resulting in intensity of the forbidden planes. Similar

XRD observations are reported in earlier reports. Additionally, there are peaks that are unidentified likely due to formation of intermetallics. Although there are overlapping intermetallic peaks, the peaks corresponding to HEA phase are observed at the same 2θ values as reported in literature by several authors indicating the formation of HEA phase. Formation of intermetallic phases can be attributed to non-uniform mixing of the elements in the melt pool leading to deviation from equiatomic composition. Thus, mixing entropy is not sufficient enough to suppress the intermetallic phase.

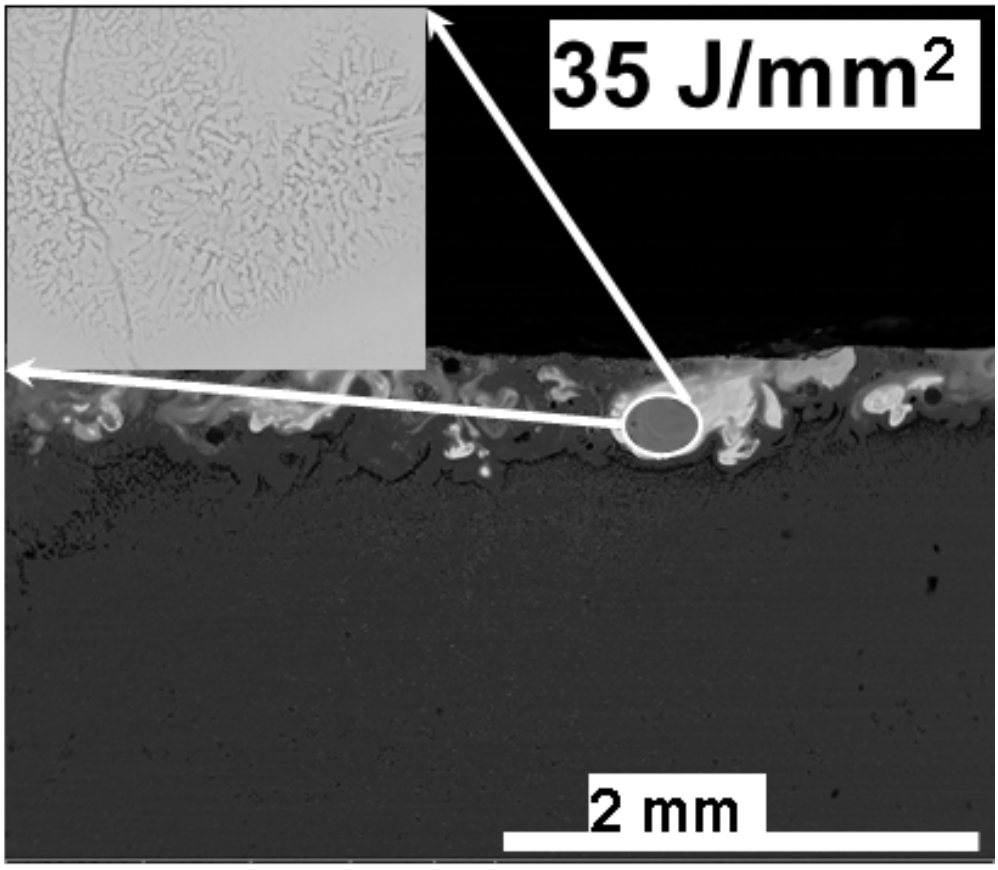

Figure 5.2 Backscatter SEM micrograph of HEA coating, inset shows high magnification image of HEA phase

In order to know the distribution of phases and evolution of microstructure SEM analysis was performed on the coating samples. The composite nature of the coating can be realized from

the SEM analysis with islands of precipitates with brighter contrast in the backscatter electron images along with aluminum matrix.

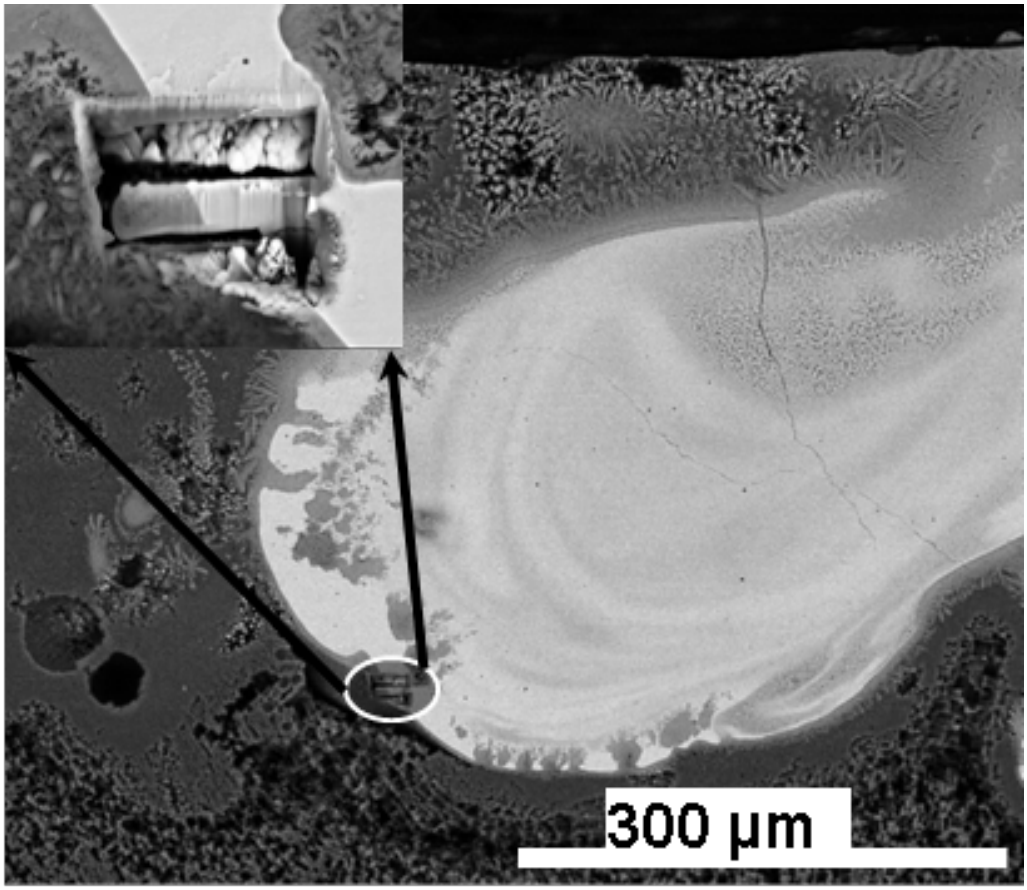

Figure 5.3 High magnification SEM image of HEA island inset showing the FIB liftout for TEM analysis

A fine columnar dendritic structure is also observed at the interface between the island and the aluminum matrix. The etched samples also revealed the formation of dendritic morphology within the islands.as shown in the high magnification micrograph (Figure 5.2). It has been reported that the morphology of the precipitates is a function of Al content and the morphology transforms from equiaxed in lower aluminum content to dendritic and finally to columnar dendritic structure or widemanstatten plane morphology for higher aluminum concentration [154,155] with the increase in Al. Phase analysis of the bright contrast phase is further done by site specific TEM characterization. A high magnification SEM image is taken at the location

from which a FIB lift out is made for TEM analysis. The bright and dark contrast of the lift out region is indicative of the microstructure with higher atomic elements. A clear two phase microstructure was evident from the bright field TEM micrograph.

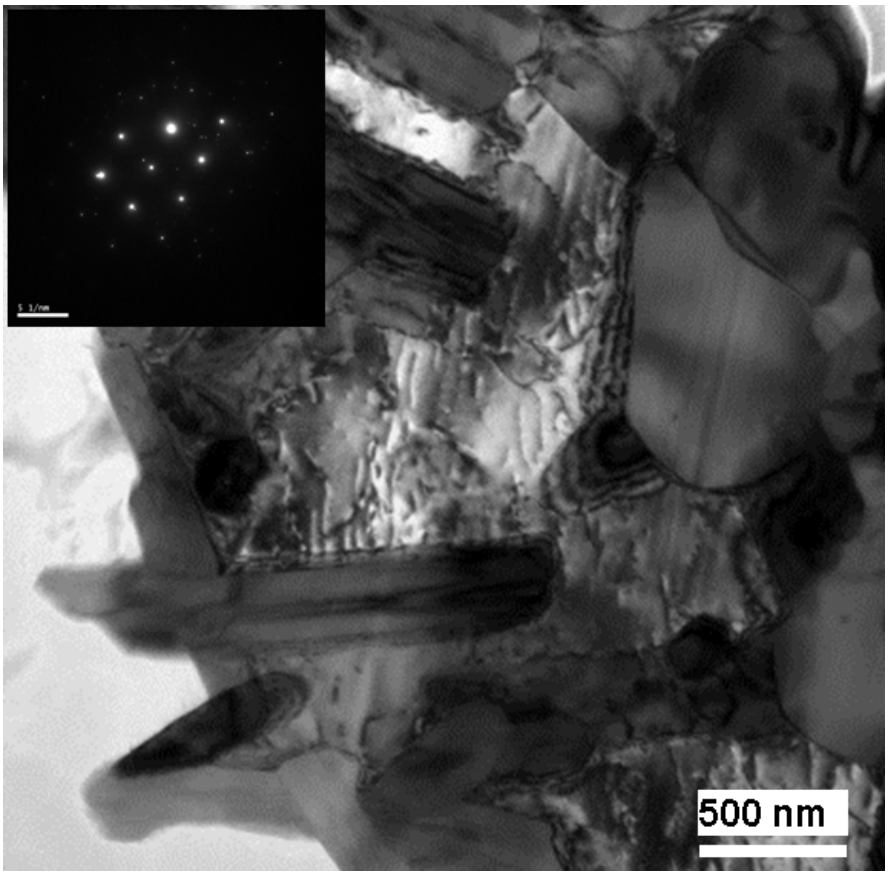

Figure 5.4 Bright field TEM micrograph, inset showing diffraction pattern from aluminum matrix

The diffraction analysis from the matrix region confirmed the presence of aluminum as shown in the diffraction pattern as inset in Figure 5.4. However, diffraction analysis of one such precipitate using a SAD aperture indicated the presence of a BCC phase based on the diffraction analysis as shown in the inset of Figure 5.5. Furthermore, in addition to the reflections corresponding to the BCC phase, closely spaced spots are observed in the diffraction pattern. The TEM diffraction pattern indicates that the crystal structure of the precipitate is observed to be BCC along the [111] zone axis. However, diffraction pattern of the same precipitate in a

different orientation exhibited a twofold symmetry with closely spaced diffraction spots indicating a long range periodic structure. Based on the above mentioned arguments, the precipitate has a simple BCC solid solution phase but there is further decomposition of the phase into small scale structures with long range periodic arrangement. Composition analysis of the microstructure is further performed to understand the distribution of alloying elements.

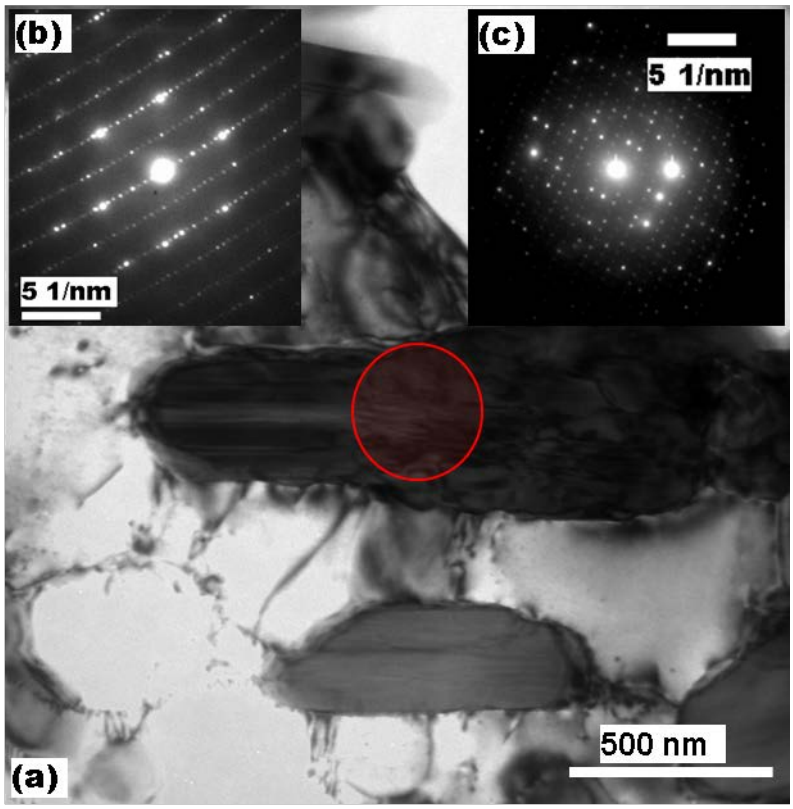

Figure 5.5 Bright field TEM of precipitate (a) SAD pattern along (111) zone axis; (c) another zone axis of the ordered phase

5.1.2 Composition Analysis

Chemical analysis was further performed on these morphologies using EDS in SEM. An EDS quantitative data is obtained by selecting an area within the island region (Table 5.1). It can be observed that the average composition of the island contains substantial amounts of all the elements as seen in Table 5.1.

Table 5.1 Average elemental composition from the bright contrast region (HEA)

Element	Al	Cr	Fe	Co	Ni
Concentration (at%)	13.12	26.83	20.88	16.42	22.76

Although substantial amounts of alloying elements are observed, a significant decrement in Al content is be observed compared to equiatomic composition. The effects of composition on the thermodynamic stability if further discussed. The composition analysis is further performed using STEM/EDS on the precipitate.

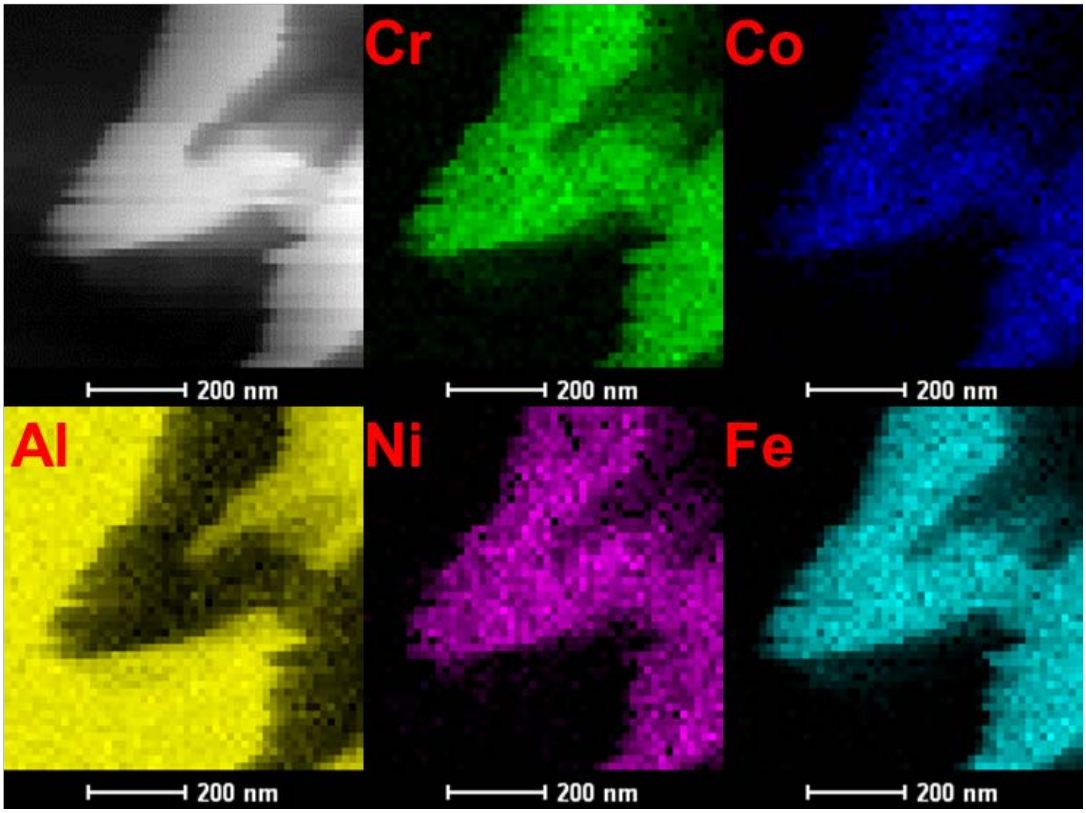

Figure 5.6 STEM/EDS showing the distribution of alloying elements

The STEM micrograph of the sample indicates a clear contrast between the precipitates and the matrix. The brighter contrast of the precipitate indicates the segregation of higher atomic elements into the precipitates as the STEM image gives a Z contrast similar to backscatter SEM image. Furthermore, STEM/EDS maps are generated to evaluate the distribution of different

alloying elements. It can be clearly observed from the STEM EDS maps that the precipitate consists of all the alloying elements. However, compared to matrix, which is aluminum, the precipitate is low in concentration which is in good agreement with the SEM EDS result. The effect of composition on the formation of a solid solution phase is further discussed in the next section.

5.1.3 HEA Formation Criteria

In conventional alloys, Home Ruthery rules are followed in ordered to predict the possibility of an alloy to form a solid solution. There have been efforts in formulating the thermodynamic rules for the formation of HEA phase based on the composition of the phase. Zhang et al suggested criteria for formation of solid solution based on atomic radius mismatch δ and enthalpy of mixing ΔH_{mix} given by the following equations.

$$\delta = \sqrt{\sum_{i=1}^{n} c_i \left(1 - \frac{r_i}{\check{r}}\right)^2}$$

here r_i is the atomic radius, ř is the average atomic radius given by $\check{r} = \sum_{i=1}^{n} c_i r_{i.}$, and ΔH_{mix} given by $4 \sum_{i=1, i \neq j}^{n} \Delta H_{ij}^{mix}$ based on average composition obtained by EDS analysis, the calculated value of δ is 0.66 and ΔH_{mix} is 4.06 kJ/mol. It has been observed that the range of δ for formation of solid solution is given by 1%< δ <5% [156] and ΔH_{mix} to be in the range of -15kJ/mol < ΔH_{mix} <0kJ/mol [157]. Hence, although δ is within the range of forming a solid solution, ΔH_{mix} is beyond the range which does not favour formation of HEA phase. However, laser processing being a rapid process, restricts the diffusion of different alloying elements thus retaining the HEA phase. Additionally, further TEM analysis, revealed the formation of layered structure as shown in Figure 5.7

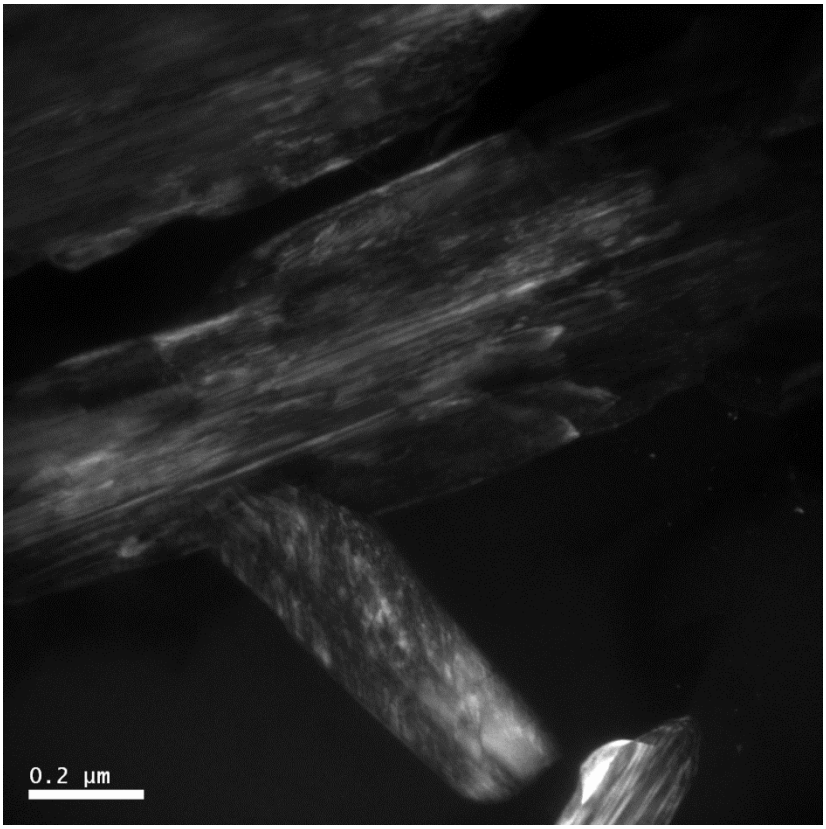

Figure 5.7 Dark field TEM micrograph taken from the ordered diffraction spots

As mentioned earlier, although there is a possibility of forming HEA phase, ΔH_{mix} is negative for only the binary solutions involving aluminium (Al-Fe, Al-Cr, Al-Fe, Al-Fe and Al-Co) indicating the fact that Al can have other elements as the nearest neighbours. However, ΔH_{mix} for other combinations of alloys (Fe-Cr, Fe-Co, Fe-Ni, Cr-Co, Cr-Ni, Co-Cr) is positive indicating the tendency of these elements to segregate. Thus, during multi-pass laser processing, the reheating effects might cause the HEA phase to decompose leading to the observed lamellar structure as seen in Figure 5.7

5.1.4 Summary of HEA Coating Using Laser Processing

High entropy alloy coatings were successfully synthesized using laser processing technique. The coatings consisted of islands of HEA phase within the aluminium matrix.

Furthermore, two different morphologies are observed within the island, dendritic and columnar dendritic structure. The evolution of morphology is attributed to difference in aluminium content. Further analysis of the HEA phase indicated a BCC structure along with long range ordering within the precipitate. The lattice mismatch calculations indicated the possibility of forming a HEA. The long range ordering is believed to be due to reheating effects leading to segregation of elements with positive enthalpy of mixing.

CHAPTER 6

CONCLUSIONS

6.1 Laser Thermal Treatment of Fe-Si-B Amorphous Ribbons

- ✓ The present study demonstrates the ability of laser processing technique to achieve extremely fine nanocrystalline microstructure using Fe-Si-B amorphous precursor.
- ✓ The laser material interaction revealed the evolution of nanocrystalline microstructure at the edge of the laser track while retaining an amorphous phase within the center region. The crystallization within the edge region is attributed to generation of thermal stresses during laser processing.
- ✓ Improved magnetic properties are for multi-pass laser processing compared to sample annealed using conventional furnace annealing samples attributed to compositional changes evolved within the phases in different heat treatments. Multi-pass laser processed samples exhibited higher coercivity due to rapid grain growth ascribed to reheating effects.
- ✓ Laser processing on a magnetic substrate resulted in substantial decrease in coercivity with an increment in saturation magnetization The reduction in coercivity is attributed to significant grain refinement due to synergistic effects of magnetic field coupled with thermal stresses experienced during laser processing.
- ✓ Microstructure-magnetic property-laser processing relationship has been established for the Fe-Si-B ternary system using different analytical techniques. It has been found that nanocrystallization by optimized laser processing conditions resulted in superior magnetic properties with significant increase in saturation magnetization coupled with near zero coercivity values for the sample processed on a magnetic substrate.

6.2 Laser Synthesis of Amorphous Fe-Cr-Mo-Y-C-B on Steel Substrate

- ✓ Laser cladding of pre-deposited amorphous powder coating on steel substrate resulted in the formation of a composite coating consisting of both crystalline and amorphous phases.
- ✓ The formation of crystalline phase is attributed to the formation of oxides which act as heterogeneous nucleation sites. Furthermore, due to the formation of Y_2O_3 phase as determined by XRD and TEM analysis, a reduction in GFA took place leading to crystallization.
- ✓ The thermal model predicted a cooling rate which is much higher than the critical cooling rate required for the formation of amorphous phase. Hence, the formation of composite microstructure is due to solute redistribution, formation of Y_2O_3, and heterogeneous nucleation sites.
- ✓ Corrosion response of the composite coatings in concentrated HCL solution showed improved corrosion resistance.
- ✓ The highest laser energy density ($46J/mm^2$) processed coatings suffered highest corrosion rate. No significant pitting was observed for the samples processed with lower laser energy densities ($26\text{-}36J/mm^2$) and pitting increased gradually with increase in laser energy density.
- ✓ SEM and TEM observations revealed that preferential corrosion of amorphous phases is due to the existence of fine non-crystalline $Cr_{23}C_6$ phase within the amorphous islands. A carbon layer as the corrosion product was developed on the corroded surface of the samples processed with lower energy density. The corrosion behavior of the samples

processed with lower energy density is similar to corrosion of bulk amorphous alloy but the samples processed with highest energy density suffered significant pitting corrosion.

CHAPTER 7

FUTURE DIRECTIONS

7.1 Laser Thermal Treatment of Fe-Si-B Amorphous Ribbons

- Effects of laser processing on the magnetic domain refinement
- Magnetostriction studies on the laser processed ribbons
- Compositional analysis of the magnetic field processed ribbons and study the partitioning behaviour of alloys elements in the presence of magnetic field
- Effects of magnetic field processing on the interface chemistry and subsequent magnetic response
- Extend the present study to hard magnetic materials to obtain a textured nanocrystalline microstructure

7.2 Laser Synthesis of Amorphous Fe-Cr-Mo-Y-C-B on Steel Substrate

- Study the slurry erosion response of the amorphous coatings
- Study the effects of reduction in dilution from substrate by multilayer deposits
- XPS and Atom probe study to understand the nature of oxide layers formed during corrosion
- Electrochemical Impedance study to understand the mechanisms of corrosion
- Synthesize a composition gradient microstructure and develop a composition window of glass forming range.

REFERENCES

[1] Steen WM, Hilton PA, Abdulhadi E, Pelletier J, Lambertin M, Decker I et al. 1997

[2] Gutfleisch O, Willard MA, Brück E, Chen CH, Sankar S, Liu JP. Adv Mater 2011;23:821.

[3] Yoshizawa Y, Oguma S, Yamauchi K. J.Appl.Phys. 1988;64:6044.

[4] Makino A, Hatanai T, Naitoh Y, Bitoh T, Inoue A, Masumoto T. Magnetics, IEEE Transactions on 1997;33:3793.

[5] Ohta M, Yoshizawa Y. J Magn Magn Mater 2009;321:2220-2224.

[6] Herzer G. Acta Materialia 2013;61:718-734.

[7] Gorria P, Orue I, Plazaola F, Barandiaran JM. J.Appl.Phys. 1993;73:6600.

[8] Allia P, Tiberto P, Baricco M, Vinai F. Appl.Phys.Lett. 1993;63:2759.

[9] Allia P, Baricco M, Knobel M, Tiberto P, Vinai F. Materials Science and Engineering: A 1994;179-180:361-365.

[10] Gupta A, Bhagat N, Principi G, Maddalena A, Malhotra N, Dasannacharya BA et al. Intermetallics 2000;8:287 - 291.

[11] Chen B, Li Y, Cai Y, Li R, Pang S, Zhang T. J.Alloys Compounds 2012;511:215-220.

[12] Chen B, Li Y, Yi M, Li R, Pang S, Wang H et al. Scr.Mater. 2012;66:1057.

[13] Chen B, Pang S, Han P, Li Y, Yavari AR, Vaughan G et al. J.Alloys Compounds 2010;504:S45-S47.

[14] Tariq NH, Hasan BA, Akhter JI. J.Alloys Compounds 2009;485:212.

[15] Svéda M, Roósz A. Mater.Sci.Forum 2013;752:175-182.

[16] Carvalho D, Cardoso S, Vilar R. Scr.Mater. 1997;37:523.

[17] Katakam S, Hwang JY, Vora H, Harimkar SP, Banerjee R, Dahotre NB. Scr.Mater. 2012;66:538-541.

[18] Katakam S, Santhanakrishnan S, Vora H, Hwang JY, Banerjee R, Dahotre NB. Philosophical Magazine Letters 2012;92:617-624.

[19] Wu G, Li R, Liu Z, Chen B, Li Y, Cai Y et al. Intermetallics 2012;24:50.

[20] Ahn S, Kim D, Kim HS, Baik K, Ahn SJ, Kim C. physica status solidi (b) 2004;241:1641-1644.

[21] Huang Y, Liu Y, Zhu GL. Key Eng Mat 2010;455:141-145.

[22] Ponnaluri SV, Cherukuri R, Molian PA. J.Mater.Process.Technol. 2001;112:199-204.

[23] Rauscher P, Hauptmann J, Beyer E. Physics Procedia 2013;41:312.

[24] Weidenfeller B, Riehemann W. J Magn Magn Mater 2005;292:210.

[25] Kollár P, Ramin D, Zeleňáková A, Riehemann W, Kuźmiński M. J Magn Magn Mater 1999;202:301.

[26] Raybould D, Meola M, Bye R, Das S. Materials Science and Engineering: A 1998;241:191.

[27] Zeleňáková A, Kollár P, Kuźmiński M, Kollárová M, Vértesy Z, Riehemann W. J Magn Magn Mater 2003;254:152.

[28] Zeleňáková A, Kollár P, Vértesy Z, Kuźmiński M, Ramin D, Rieheman W. Scr.Mater. 2001;44:613.

[29] Diegle RB. Corrosion 1980;36:362.

[30] Ha HM, Miller JR, Payer JH. J.Electrochem.Soc. 2009;156:C246.

[31] Guo RQ, Zhang C, Chen Q, Yang Y, Li N, Liu L. Corros.Sci. 2011;53:2351.

[32] Ni HS, Liu XH, Chang XC, Hou WL, Liu W, Wang JQ. J.Alloys Compounds 2009;467:163.

[33] Wang Y, Jiang SL, Zheng YG, Ke W, Sun WH, Wang JQ. Surface and Coatings Technology 2011;206:1307.

[34] Wang Y, Zheng YG, Ke W, Sun WH, Hou WL, Chang XC et al. Corros.Sci. 2011;53:3177.

[35] Zois D, Lekatou A, Vardavoulias M. J.Alloys Compounds 2010;504, Supplement 1:S283.

[36] Zhou Z, Wang L, Wang FC, Zhang HF, Liu YB, Xu SH. Surface and Coatings Technology 2009;204:563.

[37] Zheng ZB, Zheng YG, Sun WH, Wang JQ. Corros.Sci. 2013;76:337-347.

[38] Liu XQ, Zheng YG, Chang XC, Hou WL, Wang JQ, Tang Z et al. J.Alloys Compounds 2009;484:300-307.

[39] Wang AP, Wang ZM, Zhang J, Wang JQ. J.Alloys Compounds 2007;440:225.

[40] Zhao XB, Ye ZH. Surface and Coatings Technology 2013;228, Supplement 1:S266.

[41] Zhang C, Guo RQ, Yang Y, Wu Y, Liu L. Electrochim.Acta 2011;56:6380.

[42] Kim J, Kang K, Yoon S, Lee C. Surface and Coatings Technology 2011;205:3020.

[43] Jayaraj J, Sordelet DJ, Kim DH, Kim YC, Fleury E. Corros.Sci. 2006;48:950.

[44] Chen B, Li Y, Cai Y, Li R, Pang S, Zhang T. J.Alloys Compounds 2012;511:215.

[45] Huang K, Yan L, Wang C, Xie C, Zhou C. Transactions of Nonferrous Metals Society of China 2010;20:1351-1355.

[46] Li R, Li Z, Huang J, Zhu Y. Appl.Surf.Sci. 2012;258:7956-7961.

[47] Li R, Li Z, Zhu Y, Qi K. J.Alloys Compounds 2013;580:327 - 331.

[48] Liu G, An Y, Guo Z, Chen J, Hou G, Chen J. Appl.Surf.Sci. 2012;258:5380.

[49] Zhu YY, Li ZG, Li RF, Li M, Daze XL, Feng K et al. Appl.Surf.Sci. 2013;280:50.

[50] Asami K, Pang S, Zhang T, Inoue A. J.Electrochem.Soc. 2002;149:B366.

[51] Farmer J, Haslam J, Day S, Lian T, Saw C, Hailey P et al. Scientific Basis for Nuclear Waste Management 2006

[52] Farmer J, Choi J, Saw C, Haslam J, Day D, Hailey P et al. Metallurgical and Materials Transactions A 2009;40:1289.

[53] Diegle R, Sorensen N, Tsuru T, Latanision R. Academic Press, Treatise on Materials Science and Technology. 1983;23:59.

[54] Lu Z, Liu C, Porter W. Appl.Phys.Lett. 2003;83:2581.

[55] Shan X, Ha H, Payer J. Metallurgical and Materials Transactions A 2009;40:1324.

[56] Pharkya P, Shan X, Payer J. Materials science and technology-association for iron and steel technology- 2007;4:2424.

[57] Tan M, Akiyama E, Habazaki H, Kawashima A, Asami K, Hashimoto K. Corros.Sci. 1996;38:2137.

[58] Tan M, Akiyama E, Kawashima A, Asami K, Hashimoto K. Corros.Sci. 1996;38:349.

[59] Tan M, Akiyama E, Habazaki H, Kawashima A, Asami K, Hashimoto K. Corros.Sci. 1997;39:589.

[60] Ponnambalam V, Poon SJ, Shiflet GJ. J.Mater.Res. 2004;19:1320.

[61] Farmer J, Choi J, Saw C, Haslam J, Day D, Hailey P et al. Metallurgical and Materials Transactions A 2009;40:1289-1305.

[62] Ong M, Li Y, Blackwood D, Ng S. Materials Science and Engineering: A 2001;304:510.

[63] Kishitake K, Era H, Otsubo F. J.Therm.Spray Technol. 1996;5:476.

[64] Otsubo F, Era H, Kishitake K. J.Therm.Spray Technol. 2000;9:494.

[65] Branagan DJ, Swank WD, Haggard DC, Fincke JR. Metallurgical and Materials Transactions A 2001;32:2615.

[66] Wang A, Wang Z, Zhang J, Wang J. J.Alloys Compounds 2007;440:225.

[67] Liu D, Gao W, Li Z, Zhang H, Hu Z. Mater Lett 2007;61:165.

[68] Matthews DTA, Ocelík V, Branagan D, de Hosson JTM. Surface and Coatings Technology 2009;203:1833.

[69] Zhu Q, Wang X, Qu S, Zou Z. Surface Engineering 2009;25:201.

[70] Pang S, Zhang T, Asami K, Inoue A. Corros.Sci. 2002;44:1847.

[71] Pang S, Zhang T, Asami K, Inoue A. Journal of Materials Research-Pittsburgh 2002;17:701.

[72] Pang SJ, Zhang T, Asami K, Inoue A. Acta Materialia 2002;50:489-497.

[73] Kaufman L, Perepezko J, Hildal K. Joint International Topical Meeting on Mathematics and Computation and Supercomputing in Nuclear Applications (M&C SNA) 2007:15.

[74] Hildal K, Sekido N, Perepezko J. Intermetallics 2006;14:898.

[75] Lewandowski J, Gu X, Shamimi Nouri A, Poon S, Shiflet G. Appl.Phys.Lett. 2008;92:091918.

[76] Gu X, Poon SJ, Shiflet GJ. J.Mater.Res. 2007;22:344.

[77] Jones DA. Prentice hall, Principles and prevention of corrosion 1996;2nd edition

[78] Yeh J-, Chen S-, Lin S-, Gan J-, Chin T-, Shun T- et al. Advanced Engineering Materials 2004;6:299.

[79] Mingxi L, Yizhu H, Xiaomin Y. Appl.Surf.Sci. 2006;252:2882 -2887.

[80] Zhang H, Pan Y, He Y, Jiao H. Appl.Surf.Sci. 2011;257:2259 - 2263.

[81] Ye X, Ma M, Cao Y, Liu W, Ye X, Gu Y. Physics Procedia 2011;12:303.

[82] Ye X, Ma M, Liu W, Li L, Zhong M, Liu Y et al. Advances in Materials Science and Engineering 2011;2011:article ID 485942.

[83] Zhang H, Pan Y, He Y. Mater Des 2011;32:1910.

[84] Zhang YR, Ramanujan RV. Materials Science and Engineering: A 2006;416:161-168.

[85] Zhang YR, Ramanujan RV. Thin Solid Films 2006;505:97-102.

[86] Yoshizawa Y, Oguma S, Yamauchi K. J.Appl.Phys. 1988;64:6044.

[87] Yoshizawa Y, Yamauchi K. Magnetics, IEEE Transactions on 1989;25:3324.

[88] Yoshizawa Y, Yamauchi K. Mater.Trans.JIM 1990;31:307.

[89] Thompson K, Lawrence D, Larson DJ, Olson JD, Kelly TF, Gorman B. Ultramicroscopy 2007;107:131.

[90] Mehta N, Singh K, Saxena NS. Physica B: Condensed Matter 2009;404:2184-2188.

[91] Harimkar SP, Paital SR, Wang G, Liaw PK, Dahotre NB. Advanced Engineering Materials 2011;13:955.

[92] Liu XD, Lu K, Ding BZ, Hu ZQ. Materials Science and Engineering: A 1994;179-180:386 - 389.

[93] Gibson M, Delamore G. J.Mater.Sci. 1987;22:4550.

[94] Gibson M, Delamore G. J.Mater.Sci. 1992;27:3533.

[95] Jiang W, Atzmon M. Scr.Mater. 2006;54:333-336.

[96] :http://metglas.com/products/magnetic_materials/2605sa1.asp.

[97] Kim JJ, Choi Y, Suresh S, Argon AS. Science 2002;295:654.

[98] Chen H, He Y, Shiflet G, Poon S. Nature 1994;367:541.

[99] Lu J, Ravichandran G, Johnson WL. Acta Materialia 2003;51:3429.

[100] Greer JR, De Hosson JTM. Progress in Materials Science 2011;56:654 -724.

[101] Porter DA, & Easterling KE. Phase Transformations in Metals and Alloys, (Revised Reprint). CRC press, 1992.

[102] Horvath J, Ott J, Pfahler K, Ulfert W. Materials Science and Engineering 1988;97:409.

[103] Chrissafis K, Maragakis MI, Efthimiadis KG, Polychroniadis EK. J.Alloys Compounds 2005;386:165-173.

[104] Efthimiadis KG, Stergioudis G, Chadjivasiliou SC, Tsoukalas IA. Crystal Research and Technology 2002;37:827.

[105] Tian H, Zhang C, Zhao J, Dong C, Wen B, Wang Q. Physica B: Condensed Matter 2012;407:250-257.

[106] Yoon KE, Noebe RD, Hellman OC, Seidman DN. Surf.Interface Anal. 2004; 2004;36:594-597.

[107] Miller MK. Surf.Interface Anal. 2001; 2001;31:593 - 598.

[108] Hono K, Ping D, Ohnuma M, Onodera H. Acta materialia 1999;47:997.

[109] Herzer, G. 1997;10:415.

[110] Kudrnovský J, Christensen N, Andersen O. Physical Review B 1991;43:5924 - 5933.

[111] Okumura H, Laughlin DE, McHenry ME. J Magn Magn Mater 2003;267:347 - 356.

[112] Hines W, Menotti A, Budnick J, Burch T, Litrenta T, Niculescu V et al. Physical Review B 1976;13:4060 -4068.

[113] Ma XG, Jiang JJ, Bie SW, Miao L, Zhang CK, Wang ZY. Intermetallics 2010;18:2399-2403.

[114] Kulik T. J.Non Cryst.Solids 2001;287:145 -161.

[115] Herzer G. Scripta Metallurgica et Materialia 1995;33:1741-1756.

[116] Herzer G. J Magn Magn Mater 1996;157-158:133-136.

[117] Chen YM, Ohkubo T, Ohta M, Yoshizawa Y, Hono K. Acta Materialia 2009;57:4463 - 4472.

[118] Kim CK. Materials Science and Engineering: B 1996;39:195-201.

[119] Katakam S, Devaraj A, Bowden M, Santhanakrishnan S, Smith C, Ramanujan RV et al. J.Appl.Phys. 2013;114:184901.

[120] Köster, U, Meinhardt, J, Alves, H. 1995;179:533.

[121] Greer AL. Metallurgical and Materials Transactions A 1996;27:549.

[122] Ramanujan RV, Zhang YR. Appl.Phys.Lett. 2006;88:182506.

[123] Ramanujan R, Zhang Y. Physical Review B 2006;74

[124] Lu K. Materials Science and Engineering: R: Reports 1996;16:161.

[125] Wang X, Qi M, Yi S. Scr.Mater. 2004;51:1047 - 1050.

[126] Lai ZH, Conrad H, Teng GQ, Chao YS. Materials Science and Engineering: A 2000;287:238 - 247.

[127] Tsurekawa S, Okamoto K, Kawahara K, Watanabe T. J.Mater.Sci. 2005;40:895.

[128] Tsurekawa S, Kawahara K, Okamoto K, Watanabe T, Faulkner R. Materials Science and Engineering: A 2004;387:442.

[129] Vinzelberg H, Schumann J, Elefant D, Arushanov E, Schmidt OG. J.Appl.Phys. 2008;104

[130] Watanabe T, Suzuki Y, Tanii S, Oikawa H. Philosophical magazine letters 1990;62:9.

[131] Watanabe T, Tsurekawa S, Zhao X, Zuo L, Esling C. J.Mater.Sci. 2006;41:7747.

[132] Rivoirard S, Barthem VMTS, Garcin T, Beaugnon E, Miranda PEVd, Givord D. Journal of Physics: Conference Series 2009;156:012009.

[133] Cui BZ, Huang MQ, Yu RH, Kramp A, Dent J, Miles DD et al. J.Appl.Phys. 2003;93:8128.

[134] Rivoirard S, Barthem VMTS, Garcin T, Beaugnon E, Miranda PEVd, Givord D. Journal of Physics: Conference Series 2009; 2009;156:012009.

[135] Rivoirard S, Barthem VMTS, Bres R, Beaugnon E, de Miranda PEV, Givord D. J.Appl.Phys. 2008;104:043915.

[136] Kato H, Koyama K, Takahashi K. J.Appl.Phys. 2011;109:07A726.

[137] Hamaya K, Ueda K, Kishi Y, Ando Y, Sadoh T, Miyao M. Appl.Phys.Lett. 2008;93

[138] Passamani EC, Tagarro JRB, Larica C, Fernandes AAR. Journal of Physics: Condensed Matter 2002;14:1975-1983.

[139] Ma D, Tan H, Wang D, Li Y, Ma E. Appl.Phys.Lett. 2005;86:191906.

[140] Li X, Bian X, Hu L, Wu Y, Guo J, Zhang J. J.Appl.Phys. 2007;101:103540.

[141] Inoue A, Arnberg L, Oguchi M, Backmark U, Bäckström N, Masumoto T. Materials Science and Engineering 1987;95:101.

[142] Bouchareb A, Bendjemil B, Piccin R, Baricco M. Chinese Physics Letters 2010;27:076103.

[143] Liang G, Wong T, Su J, Woo C. J.Mater.Sci.Lett. 2000;19:1193.

[144] Klement W, Willens R, Duwez P. Nature 1960;187:869-870.

[145] Ha HM, Payer JH. Metallurgical and Materials Transactions A 2009;40:2519.

[146] Katakam S, Santhanakrishnan S, Dahotre NB. JOM 2012; 2012;64:709 -715.

[147] Kingery WD, Bowen H, Uhlmann D. Jhon Willey & Sons, New York

[148] Zhang C, Chan KC, Wu Y, Liu L. Acta Materialia 2012;60:4152.

[149] Heuer A, Kahn H, Ernst F, Michal G, Hovis D, Rayne R et al. Acta Materialia 2012;60:716.

[150] Tan M-, Akiyama E, Kawashima A, Asami K, Hashimoto K. Corros.Sci. 1996;38:349.

[151] Asami K, Naka M, Hashimoto K, Masumoto T. J.Electrochem.Soc. 1980;127:2130.

[152] Santhanakrishnan S, Kong F, Kovacevic R. J.Mater.Process.Technol. 2011;211:1247.

[153] Samant AN, Dahotre NB. Journal of the European Ceramic Society 2009;29:969 - 993.

[154] Pi J, Pan Y. Rare Metal Materials and Engineering 2013;42:232.

[155] Zhou YJ, Zhang Y, Wang YL, Chen GL. Appl.Phys.Lett. 2007;90:181904.

[156] Egami T, Waseda Y. J.Non Cryst.Solids 1984;64:113.

[157] He JY, Liu WH, Wang H, Wu Y, Liu XJ, Nieh TG et al. Acta Materialia 2014;62:105 - 113.